Analysis of the x dependence of leading hadron correlations at STAR

Xuan Li

Shandong University

Contents

Abstract

The constituents of the nucleon are discovered to be quarks and gluons. The dynamics of quarks and gluons are described by Quantum Chromodynamics (QCD). The gluons are the force carrier of the strong interaction between partons (quarks and gluons), and the strong force is characterized by color charge. The confined quarks together form protons, neutrons and other hadrons (e.g. pion). The mass of gluons is zero; the sum of quark mass inside a proton only occupies a small fraction of the proton mass. This means the strong interactions propagated by the gluons are predicted to play an important role in forming the mass of a proton. The constituents of a proton can be probed via high energy experiments. For example, Deep Inelastic Scattering (DIS) experiments scatter a lepton or neutrino off a proton (or nucleus) to probe partons with longitudinal momentum fraction x_{BJ} at resolution scale Q^2. The hard scattering processes can be factorized into convolutions between parton distribution function, parton scattering and parton fragmentation functions.

The quark distribution function is well determined, while the gluon distribution function derived from the structure function $F_2(x_{BJ}, Q^2)$ increases rapidity as x_{BJ} decreases at fixed Q^2. As x_{BJ} decreases, the proton gluon density increases rapidly as a gluon splits into two gluons or a quark can emit a gluon (gluon emission). The gluon distribution can not increase indefinitely due to the unitarity of the scattering amplitude. When the gluon splitting processes balances the gluon recombination processes, saturation is expected. The nuclear parton distribution is little known at low x_{BJ} region as the current fixed nucleus target DIS experiment only provides constraints to the nuclei gluon distribution function at $x_{BJ} > 0.02$. The forward particle production at RHIC can probe low x_{BJ} gluons. Forward inclusive neutral pion production measured at STAR experiment is found to be suppressed in d+Au collisions compared to p+p collisions, which is consistent with a Color Glass Condensate (CGC) description. However, inclusive production is a measure of the integral on a broad range of x_{BJ} value. To select a certain low x_{BJ} region, di-hadron azimuthal correlations with the leading particle triggered in the forward rapidity are further studied in d+Au collisions to probe the gluon distribution function of Au nuclei.

The STAR experiment at RHIC has a nearly continuous electromagnetic system spaning pseudo-rapidity $-1 < \eta < 4$ with full azimuthal angle coverage. The analysis in this thesis focuses on the azimuthal correlations between a leading neutral pion triggered in the FMS ($2.5 < \eta < 4.0$) and an associated neutral pion or jet-like cluster measured in the EEMC ($1.083 < \eta < 2.0$) during RHIC run8 p+p collisions and d+Au collisions at $\sqrt{s} = 200GeV$. The correlation studies in p+p collisions are taken as reference for d+Au results. The low x gluons in the dense gold nuclei are scattered by the deuteron nuclear probe, and their fragments can be measured by the FMS and EEMC detectors. The FMS-EEMC correlations provide sensitivity for the gold nuclei gluon distribution function within $0.003 < x_{BJ} < 0.02$ region. A threshold bounded cluster finder is developed to search the photon signal in the EEMC. We first looked at the FMS π^0 - EEMC π^0 azimuthal correlations [1]. The

statistics of FMS π^0 - EEMC π^0 are low. The direction of the initial partons does not rely on the type of final state particles. For this matter, Jets are more direct probes than inclusive hadrons. The electromagnetic calorimeters at STAR can determine the direction of jet. Therefore, we use the EEMC to reconstruct jet-like clusters based on cone radius algorithm. Details of excluding detector acceptance effects, suppressing the underlying event contributions to the jet-like cluster will be introduced in this thesis. The transverse momentum and collision centrality dependence of the azimuthal correlations are studied. To understand the pedestal underneath the correlation peak, a p+Au collision is approximated by requiring a neutron to be observed in the deuteron beam direction in d+Au collisions. The comparison between the FMS-EEMC correlation in p+Au collisions and d+Au collisions will be discussed as well. After a series of systematic check, the back-to-back azimuthal correlations of the FMS π^0 - EEMC jet-like clusters are found broader in d+Au collisions than in p+p collisions. The width differences between p+p and d+Au collisions are not dependent on the underlying event contributions to the jet-like clusters. The FMS-EEMC azimuthal correlations probe the intermediate x region for nuclei gluon distribution function the forward+mid-rapidity correlations and the forward+forward correlations. The forward di-hadron correlation studies at STAR proves a smooth transition from dilute parton gas to CGC state.

Chapter 1

Introduction

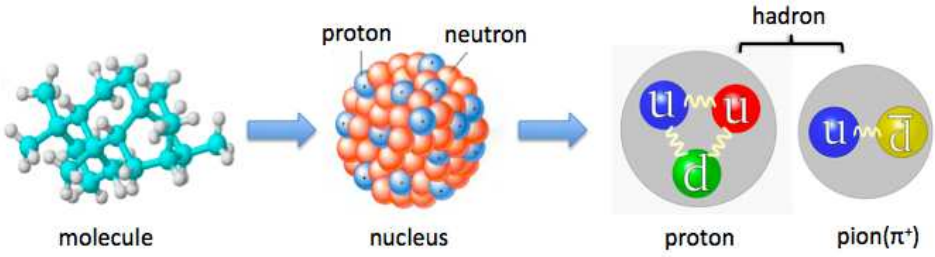

Figure 1.1: The schematics from molecule to hadron.

Normal matter only occupies about 4% of the universe energy. With the developments of high energy physics, the Standard Model (SM) describes the interactions between matter which consists of gravitation, electromagnetism, weak and the strong force. From a macroscopic view of point, the interaction of gravity and electromagnetic fields can be seen and felt by people. If you look inside the inner structure of matter from molecular, atom to nucleon, the order of strong force is about 100 times stronger than the electromagnetic force, which in turn is orders of magnitude stronger than the week force and gravitation.

We have the molecule concept as the fundamental particle for a long time; later on the molecule is discovered to be made of atoms. Nucleons (proton or neutron) inside a atom occupy most of the mass of the atom (see Figure 1.1). Before 1960s, the nucleons were thought to be the elementary particles which are constituents of the atomic nucleus. As the quark model was independently proposed by Murray Gell-Mann and George Zweig, quarks and gluons were introduced to be elementary particles of hadrons(including nucleons). The strong interaction arising from the interactions of colored quarks. Partons (quarks and gluons) inside nucleons are not static; the dynamics of partons can be described by Quantum Chromodynamics (QCD). QCD contains one very important characteristic : asymptotic freedom that means partons inside nucleons with short interaction length can be treated as free particles. The asymptotic freedom helps to make QCD a special gauge theory. By the 1990s, all six types of quarks (known as flavors: up, down, strange, charm, bottom, and top) were found in accelerator experiments. Explorations on the parton distribution inside nucleon or nucleus are performed by a series of Deep Inelastic Scattering (DIS) experiments which uses electrons, muons or neutrinos as probes to study the internal structure of nucleon or nucleus. The mass of a proton is not equal

to the sum of quark mass (gluon mass is zero) which indicates the strong interaction carried by the gluons play an important role in forming nucleons.

The parton density function in proton describes the probability of finding a parton inside the proton. It contains two parameters, one is the longitudinal momentum fraction x_{BJ} carried by the parton, and the other is the resolution scale Q^2 (which is inverse of the transverse size). According to Heisenberg uncertainty principle, to see the constituents of proton, we need to use a large momentum probe (eg. the virtual photon in deep inelastic scattering). The absorption of the probe results in an impulse (i.e. momentum transfer) to the constituent, and the observed colored constituent usually radiate gluons. The act of observing causes the constituent to radiate gluons, therefore the proton gluon density increases rapidly as resolution scale Q^2 increases at fixed x_{BJ}. Such process can be described by DGLAP function [2, 3, 4, 5]. The number of gluon increases as $1/x_{BJ}$ gets large at fixed Q^2. Radiation to even softer gluons is divergent in the fixed Q^2 evolution with $1/x_{BJ}$. This is analogous to the infrared catastrophe in QCD. To resolve this problem, the theoretically proposed resolution (BFKL function [6, 7, 8]) is that the gluon recombination can serve to balance gluon radiation, resulting in the expectation of saturation. In addition to BFKL equations which characterize the evolution of gluons with x_{BJ} at low Q^2, non-linear effects should be considered to resolve the scattering amplitude unitarity problem.

Deep Inelastic Scattering (DIS) experiments (eg. HERA collider) had proved the existence of gluons through Bjorken scaling violations [9]. However, gluons do not have electric charge, and they are only indirectly probed in DIS processes. Quarks carry color charges, therefore gluons can be directly probed by quarks. As there are no free quark state, hadrons can be treated as sources of quarks. Consequently, hadron-hadron collision experiments are developed to study QCD phenomena. Recent experimental results at RHIC in d+Au collisions can be well described by the Color Glass Condensate (CGC) theory. The forward particle production is dominated by asymmetric partonic scattering between a large x valence quark and a low x gluon. Therefore, the low x gluon of the Au nuclei can be probed by the dilute deuteron nuclei through asymmetric partonic scattering (usually the scattering happens between a high x ($x > 0.2$) valence quark inside the deuteron nuclei and a low x ($x < 0.01$) gluon inside the Au nuclei) in d+Au interactions. As shown in Figure 1.2, low x_{BJ} gluon means high center of mass energy $\sqrt{s}$, low Q^2 and large pseudo-rapidity η in hadron(nucleus)-hadron(nucleus) collisions. Inclusive particle production measures the integral over a broad x_{BJ} region. Di-hadron correlations can select a narrow low x_{BJ} range.

The high luminosity d+Au collisions produced by RHIC run8 operations provide opportunities to study cold nuclear matter effects (see the schematics of STAR detectors of RHIC run8 in Figure 1.3). The p+p interactions in RHIC run8 are taken as reference for d+Au interactions. The forward π^0-π^0 back-to-back ($\Delta\varphi \sim \pi$) azimuthal correlations in d+Au collisions are broader than the results in p+p collisions [10]. Suppression of back-to-back azimuthal correlations of forward rapidity neutral pion pair was observed in central d+Au collisions. This phenomena can be well de-

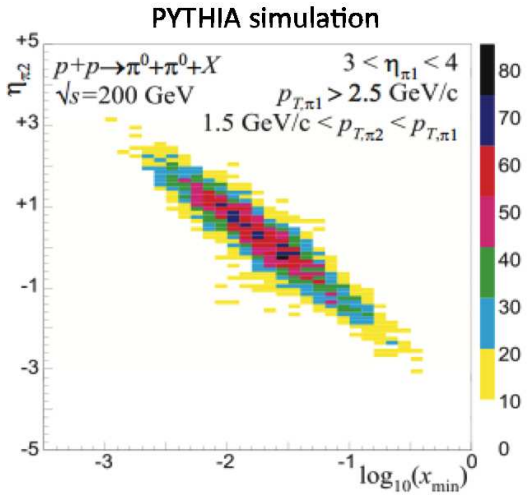

Figure 1.2: PYTHIA simulation of the π^0 - π^0 correlations in p+p collisions at $\sqrt{s} = 200GeV$. The leading π^0 with pseudo-rapidity $3 < \eta_{\pi 1} < 4$ and $p_{T,\pi 1} > 2.5GeV/c$, the associated π^0 requires $1.5GeV/c < p_{T,\pi 1} < p_{T,\pi 2}$. The pseudo-rapidity of the associated π^0 $\eta_{\pi 2}$ is shown in the vertical axis and the x (i.e. x_{min}) of the soft gluon involved in the asymmetric partonic scattering is shown in the form of $log_{10}(x_{min})$ in the horizontal axis. The pseudo-rapidity of the associated π^0 $\eta_{\pi 2}$ is strongly correlated with the soft gluon x_{min}, i.e., larger $\eta_{\pi 2}$ smaller the x_{min} is.

scribed by CGC calculations [11]. However, there is no significant broadening from p+p to d+Au for the forward+central rapidity azimuthal correlations [12]. The FMS-EEMC azimuthal correlations (they are forward+near-forward correlations) sit in the intermediate region between forward+forward and forward+mid-rapidity correlations [1]. The analysis in this thesis is about the FMS π^0 - EEMC π^0 or jet-like cluster azimuthal correlations. This will address how smoothly the transition process from dilute parton system to dense CGC state is. Details of the analysis will be introduced further in the following chapters. In chapter 2, we will introduce the relative theoretical model and phenomena. The detector configuration and setup will be introduced in chapter 3. Data analysis including trigger setup, Monte Carlo simulation, π^0 and jet-like cluster reconstructions will be discussed in chapter 4. Results considering removing detector acceptance effects and underlying event contributions to the jet-like clusters will be discussed in chapter 5. Chapter 6 gives the conclusion and outlook. Implement of the forward+near-forward correlation studies completes the full picture of transition from dilute parton gas to Color Glass Condensate state for gold nuclei.

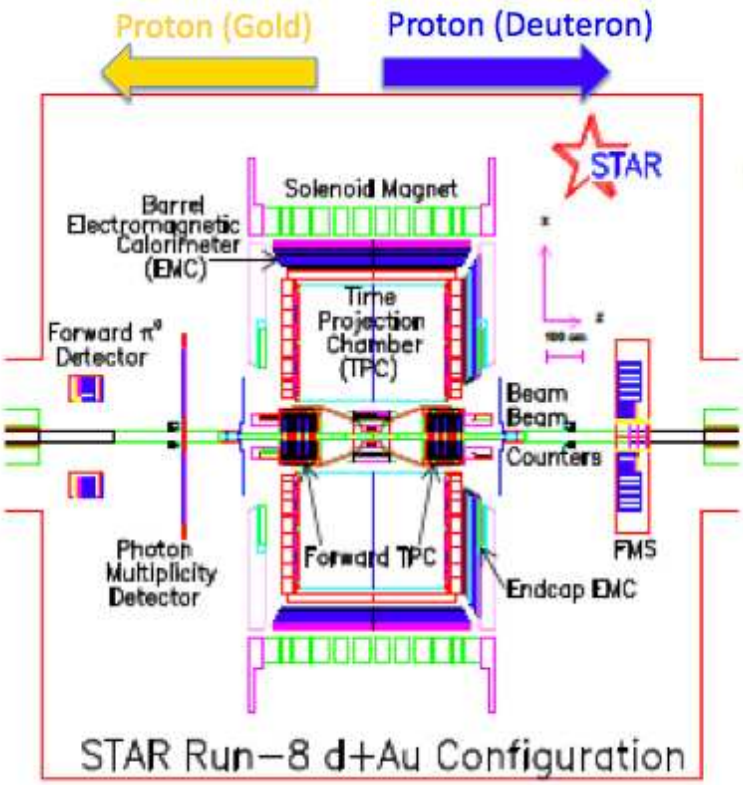

Figure 1.3: STAR schematics along the beam pipe in RHIC run8 p+p and d+Au collisions. Blue beam (deuteron beam in d+Au collisions) facing the west part of STAR and yellow beam (gold beam in d+Au collisions) facing the east side of STAR.

Chapter 2

Theory description and phenomenology

The Bjorken scaling violation observed by the deep inelastic scattering experiment at HERA collider indicates the existence of gluons. The gluon distribution function can be extracted from the proton structure function $F_2(x_{BJ}, Q^2)$ [13, 14]. The evolution of the proton parton distribution function on Q^2 can be well interpreted by perturbative QCD (pQCD) [15, 16]. Moreover, the gluon distribution function rises rapidly as x_{BJ} decreases with a fixed Q^2 [17]. At a sufficiently low x_{BJ}, gluon recombination is expected to balance gluon splitting, which leads to gluon saturation. The universality of the QCD factorization formulation allows the parton distribution function and fragmentation functions to be applied in the hadron-hadron interactions as well. The nuclei gluon distribution function is expected to be denser than in nucleon at the same x_{BJ}. The detailed theory interpretation related with the analysis of this thesis will be introduced in the following sections. We will first introduce Quantum Chromodynamics (QCD) and Deep Inelastic Scattering (DIS). The parton distribution function which describes the probability of finding a parton inside the proton (or nuclei) can be extracted from DIS experiments in Bjorken frame. Later on, dipole frame is developed and treat the virtual photon in DIS process as a quark anti-quark pair. In the dipole frame, we can more direct to describe the scattering process of gluons. The gluon distribution derived from experiment is found to increase rapidly as x decreases with a fixed low Q^2. In additional to DIS experiment, hadron(nucleus)-hadron(nucleus) collisions can probe the initial state parton as well. To solve the unitarity problem of the hadron scattering amplitude, non-linear corrections to the parton evolution are tried and Color Glass Condensate (CGC) is one example. Details of these theory descriptions will be discussed and the phenomena observed in DIS experiment and RHIC experiments which are correlated with low x physics will be introduced as well.

2.1 Quantum Chromodynamics

Quantum chromodynamics (QCD) is a theory describing the strong interaction between quarks and gluons making up hadrons. It is a non-abelian field (Yang-Mills) theory respecting SU(3) symmetry. Quarks carry three different color charges, red, green and blue which make up the fundamental representation of SU(3). Unlike photons in the quantum electromagnetic field theory (QED), the strong force carrier gluons carry color charges. The QCD Lagrangian which describes the kinematics of

quarks and gluons is defined as following[15, 16],

$$\mathcal{L}_{QCD} = -\frac{1}{4}F^a_{\mu\nu}F^{a\mu\nu} + \sum_q \bar{q}_i(i\gamma^\mu D_\mu - m_q)_{ij}q_j, \tag{2.1}$$

and the field strength tensor $F^a_{\mu\nu}$ is given by,

$$F^a_{\mu\nu} = \partial_\mu A^a_\nu - \partial_\nu A^a_\mu - g_s f^{abc} A^b_\mu A^c_\nu \tag{2.2}$$

where q_i is the quark field, i or j stands for different flavor of quarks, A^a_μ is the gluon field with color charge a, f_{abc} is the SU(3) structure constants and abc stands for different color charge [15]. The covariant derivative D_μ is,

$$(D_\mu)_{ij} = \delta_{ij}\partial_\mu + ig_s T^a_{ij} A^a_\mu, \tag{2.3}$$

where T^a_{ij} are the Lie group generators connecting fundamental, anti-fundamental and adjoint representations of the SU(3) gauge group. As gluons also have color charges, the QCD theory contain quark-gluon and gluon-gluon interaction vertices.

There are two important properties in QCD theory. When the separation distances are small, which means high energy interactions, the coupling forces between quarks and gluons are weak: quarks and gluons can be treated as free particles. This behavior which was first discovered by David Politzer, Frank Wilczek and David Gross (2004 Nobel prize in physics) is known as "asymptotic freedom".

At long distances or small energy scales, the coupling forces between quarks and gluons are so strong that the amount of energy to separate them goes to infinity. This behavior called "confinement" explains the absence of free quark objects in high energy experiment. The strong coupling constant is defined as following [18],

$$\alpha_s(Q^2) \equiv \frac{g_{s(Q^2)}}{4\pi} = \frac{1}{\beta_0 ln(Q^2/\Lambda^2_{QCD})} \tag{2.4}$$

where β_0 is a constant, Λ_{QCD} named with QCD scale sets the momentum scale at which the strong force can not be described by perturbative QCD. The value of Λ_{QCD} is around 200MeV. The strong coupling constant α_s is a function of Q^2. At small α_s, which is equivalently small separation distances between quarks and gluons, perturbation theory techniques are applied and such interactions are "hard" processes. Non-perturbative process with typical momentum scale Q less than 2GeV/c are defined as "soft" processes. The time scale $1/Q$ suppresses the interactions between the stuck parton in the hadron and the co-moving partons in the leading order coupling constant. Separation of hard and soft interaction is valid in this limit.

Due to color confinement, quarks or gluons are always in the form of hadrons which are color neutral. Hadrons include mesons, which are made of quark anti-quark pairs, and baryons, which are made of three quarks. The constituents of nucleon are named "partons" which were initially postulated by Bjorken [19] before QCD was defined. In order to study the behavior of partons inside the nucleus,

lepton or neutrino nucleus scattering experiments were performed. Later on, hadron hadron scattering experiments including fixed target apparatus or collider facilities appeared. QCD factorization theorem [20] is developed to separate such scattering cross section into two parts: perturbative hard scattering parts which are calculable in perturbative QCD, and non-perturbative universal long distance functions.

As the transverse size hadron grows slowly with $\sqrt{s}$, unlike the rapid growth of the gluon density with $\sqrt{s}$ (i.e. the growth of the gluon density with energy is actually probing small x, low x requires high energy). Consequently, more and more gluons are put into a fixed area. This means that the gluons begin to "see each other", so that gluon recombination can compete with gluon radiation. The total cross section of a hadronic scattering process is expected to be bounded by the logarithm squared of the center of mass energy s [21],

$$\sigma(s) \leq \sigma_0 ln^2(s). \tag{2.5}$$

This is known as the Froissart bound. The universal long distance functions contain the parton distribution functions, fragmentation functions, multi-parton correlation functions and many other form factors. They are determined by global fits on the experimental data.

2.2 Deep inelastic scattering

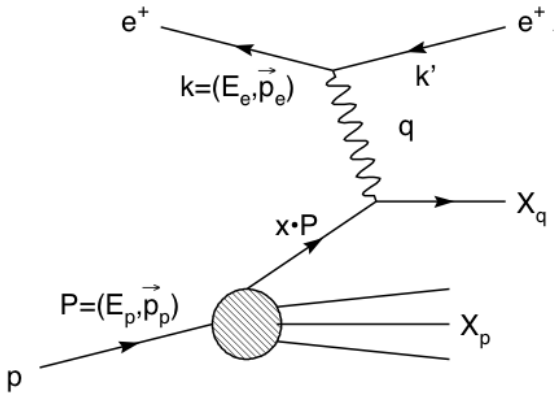

Figure 2.1: The leading order positron-proton deep inelastic scattering. Please see the definition of the parameters in text.

High energy lepton(or neutrino)-nucleon deep inelastic scattering (DIS) plays an important role in exploring the inner structure of the nucleon (eg. proton). In lepton-nucleon DIS process, lepton emits a virtual photon to interact with partons inside the nucleon. Figure 2.1 shows the positron-proton DIS scattering process for example. The parameters marked in this figure are defined as following,

(1) P is the four momentum vector of the proton,

(2) k is the four momentum vector of the incident positron e^+,

(3) q is the four momentum transfer from the positron (it is opposite to the four momentum vector carried by the virtual photon Q),

(4) ν ($\nu = |E_e - E_{e'}|$) is the energy transfer from the positron to the virtual photon.

The longitudinal momentum fraction of the scatted quark x_{BJ} is defined as,

$$x_{BJ} \equiv \frac{Q^2}{2P \cdot q}. \tag{2.6}$$

There are a set of parameters that characterize the inclusive cross sections of DIS,

- the center of mass energy squared $\sqrt{s}$ ($s = (P + k)^2$),
- the four momentum squared of the virtual photon Q^2 which is also the transfer four momentum squared from positron to the hadron or nucleon q^2 ($Q^2 = -q^2$).
- the longitudinal momentum fraction carried by a parton inside the hadron or nucleon x_{BJ} (see definition in Eq 2.6) at lowest order of perturbative QCD.
- the ratio of the virtual photon energy to the positron energy y in the rest frame of hadron or nucleon ($y = \frac{Q^2}{x_{BJ} \cdot s}$).

These parameters satisfy the relation $x_{BJ} = Q^2/s \cdot y$. At fixed y, two asymptotic limits need consideration. The first called Bjorken limit is related with fixed x_{BJ}, $Q^2 \to \infty$, $s \to \infty$. The second one called Regge-Gribov limit corresponds to fixed Q^2, $x_{BJ} \to 0$, $s \to \infty$. According to uncertainty principle, the De Broglie wave length $\lambda \sim \frac{2\pi\hbar}{Q}$ and Q ($Q^2 = -q^2$)is the momentum transferred from the lepton to the hadron. The higher the Q is the smaller the sensitive area is. When the Q is large enough, the nucleon breaks and generates new hadronic final states. We use W_p to stand for the mass of the recoiling system X_p and M_p to stand for the mass of the nucleon. DIS process requires $Q^2 \gg M_p^2$ (deep) and $W_p^2 \gg M_p^2$ (inelastic) [22]. From Quantum electrodynamics (QED), the cross section of the DIS can be factorized in terms of leptonic tensor $L^{\mu\nu}$, hadronic tensor $W_{\mu\nu}$ and the associated strong coupling const $\alpha_S(Q^2)$. The structure functions $F_i(x, Q^2)$ (i=1,2) are defined in terms of the hadronic tensor $W_{\mu\nu}$. Therefore, the double differential cross section with respect to the scattered positron energy E' and the relative angle between the momenta of the outgoing positron and the incoming positron (the energy is E) θ is,

$$\frac{d\sigma}{dE' d\Omega} = \frac{\alpha^2}{4E^2 sin^4(\frac{1}{2}\theta)}[W_2 cos^2(\frac{1}{2}\theta) + 2W_1 sin^2(\frac{1}{2}\theta)], \tag{2.7}$$

where W_1 and W_2 are structure functions of x_{BJ} and Q^2 ,

$$W_1 = \frac{1}{2m_p} \sum_i e_i^2 f_i(x_{BJ}), \tag{2.8}$$

$$W_2 = \frac{-2m_pc^2}{q^2}x_{BJ}^2 \sum_i e_i^2 f_i(x_{BJ}). \tag{2.9}$$

Therefore, the structure function can be redefined as the following,

$$F_1(x_{BJ}, Q^2) \equiv m_p W_1 = \frac{1}{2}\sum_i e_i^2 f_i(x_{BJ}), \tag{2.10}$$

$$F_2(x_{BJ}, Q^2) \equiv -\frac{q^2}{2m_pc^2}W_2 = x_{BJ}\sum_i e_i^2 f_i(x_{BJ}), \tag{2.11}$$

where $f_i(x_{BJ})$ is the parton distribution function and i stands for the flavor of parton. The structure functions $F_1(x_{BJ}, Q^2)$ and $F_2(x_{BJ}, Q^2)$ are usually measured in DIS experiment like HERA collider [9]. In high energy experiments, the proton (or lepton) can be accelerated to a very high speed (nearly the speed of light). Therefore, we can consider the proton carrying a very large momentum component along z-axis in a frame (this is so-called *infinite momentum frame*). Consequently, the transverse momentum of the partons inside proton is small compared to their longitudinal components. In this so-called Bjorken limit when $Q^2 \to \infty$ with fixed x_{BJ}, the structure functions become independent of Q^2; $F(x_{BJ}, Q^2)$ can be written as $F(x_{BJ})$. As the resolution scale Q^2 increases, quarks can be probed by the virtual photon. If the Q^2 is large enough (larger than the inverse of the transverse size of a quark), the cross section of the DIS should be a constant, and the phenomena is called Bjorken scaling. This means the elementary particles inside the proton are quarks (gluons will be introduced later). No smaller constituents are observed with current experiments.

2.2.1 Parton dynamics inside nucleon

Comparing Eq 2.10 and 2.11 reveals a relation between structure function $F_1(x_{BJ})$ and $F_2(x_{BJ})$,

$$F_2(x_{BJ}) = 2x_{BJ}F_1(x_{BJ}). \tag{2.12}$$

Such relation is called Callan-Gross relation based on parton model. This relation implies that the point-like particle that the lepton (or neutrino) is colliding with within the proton must have spin $\frac{1}{2}$. If the target particle had spin 0 rather than spin $\frac{1}{2}$, the structure function $F_1(x_{BJ}) = 0$ which is contrary to the experiment measurements.

Bjorken scaling established that DIS must be described in terms of parton-photon process and the partons are independent point-like particles. The Callan-Gross relation supports that quarks that interact with photon are spin $\frac{1}{2}$ fermions. QCD (beyond the quark model) allows scaling violation, $F_2 - 2xF_1$ (defined as F_L) is non-zero. The non-zero F_L measured in experiments probes the existence of gluons. Parton distribution function $f(x_{BJ}, Q^2)$ which is defined as the number density of partons with flavor f (quark u, d, s, c, t, b or gluon) and momentum fraction x_{BJ} when probing the resolution scale is Q^2 inside a nucleon. The parton distribution

function is used to describe the initial dynamic behavior of partons inside the proton. $F_2(x_{BJ}, Q^2)$ is proportional to $x_{BJ} f(x_{BJ}, Q^2)$,

$$F_2(x_{BJ}, Q^2) = \sum_i e_i^2 x_{BJ} f_i(x_{BJ}, Q^2), \tag{2.13}$$

where i stands for the quark flavor (u, d, c, s, t, b). The quark distribution function $f_i(x_{BJ}, Q^2)$ can be extracted from structure function $F_2(x_{BJ}, Q^2)$.

Figure 2.2 shows the data of DIS experiment at HERA collider for the $F_2(x, Q^2)$ as a function of Q^2 at different x_{BJ}. At large x_{BJ}, the structure function $F_2(x, Q^2)$ does not dependent on Q^2, which is the Bjorken scaling phenomena. As x_{BJ} decreases, the scaling breaks which indicates more and more gluons are involved in the interactions (gluons have strong interactions with the scattered quark). Quarks obtain transverse momentum in a nucleon through radiating gluons and this causes logarithmic scaling violations which are particularly large at low x_{BJ}. Therefore, structure functions $F_{1,2}$ are not constant in Q^2 any more which lead to Bjorken scaling violations. From lepton-nucleon deep inelastic scattering (DIS) experiments, Bjorken scaling breaks when x_{BJ} decreases to $x_{BJ} < 0.03$, see Figure 2.2. This phenomena can be explained as the nucleon is hit harder and harder (i.e. at large Q^2), the gluons and their emitted quark-antiquark pairs are involved in the interaction. The gluon distribution function $g(x_{BJ}, Q^2)$ can be derived from the function $F_2(x_{BJ}, Q^2)$ [23],

$$x_{BJ} g(x_{BJ}, Q^2) \approx \frac{\partial F_2(x_{BJ}, Q^2)}{\partial ln Q^2} \tag{2.14}$$

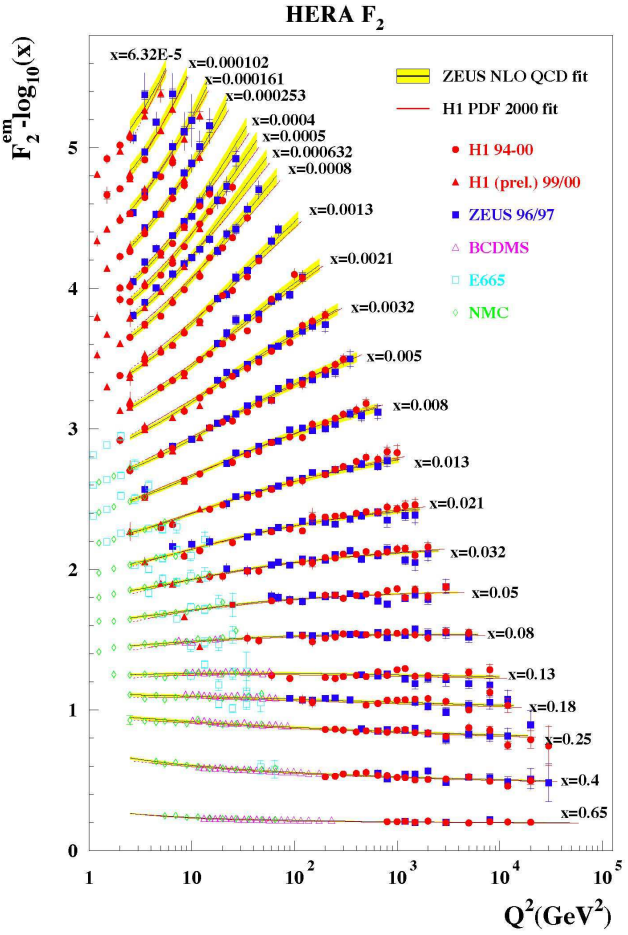

Figure 2.2: The $F_2(x, Q^2)$ structure function in deep inelastic scattering, taken from [9]. The Bjorken scaling appears at large x_{BJ}, but it breaks at low x_{BJ} region which is related with the interaction between the projectile quark and gluons inside the proton before or after DIS scattering process. This leads to that the gluon distribution function can be derived from the structure function $F_2(x, Q^2)$.

The slope of the $F_2(x_{BJ}, Q^2)$ gets larger when the x_{BJ} becomes lower. This reflects more and more gluons are involved in the DIS scattering. And the derived gluon distribution function $x_{BJ}g(x_{BJ}, Q^2)$ increases as x_{BJ} decreases. The left panel of Figure 2.3 shows $x_{BJ}g(x_{BJ}, Q^2)$ versus x_{BJ} at different fixed Q^2 under CTEQ6M model [24]. $x_{BJ}g(x_{BJ}, Q^2)$ increases rapidly as x_{BJ} decreases, which is consistent with the $F_2(x_{BJ}, Q^2)$ results.

In general, all observables involving a hard hadronic interaction (such as structure functions) can be expressed as a convolution of calculable, process-dependent coefficient functions and universal parton distributions. The factorization mechanism provides a path to calculate the hard hadronic scattering including DIS processes. The whole process is the convolution among parton distribution function,

hard partonic scattering and parton fragmentation function.

2.2.2 Parton evolution

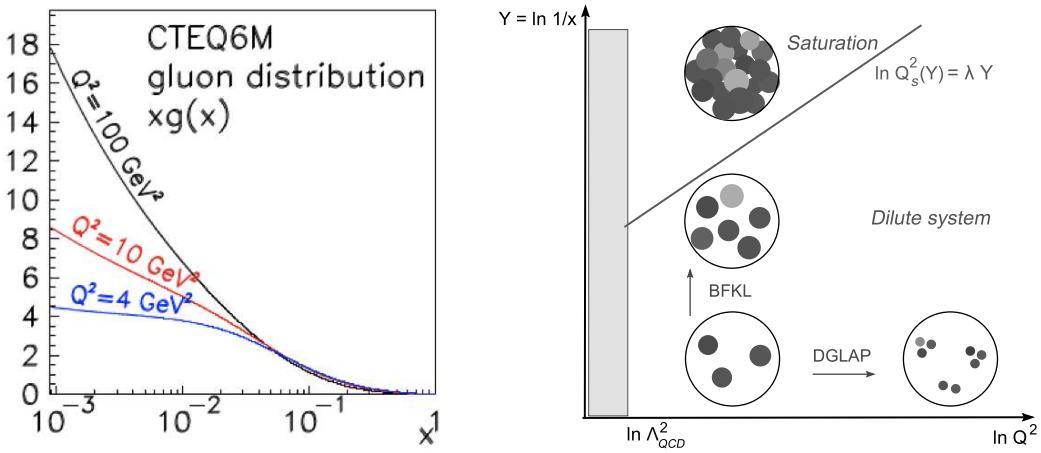

Figure 2.3: Left: Gluon density increases when x_{BJ} decreases at fixed Q^2 in CTEQ6M model [17]. Figure is taken from [24]. Right: pictorial representation of parton density function evolution in Q^2 (DGLAP) and x (BFKL), taken from [25]. Each circle represent the resolved parton with transverse size $1/Q^2$ and longitudinal momentum $k^+ = x_{BJ}P^+$ (P^+ is the longitudinal momentum of the nucleon in light cone frame).

The scale Q^2 plays a role like the observed resolution: the higher the Q^2 is the smaller transverse size the observed area inside the nucleon is. As Q^2 increases, more and more gluons are radiated which in turn splits into quark-antiquark pairs. The radiation of gluons produces the evolution of structure function, and this process is described in terms of parton density distribution $f_i(x, Q^2)$, where i = q or g is the parton flavor and Q^2 is the resolution scale. The evolution in Q^2 of the parton density can be described by a DGLAP (Dokshitzer-Gribov-Lipatov-Altarelli-Parisi) equation [2, 3, 4, 5],

$$\frac{\partial f_a}{\partial ln Q^2} \sim \frac{\alpha_S(Q^2)}{2\pi} \sum_b (P_{ab} \otimes f_b). \tag{2.15}$$

In equation 2.15, P_{ab} are the splitting functions that describe the probability of a parton splitting into parton a and parton b (e.g. $q \to qg$ or $g \to gg$) and they are given in a power series in α_S. Although the number of partons increases according to DGLAP evolution, the parton density decreases as the transverse resolution Q^2 increases.

After DGLAP evolution, the transverse size of parton becomes smaller. Although the number of parton increases, the parton system is dilute after DGLAP

evolution. The series contain terms proportional to lnQ^2 and to $ln(1/x_{BJ})$. In the very small x_{BJ} kinematic region, the DGLAP evolution can not compete with the evolution along $ln(x_{BJ})$ even when the transverse momentum transfer is large ($Q^2 \to \infty$). Balitsky-Fadin-Kuraev-Lipatov (BFKL) equation describes the gluon radiation dependence in orders of lnx_{BJ}. The BFKL equation predicts rapid growth of the gluon density while the transverse size of partons $(1/Q^2)$stays constant [6, 7, 8]. In BFKL evolution, the small x_{BJ} partons are produced overlapping with each other in the transverse coordinate space. As the gluon distribution function is much smaller in the large x_{BJ} region compared to quarks. For simplicity, gluons are treated as the only low x_{BJ} partons (the probability of finding a quark in the same low x_{BJ} region is lower than the gluon). As shown in the right panel of Figure 2.3, the transverse size of the parton decreases as Q^2 increases. When Q^2 is not large but still larger than Λ_{QCD}, the gluon density $x_{BJ}g(x_{BJ}, Q^2)$ grows rapidly with decreasing x_{BJ} at fixed Q^2 (see the left panel of Figure 2.3). More and more gluons are generated through gluon splitting (or emission). When the gluon recombination process balances the gluon splitting process, saturation is expected at a low x_{BJ} as the total cross section of hadronic scattering $\sigma(s)$ at a center of mass energy s is finite; and the cross section has a upper limit $\sigma(s) \leq \sigma_0 ln^2(s)$ (the Froissart bound) [21].

The gluon saturation of proton is expected to be below $x_{BJ} = 0.0001$, and this is hard to achieve at RHIC energy. If we change the target from a proton to a large nucleus (the atomic mass number A »1), as the protons and neutrons inside the large nucleus overlap with each other, there is probability to probe denser gluon density inside a large nucleus than a proton at the same x_{BJ}. In other words, the gluon saturation inside a large nucleus is expected to happen before the proton gluon saturation along x_{BJ}.

Unlike a dilute proton, multiple parton scattering in the rest frame of the nucleus (or a dense proton) corresponds to recombination in the infinite momentum frame [26, 27]. At low x_{BJ}, the gluon recombination begins to compete with further emission of gluons. Gluon recombination becomes important so that non-linear contributions to evolution equations must be included [27, 28]. Gribov, Levin and Ryskin first proposed a model (GLR model) that describes the parton density distribution at low x_{BJ} with fixed Q^2 with double log approximation of perturbative QCD [29, 26]. In GLR model, the modified evolution function with non-linear correction like gluon-gluon recombination expresses the tendency towards saturation without violating the unitarity of the hadronic scattering amplitude. In addition to this, a Color Glass Condensate (CGC) model which includes non-linear effects will be introduced later in this chapter. The dipole model which involves the interactions of gluons during the DIS scattering process will be introduced in the next subsection.

2.2.3 Dipole model

The Bjorken frame provides a first glimpse on gluon saturation and descriptions of the inner structure of hadron in parton level. In the DIS process, the lepton or

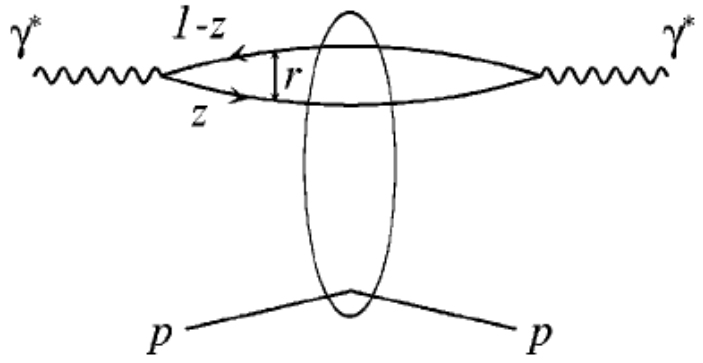

Figure 2.4: Interaction of a quark anti-quark dipole with the proton in deep inelastic ep scattering. Figure from [30].

neutrino interacts with a quark inside the nucleon or nucleus. The cross section of deep inelastic scattering (eg. ep scattering) is described proportional to virtual photon quark ($\gamma^* q$) process in perturbative QCD. The quark inside the nucleon or nucleus probed by the virtual photon is most likely a sea quark emitted by a gluon not a valence quark at low x_{BJ} region. Therefore, gluons can be indirectly probed in DIS processes.

At high center of mass energy, the incoming virtual photon with large transverse momentum splits into a quark-antiquark pair which then interacts with partons inside the nucleus at rest frame (See Figure 2.4). In the target frame, it is more straightforward to describe the gluon interactions. Then, the F_2 structure function of the nuclei can be rewritten as proportional to the propagator of the quark-antiquark ($q\bar{q}$) pair through the nucleon (or nuclei) [31, 32, 33, 34]. In the dipole frame, the cross section of DIS process can be factorized into the probability that a virtual photon fluctuates into a $q\bar{q}$ pair which can be well described by perturbative QCD and the cross section of $q\bar{q}$ dipole passing through the gluon cloud inside the nucleon (or nuclei).

As shown in Figure 2.4, the momentum of the virtual photon and the momentum of the proton are collinear (we can treat the proton as a target with translation). The quark anti-quark distribution is given in terms of z and $(1-z)$, the momentum fraction with respect to the virtual photon ($\gamma*$) momentum, and the relative transverse separation r. The $\gamma*$p cross section for transversely (T) and longitudinally (L) polarized photons $\sigma_{T,L}(x, Q^2)$ can be written as the following,

$$\sigma_{T,L}(x, Q^2) = \int d^2r \int_0^1 dz |\Psi_{T,L}(z, r)|^2 \hat{\sigma}(x, r^2), \tag{2.16}$$

where $\Psi_{T,L}$ is the photon wave function, and $\hat{\sigma}(x, r^2)$ is the dipole cross section. From [30], the dipole cross section can written as,

$$\hat{\sigma}(x, r^2) = \sigma_0 g(\hat{r}), \tag{2.17}$$

with

$$\hat{r} = \frac{r}{2R_0(x)}, \tag{2.18}$$

$$R_0(x) = \frac{1}{Q_0}(\frac{x}{x_0})^{\lambda/2}, \tag{2.19}$$

where $Q_0 = 1GeV$ and σ_0, x_0, and λ are free parameters to be determined by fitting. Assuming the gluon density is evenly distribute over a certain area with a sharp boundary, a simple ansatz is used in Ref [30] for function g,

$$g(\hat{r}^2) = 1 - e^{-\hat{r}^2}. \tag{2.20}$$

Scale $1/Q$ is introduced to stand for the transverse dimension of the $q\bar{q}$ pair [30]. After calculation, σ_T in Eq.(2.16) is $\sim \frac{1}{Q^2}\frac{\sigma_0}{R_0^2}$ when $1/Q$ is much smaller than the saturation radius R_0 ($1/Q << R_0$). When the transverse size $1/Q > R_0$, σ_T is $\sim \sigma_0 + \sigma_0 log(\frac{1}{Q^2R_0^2})$. This means the cross section σ_T is a constant in Q^2 for $1/Q > R_0$ and saturation is realized.

From Eq.(2.19), the transition from "hard" to "soft" regime for the cross section $\sigma_{\gamma * p}$ requires a critical line in x-Q^2 plane [30],

$$Q^2 = \frac{1}{Q_0^2}(\frac{x_0}{x})^{\lambda}. \tag{2.21}$$

Therefore the GBW dipole model [30] denotes the saturation scale $Q_s^2 = (x_0/x_{BJ})^{\lambda}$, where x_0 and λ are determined from fitting to the DIS data for $x \leq 0.01$. This definition leads to a straight line which clearly sepearates the saturated and the dilute parton system in a $\ln Q^2$(x)-ln (x) plane, as depicted on the right panel of Figure 2.3.

The dipole with high enough energy can evolve by emitting a gluon or more, and the radiated gluon can be described as a new color dipole. Thus the $\gamma^* q$ scattering amplitude including evolution has the probability of simultaneous interaction of two or more dipoles with the gluon fields of the nuclei. The reaction extends from single gluon exchange to multi-gluon exchange in the saturation region. The later part of $\gamma^* q$ interaction is treated with semiclassical methods. At a given impact parameter b, the cross section of quark anti-quark color dipole with relative transverse separation r passing through the gluon fields of a proton $x_{BJ}g(x_{BJ}, \mu^2)$ is,

$$\sigma_{q\bar{q}} \sim 1 - exp(-\alpha_s(\mu^2)x_{BJ}g(x_{BJ}, \mu^2))T(b), \tag{2.22}$$

where T(b) is the gluon density at impact parameter b which integrates over the longitudinal profile. This is known as the Glauber-Muller dipole cross section [35], and can also be derived from the McLerran-Venugopalan model [36, 37]. The Glauber-Muller dipole cross section is proportional to the transverse area of the dipole r^2 (color transparency) for small r, but approaches a const value when the dipole r goes large (the gluon density reaching saturation).

The nucleon parton density is determined by the global fit to the data [38, 39]. The nuclei parton density function is little known below $x_{BJ} < 0.02$ from the fixed

nucleus target DIS experiment. The distribution of nucleons inside a nucleus is assumed to obey a Woods-Saxon function [40], and the transverse density of nucleus with mass number A is proportional to $A^{2/3}$. Consequently, the saturation scale in nucleus is defined as following [41],

$$Q_s^2(x_{BJ}) \sim \alpha_s A^{1/3} x_{BJ} g(x_{BJ}, Q_s^2). \tag{2.23}$$

Therefore, saturation in the nuclear gluon density is expected to be realized at higher x_{BJ} value than the nucleon in the low x_{BJ} region at fixed Q^2. In a large composite system (nuclei), gluons emitted from the same spatial source exhibits saturation at low x_{BJ}. However, if gluons are emitted from spatially non-overlapping region with different rapidity intervals ($ln(1/x)$) (see Figure 1.2, in the $2 \to 2$ partonic scattering) or different transverse momentum region (lnQ^2), the saturation of the gluon density will not appear [35].

Instead of the electromagnetic probe (i.e. virtual photon), the nucleon (or nucleus) which can be treated as a bag of quarks or gluons is used to directly probe gluons inside the nucleon or nucleus. Therefore, the nuclear structure can be measured through hadron probes in hadron-hadron(or nucleus) interactions, while the energy of the hadron projectile needs to be higher than the energy of the virtual photon probe in deep inelastic scattering to probe the same low x_{BJ} region. A nucleus at high energy (e.g in high energy collision) is Lorentz-contracted and can be treated as a pancake. The nuclear scattering amplitude can be factorized into the probability of finding partons inside a nucleus, the parton multiple interaction scattering process, and the parton fragmentation into hadron process. The nuclear parton distribution function is the same as in deep inelastic scattering process. The hadron-hadron scattering cross sections with large Q^2 can also be factorized into short range interactions (hard scattering between quarks and gluons) and universal long range functions. Therefore, the hadron hadron scattering can be generally written as the convolution of probability of finding partons inside the hadrons, the elementary cross sections between partons, and the fragmentation functions of scattered partons into final states. For example, the cross section of $p + p \to h + X$ is,

$$E_h \frac{d\sigma^{pp\to hX}}{d^3p} = K \sum_{abcd} \int dx_a dx_b f_{a/p}(x_a, Q_a^2) f_{b/p}(x_b, Q_b^2) \times \frac{d\sigma}{dt}(ab \to cd) \times \frac{D_{h/c}(z_c, Q_c^2)}{\pi z_c}, \tag{2.24}$$

where $x_a = p_a/P_A$, $x_b = p_b/P_B$ are the initial momentum fractions carried by parton a over proton A or parton b over proton B , $z_c = p_h/p_c$ is the momentum fraction carried by hadron h over parton c, $f_{a/p}(x_a, Q_a^2)$ or $f_{b/p}(x_b, Q_b^2)$ are parton distribution functions and $D_{h/c}(z_c, Q_c^2)$ is the fragmentation function for a parton c to fragment into hadron h [42]. The parton distribution functions and fragmentation functions are determined from global fits based on experimental results.

2.3 Color Glass Condensate

The Color Glass Condensate (CGC) theory is an effective field theory describing a dense state of incoherently interacting gluons. The gluons carry color charges and exhibit disordered and condensate states. These gluons are generated by fast partons at large rapidity and they are Lorentz time dilated in center of mass frame. This state is like solid in short time scale and liquid in long time scale. Such disordered states are like "spin glass" [43, 44].

A modified coupling constant, which depends on the multiplicity of the particles per unit rapidity per unit area, is used to solve the many body problems in the kinematics of the partons at low x_{BJ} inside nuclei. The nucleus with high speed (near the speed of light) is compressed along the direction of its motion. The nucleus looks like a pancake in the dimension of the Lorentz-contracted length R_N/γ_N where R_N is the radius of the nucleus and γ_N is the gamma factor of the nucleus in the center of mass frame. The coupling between valence quarks of the dense nucleus at low x is assumed to be weak. The dominant mechanism of parton production around the fast moving valence quarks is bremsstrahlung and chains of bremsstrahlung from bremsstrahlung particles. The average color charge around the valence quarks is zero, and the color charges are generated only through fluctuations. Therefore the fast partons (i.e. valence quarks) play the role as static and recoilless sources of color charges [45, 46, 47].

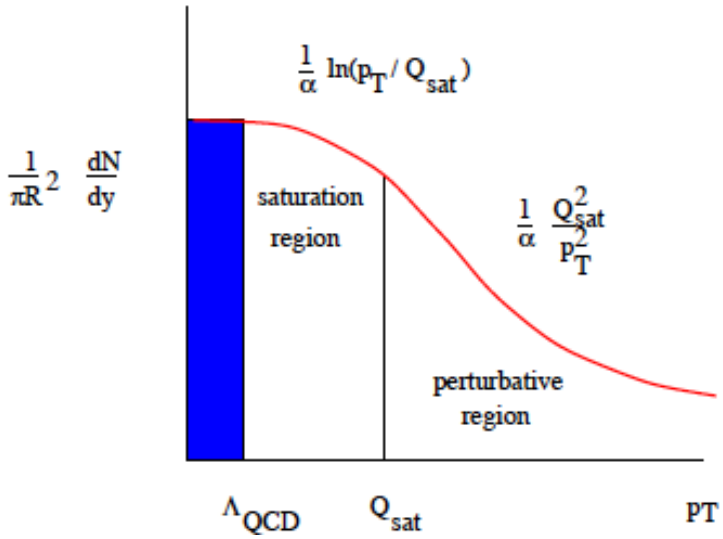

Figure 2.5: The gluon density per unit transverse area per unit rapidity versus transverse momentum. Figure from [43].

Although the CGC state is weakly coupling at small x_{BJ}, this does not mean it can be dealt with by perturbative QCD. The number of gluons per unit area per

unit rapidity is defined as following [45],

$$\Lambda^2 = \frac{1}{\pi R^2}\frac{dN}{dy}, \tag{2.25}$$

where R is the nucleus radius, and πR^2 is the cross section of hadronic scattering from nucleus. See the local gluon distribution $\frac{1}{\pi R^2}\frac{dN}{dy}$ in Figure 2.5. Since the coupling scale $\alpha_S(\Lambda) \ll 1$, the local density is high,

$$\Lambda^2 \gg \Lambda^2_{QCD}. \tag{2.26}$$

The empirical parameterization form of the gluon density is,

$$\frac{1}{\pi R^2}\frac{dN}{dy} \sim \frac{A^{1/3}}{x^{\delta}_{BJ}}, \tag{2.27}$$

where A is the mass number of the nucleus, δ is a fit parameter on experimental results. As the typical transverse momentum scale of the constituents of the nucleus is nearly equal to Λ ($\Lambda^2 \gg 1/R^2$), the nucleus can be treated as a thin sheet (Lorentz contracted along moving direction) with infinite transverse area. The rapidity of the produced hadron y can be written in the form of the constituent of the colliding hadron y_{parton} in hadron-hadron scattering,

$$y \sim y_{parton} - ln(1/x_{BJ}). \tag{2.28}$$

We can probe low x_{BJ} partons through forward particle measurements. In theoretical physics, light cone gauge is an approach to remove the ambiguities arising from a gauge symmetry. While the term refers to several situations, a null component of a field A is set to zero (or a simple function of other variables) in all cases. In light cone gauge, the saturation scale Q_s is defined as [43],

$$Q_s^2 \sim \alpha_s^2 \int dx^- \mu^2, \tag{2.29}$$

where $\int dx^- \mu^2$ stands for the color charge square per unit transverse area, where $x^- = (x_0 - x_3)/\sqrt{2}$ ($x^+ = (x_0 + x_3)/\sqrt{2}$) and other coordinates x_1 and x_2 are spatial and they are defined as $x_\perp$.

Assuming the initial transvere momentum scale $Q \gg Q_s$, the local gluon density rises as a order of Q_s^2. The saturation scale Q_s increases rapidly as x_{BJ} decreases to 0. As a result, Q_s eventually become larger than Q. Then, the slope of the increasing distribution becomes smaller. The local number of gluons rises like $ln(1/Q_s)$. Finally, the number of gluons stops growing and the cross section saturates. The problem of unitary of cross section in BFKL evolution is solved by the CGC theory.

2.3.1 The Extended Scale in Color Glass Condensate

The Color Glass Condensate (CGC) theory contains two types of degrees of freedom for gluons depending on the longitudinal momentum k^+. The fast gluon with $k^+ >>$

Λ is frozen by the Lorentz time-dilation. The slow gluon with $k^+ >> \Lambda$ can be described by the normal QCD field. The color field of the fast gluon ρ_A is treated as the source of the slow gluons, and ρ_A varies event by event. The CGC theory provides a gauge invariant formalism to predict the form of ρ_A. In very small x_{BJ} (the saturation region), the dynamics of the partons inside hadron or nuclei is only controlled by the saturation scale Q_s^2. A widely used factorization in the CGC frame is k_T factorization which can be applied on partons with $k_T >> Q_s$. The k_T factorization gives unintegrated k_T dependent quark or gluon distribution function, and the related calculations on gluon distribution are reproducible [48, 49].

In the CGC state, the fast gluons (larger x_{BJ}) evolve with normal time scale $1/Q_s$ and can be treated as "frozen color source" in high energy nucleus. The soft gluons (lower x_{BJ}) emitted by the fast gluons are dynamical around the static color source. The life time of low x_{BJ} parton is around x_{BJ}, therefore the slow gluons have short life time than the fast color sources. The evolution of fast partons in CGC state with decreasing x_{BJ} can be described by JIMWLK (Jalilian-Marian, Iancu, McLerran, Weigert, Leonidov, Kovner) function [50, 51, 52, 53]. Scale $\Lambda_+ = xP_+$ is used to separate the frozen color source and the dynamic color field in nucleon with momentum P_+. The probability of the color source ρ is described by function $W_{\Lambda_+}[\rho]$. The evolution of $W_{\Lambda_+}[\rho]$ with Λ_+ is,

$$\frac{\partial W_{\Lambda_+}[\rho]}{\partial ln(\Lambda_+)} = -\hat{H}[\rho, \frac{\delta}{\delta\rho}]W_{\Lambda_+}, \tag{2.30}$$

where $\hat{H}$ is the JIMWLK Hamiltonian, the detailed formulae can be found in [50, 51, 52, 53].

Assuming the factorization mechanism is universal, the parton distribution function $f_{a/p}(x_a, Q_a^2)$ and fragmentation function $D_{h/c}(z_c, Q_c^2)$ which were determined in deep inelastic scattering experiments can also be applied in the hadron-hadron interaction processes. There are two parton distribution functions involved in the hadron-hadron interactions which are related with more QCD interactions than deep inelastic scattering. Therefore, hadron-hadron interaction is a more complex process than the deep inelastic scattering. Nucleus-nucleus interaction has similar structure as mentioned in Eq.2.24, and the difference is changing the proton parton distribution to nuclear parton distribution function.

We define the rapidity variables $\tau \equiv ln(1/x) = ln(P^+/\Lambda^+)$ and $\Delta\tau = ln(\Lambda^+/k^+)$ [54]. τ can be treated as a evolution time scale, and the saturation scale Q_s is expected to increase exponentially with τ. In the large N_c limit, Balitsky firstly derived the evolution form of the two point function of the Wilson lines (which represents the S-matrix element for dipole-hadron scattering) [55]. This formula is known as Balitsky-Kovchegov (BK) equation. The BK equation is based on the target frame like the CGC formulation. It works well in asymmetric collision between a high energy dipole and a dense hadronic target (e.g. a nucleus). Figure 2.6 shows the scattering amplitude of hadronic interactions N_τ as a function of rapidity difference

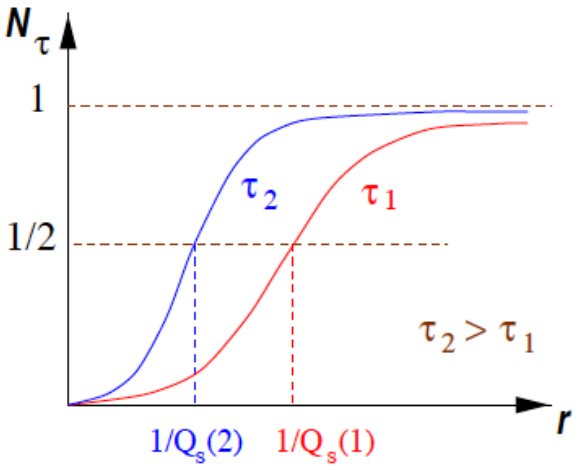

Figure 2.6: The scattering amplitude of hadronic interactions versus $\tau = ln(1/x)$ for two values of τ.

$r_\perp$. The saturation condition for N_τ gives the leading order extend scale for $Q_s^2(\tau)$,

$$Q_s^2(\tau) = Q_0^2 e^{c\alpha_s \tau}, \tag{2.31}$$

where c = 4.84. For $r_\perp$ is close to $1/Q_s$, the scattering amplitude can be written in,

$$N_\tau \approx (r_\perp^2 Q_s^2(\tau))^\gamma, \tag{2.32}$$

where γ is a fitted parameter from experiment. Eq.(2.32) can be expanded in powers of $ln(\frac{1}{r_\perp^2 Q_s^2(\tau)})/ln(\frac{Q_s^2(\tau)}{Q_0^2})$ with $ln(\frac{Q_s^2(\tau)}{Q_0^2}) = c\alpha\tau$. This approximation works for $1 < ln(\frac{1}{r_\perp^2 Q_s^2(\tau)})$. The dipole transverse resolution $Q^2 = 1/r_\perp^2$, and the condition can be represented as a scaling window,

$$Q_s^2(\tau) << Q^2 << \frac{Q_s^4(\tau)}{Q_0^2}. \tag{2.33}$$

The upper boundary in Eq.(2.33) shows a wider window for $Q_s^2(\tau)$. Considering the running coupling α_s is proportional to $ln(1/\Lambda_{QCD})$, the saturation scale Q_s is set by Λ_{QCD} rather than Q_0. Therefore Eq.(2.33) can be written as [56],

$$Q_s^2(\tau) << Q^2 << \frac{Q_s^4(\tau)}{\Lambda_{QCD}^2}. \tag{2.34}$$

Eq.(2.34) indicates that there is a transition region from dilute parton gas to the CGC state. Figure 2.6 shows the smooth transition with two different τ values. The extended scale is also represented in the right panel of Figure 2.3.

The Bjorken scaling variable x_{BJ} is defined as $x_{BJ} \sim Q^2/(2p \cdot q)$ (see Eq 2.6) in DIS experiments. In hadron(nucleus)-hadron(nucleus) scattering process, the partonic interaction is treated as $2 \to 2$ partonic scattering at leading order. In

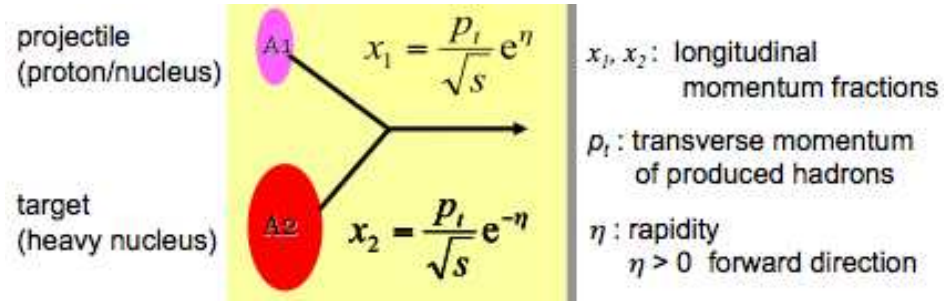

Figure 2.7: Schematics of light nucleus A_1 and heavy nucleus A_2 scattering process. Figure from [57].

the leading order of $2 \to 2$ elastic partonic scattering with collinear assumption and ignoring the mass of the parton, the final state parton carried momentum fraction x_1 and x_2 are defined as follows,

$$x_1 = \frac{p_T}{\sqrt{s}}(e^{\eta_1} + e^{\eta_2}), \tag{2.35}$$

$$x_2 = \frac{p_T}{\sqrt{s}}(e^{-\eta_1} + e^{-\eta_2}), \tag{2.36}$$

where $\sqrt{s}$ is the center of mass energy, p_T is the transverse momentum of produced hadron, and η_1 (η_2) is the pseudo-rapidity of produced hadron from parton carrying momentum fraction x_1 (x_2). If one of the final hadrons is generated at forward rapidity η, the momentum fraction can be approximated $x_1 = \frac{p_T}{\sqrt{s}} e^{\eta}$ and $x_2 = \frac{p_T}{\sqrt{s}} e^{-\eta}$. Asymmetric nucleus-nucleus collisions provide good paths to probe low x_{BJ} gluons in heavy nucleus. The schematics of scattering of light nucleus A_1 and heavy nucleus A_2 are shown in Figure 2.7. A parton from the projectile A_1 carrying longitudinal momentum fraction $x_1 = \frac{p_t}{\sqrt{s}} e^{\eta}$ interacts with another parton from the target A_2 with longitudinal momentum fraction $x_2 = \frac{p_t}{\sqrt{s}} e^{-\eta}$. Here p_t is the transverse momentum of produced final hadrons. For forward scattering ($\eta >> 0$), $x_1 \to 1$ (valence quark) and x_2 is very small (soft gluons). Take the deuteron gold collision for example, the probed x_{BJ} of soft gluons in the gold nuclei is around 0.001 at center of mass $\sqrt{s} = 200GeV$. Therefore, forward particles production is sensitive to low x_{BJ} region.

In addition to the theory models, a series of high energy experiments tried to probe low x_{BJ} gluons. We will begin with the observed "Geometric Scaling" in DIS experiment. Then we will introduce the inclusive hadron measurements at RHIC. The forward hadron suppression in d+Au collisions at RHIC is in agreement with CGC description. Correlations of di-hadron are more sensitive to x_{BJ} low gluons. Details of the di-hadron correlations will be introduced in the following section.

2.4 Phenomena in experiments

2.4.1 Geometric Scaling

The dipole nucleus cross section can be written in a phenomenological form [58, 59],

$$\hat{\sigma}(x_{BJ}, r) = \sigma_0\{1 - exp(-\frac{r^2}{rR_0^2(x_{BJ})})\}, \tag{2.37}$$

where r is the dipole transverse radius, σ_0 is the normalization independent of x_{BJ}. The saturation radius $R_0(x_{BJ})$ is defined as,

$$R_0(x_{BJ}) = \frac{1}{Q_0^2}(\frac{x_{BJ}}{x_0})^{\lambda}, \tag{2.38}$$

where $Q_0^2 = 1GeV^2$, and $R_0(x_{BJ}) = 1/Q_S(x_{BJ})$. Rescaling r to $\hat{r} \equiv r/R_0$, the virtual photon proton cross section $\sigma_{\gamma^* p}$ becomes a function of new dimensionless scale $\tau = Q^2 R_0^2(x_{BJ})$. The phenomena are known as geometric scaling in the small x_{BJ} region. Figure 2.8 shows the DIS experimental data on $\sigma_{\gamma^* p}$ versus the dimensionless scale τ.

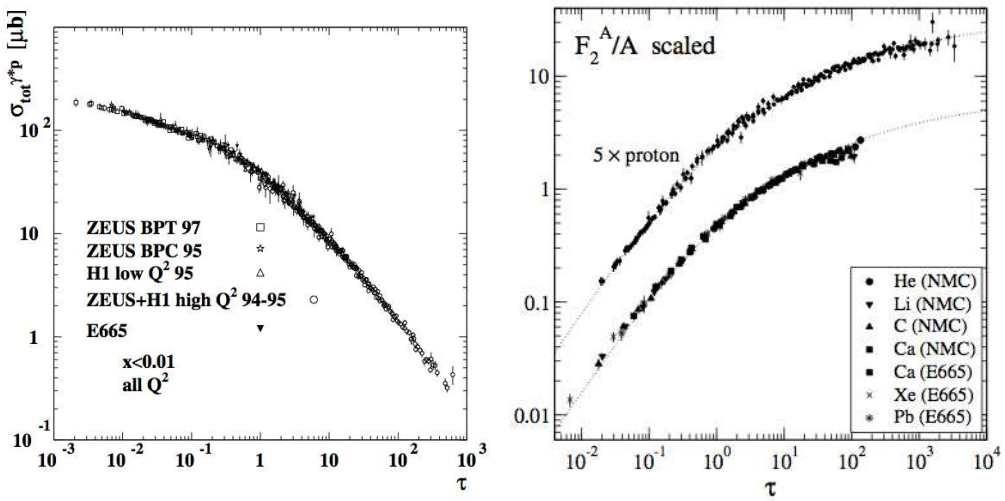

Figure 2.8: Left panel: Experimental data on virtual photon proton cross section $\sigma_{\gamma^* p}$ versus dimensional variable $\tau = Q^2 R_0^2(x_{BJ})$ for $x_{BJ} < 0.01$ and Q^2 between 0.045 and $450GeV^2$ region. Figure from [59]. Right panel: F_2^A/A versus $\tau = (\frac{x_{BJ}}{x_0})^{2\lambda}\frac{Q^2}{A^{1/3}}$. Figure from [60].

The cross section of $\gamma^* p$ reaction is then,

$$\sigma_{tot}(x_{BJ}, Q^2) = \sigma_{tot}(x_0, \frac{Q^2}{Q_s^2(x_{BJ})}Q_0^2). \tag{2.39}$$

The total cross section $\sigma_{\gamma * p}$ has an asymmetric dependence on $1/\tau$ from the left panel of Figure 2.8. At small τ, less steep of the cross section $\sigma_{\gamma^* p}$ corresponds to

the saturation of the dipole cross section. The saturation scale $Q_s \sim 1/R_0(x_{BJ})$ which characterizes dense parton system is embedded in the geometric scaling. With Q_s changes by a factor of $Q^{\frac{1}{3}}$, the leading order nuclear shadowing effect can be incorporated within non-linear pQCD. As structure function $F_2 \sim \sigma \cdot Q^2$, Eq 2.39 can be rewritten as,

$$(\frac{x_{BJ}}{x_0})^{2\lambda}\frac{F_2^A(x_{BJ},Q^2)}{A} = F_2^p[x_0,(\frac{x_{BJ}}{x_0})^{2\lambda}\frac{Q^2}{A^{1/3}}]. \quad (2.40)$$

This suggests $\frac{1}{A}F_2^A$ versus $\tau = (\frac{x_{BJ}}{x_0})^{2\lambda}\frac{Q^2}{A^{1/3}}$ has the same curve as for F_2^p [60]. From the plot in the right panel of Figure 2.8 which shows the experiment data on F_2^A/A as a function of τ, F_2^A has similar scaling as F_2^p. The geometric scaling are also found in eA DIS scattering experiments (eg. NMC and E665) [61]. The geometric scaling proves the existence of saturation scale Q_s in DIS processes and opens new window for extending scaling regime $k_t < Q_s^2/\Lambda_{QCD}$ [62].

2.4.2 Inclusive particle measurements

As we discussed in previous section, forward production in hadron(nucleus)-hadron(nucleus) interactions provides a path to probe low x_{BJ} gluons. Such process usually is realized by a large $x_F \sim x_1$ ($x_F \equiv \frac{p_L}{2\sqrt{s}}$, see the x_1 definition in Eq2.35) quark from one proton and a soft $x_{BJ} \sim x_2$ (see x_2 definition in Eq2.36)gluon from the other proton. The d+Au collision is using dilute system (deuteron nuclei) to probe the structure of dense system (gold nuclei). The forward particle production favors the interactions between a hard quark from the projectile deuteron nuclei and a soft gluon inside the gold nuclei. From HERA data [13, 14], the saturation x_{BJ} is expected to be around 10^{-4} in p+p collisions. At RHIC current energy, it is hard to reach the saturation region in p+p collision. In nucleus-nucleus collision, the saturation scale Q_s^2 has A (nuclei mass number) dependence. Therefore, the related x_{BJ} is expected to be higher in nucleus-nucleus collisions than p+p collisions.

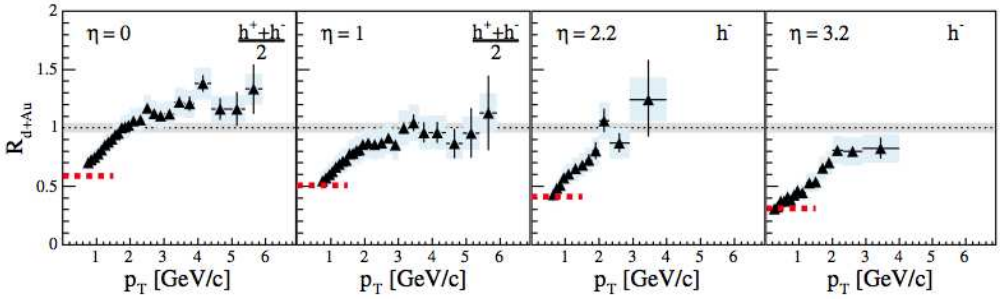

Figure 2.9: Nuclear modification factor R_{dAu} for charged particles versus transverse momentum p_T at pseudo-rapidity η = 0, 1, 2.2 and 3.2. Figure from [63].

The BRAHMS experiment at RHIC has observed forward charged particle production suppression in d+Au collision, and Figure 2.9 shows the measured nuclear

modification factor R_{dAu} at the BRAHMS experiment in $\sqrt{s} = 200GeV$ d+Au collisions [63]. R_{dAu} gives the relative ratio between yields from d+Au collisions and the scaled yields from p+p collisions,

$$R_{dAu} \equiv \frac{1}{< N_{coll} >} \frac{d^2N^{d+Au}/dp_T d\eta}{d^2N^{p+p}_{inel}/dp_T d\eta}, \tag{2.41}$$

where $< N_{coll} >$ is the mean number of binary collisions. At midrapidity, R_{dAu} for charged particles presents a Cronin enhancement with $p_T > 2GeV/c$, and it reduces smoothly as the rapidity increases until the suppression appears at forward rapidity (see Figure2.9). In addition to charged particles, the neutral pion R_{dAu} measured at STAR experiment shows suppression at forward rapidity. Consider the isospin effect, the scale agrees with charged particle results [64]. The inclusive π^0 cross section in p+p collisions can be well described by next-to-leading order (NLO) pQCD, while the results in d+Au collisions have better agreements with CGC theory predictions.

The suppression of particle productions at forward rapidity, which is consistent with onset of saturation in the gold nuclei gluon density, can be explained by CGC theory. Forward particle production in d+Au interactions is dominated by quark-gluon scattering process, which is used to probe the nuclei gluon density of the gold nuclei at low x_{BJ} region. The momentum scale of the saturation region is related with the saturation scale $Q^2 \sim A^{1/3}e^{\lambda}y$ of the nuclei gluon density. A is the mass atomic number of the nuclei, y is the rapidity of the final hadron state (in forward region, rapidity y $\sim$ pseudo-rapidity η) and $\lambda \sim 0.2 - 0.3$ is a fit paramter from HERA measured F_2 structure function. The saturation effect gets enhanced in the forward region (at high center of mass energy $\sqrt{s}$, pseudo-rapidity $\eta \sim$ rapidity y). The average x_{BJ} can go to $\sim 10^{-4}$ with $\eta = 4$ of produced pion [65].

2.4.3 Correlation measurements

Forward inclusive particle production only measures an average x_{BJ} region; the higher the pseudo-rapidity η is the lower x_{BJ} it probes. The coincident correlation measurements can limit the broad x_{BJ} range to a certain region for the probed soft gluon as shown in the left panel of Figure 2.10 [66]. The left panel of Figure 2.10 is based on leading order kinematics; the d+Au interaction considers nuclear shadowing and anti-shadowing effect. With the associated π^0 measured in the forward rapidity, the sensitive gluon x_{BJ} can go below 0.01 which is beyond the fixed target experiment measured region (see Figure1.2).

STAR experiment explored the first di-hadron correlation measurement at RHIC to emphasize the low x_{BJ} phenomenon [64]. Figure 2.10 shows the coincidence probability of a forward π^0 ($< \eta > \sim 4$) and a leading mid-rapidity charged hadron h^{pm} ($|\eta| < 0.75$) in p+p collisions and d+Au collisions at center of mass energy $\sqrt{s} = 200GeV$. At lower E_π, the back-to-back correlation peak in d+Au collisions is smaller than in p+p collisions. This result is expected by mono-jet coherent scattering predictions [67, 68] and CGC models [69].

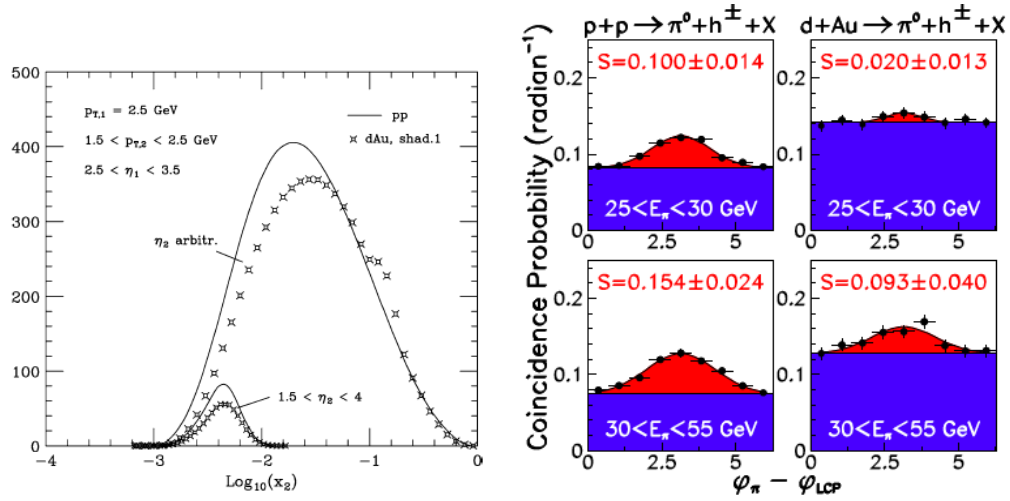

Figure 2.10: Left panel: leading order (LO) kinematics of $log_{10}(x_2)$ (x_2 definition in Eq. 2.36) of cross section $d\sigma/dp_{T,1}$ for $p+p \to \pi^0+\pi^0+X$ and $d+Au \to \pi^0+\pi^0+X$ processes at $\sqrt{s} = 200GeV$. Top histograms are for unconstrained η_2 and the bottom ones are for $1.5 \leq \eta_2 \leq 4$. This figure is from [66]. Right panel: Coincidence probability of a forward π^0 and a mid-rapidity leading charged particle azimuthal correlations at STAR experiment. Figure from [64].

With the large granularity Forward Meson Spectrometer (FMS) installed at STAR and high luminosity RHIC run8 p+p and d+Au collision data, we measured di-hadron azimuthal correlations at different rapidities with fixed Q^2 to probe a path from dilute parton system to possible dense CGC state as shown in the right panel of Figure 2.3. Figure 2.11 shows the forward $\pi^0 - \pi^0$ azimuthal correlations in PYTHIA 6.222 simulation. The pseudo-rapidity of the associated π^0 is related with the x_{BJ} of the soft gluon involved in the partonic scattering. Simulation studies with different parton distributions as input shows that the azimuthal correlation peak is closely related with gluon density distribution [11].

The forward-forward π^0-π^0 azimuthal correlations in d+Au collisions are found to be broader than that in p+p collisions [10]. With centrality selection, suppression of the back-to-back correlations are seen in the central d+Au collisions which indicate the forward-forward correlation approach saturation region for nuclei gluon density [11]. The suppression of back-to-back azimuthal correlation in central d+Au collisions (see Figure 2.12) can be well determined in CGC models [71]. In the forward + mid-rapidity azimuthal correlations, there is no significant broadening from p+p collisions to d+Au collisions on the back-to-back peak [12]. Recent theory calculations from effective "k_t factorization" including $q + g$ and $g + g$ $2 \to 2$ partonic scattering describe forward-forward correlations in both peripheral and central dAu collisions very well [72]. One model which is also based on "k_T factorization" calculates the azimuthal correlations from $2 \to 4$ partonic scattering [73]. Although the "k_T factorization" mechanism fails in the saturation region, the forward-central

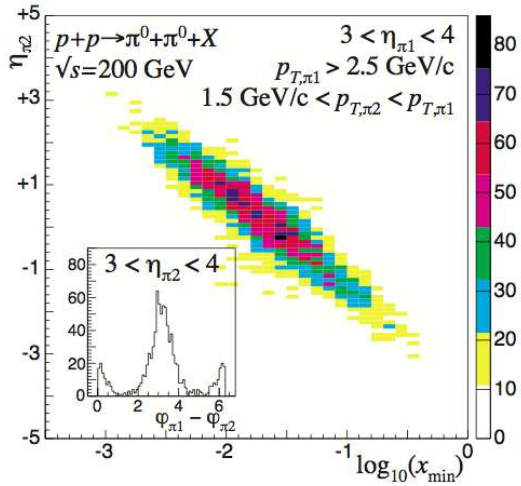

Figure 2.11: PYTHIA 6.222 simulation of forward $\pi^0 - \pi^0$ azimuthal correlations in p+p collisions at $\sqrt{s} = 200GeV$. The x_{BJ} of the soft gluon involved in the partonic scattering is correlated with pseudo-rapidity η_{π_2} of the associated π^0. Figure from [24].

azimuthal correlations are reproducible with this method.

Currently, the di-hadron correlation with pseudo-rapidity gap $|\Delta\eta| \sim 1$ remains a challenge for theory calculations. In the large coverage STAR electromagnetic calorimeter system, the Endcap ElectroMagnetic Calorimeter (EEMC) sits between the forward rapidity FMS and the mid-rapidity Barrel ElectroMagnetic Calorimeter (BEMC) with pseudo-rapidity $1.08 < \eta < 2$ and full azimuthal coverage. Therefore the azimuthal correlations between one hadron measured in the FMS and the other hadron measured in the EEMC probe the intermediate x_{BJ} region between forward+forward correlations and forward+mid-rapidity correlations. The FMS-EEMC di-hadron correlation analysis is the main concept of this thesis and will be introduced in the following chapters.

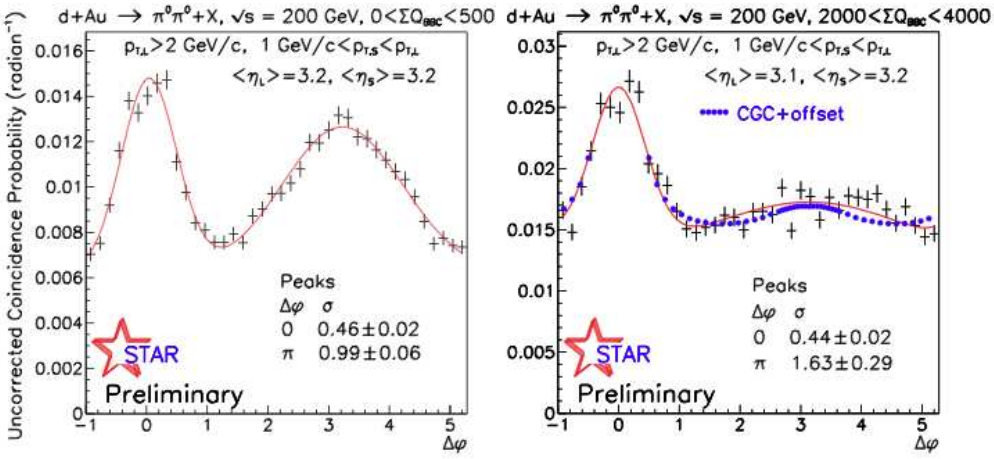

Figure 2.12: The uncorrected coincidence probability of forward forward $\pi^0 - \pi^0$ azimuthal correlations in central d+Au collisions. Data are in good agreement with CGC expectation [70]. Figure from [11].

Chapter 3

Experiment: detector setup

3.1 Relativistic Heavy Ion Collider(RHIC)

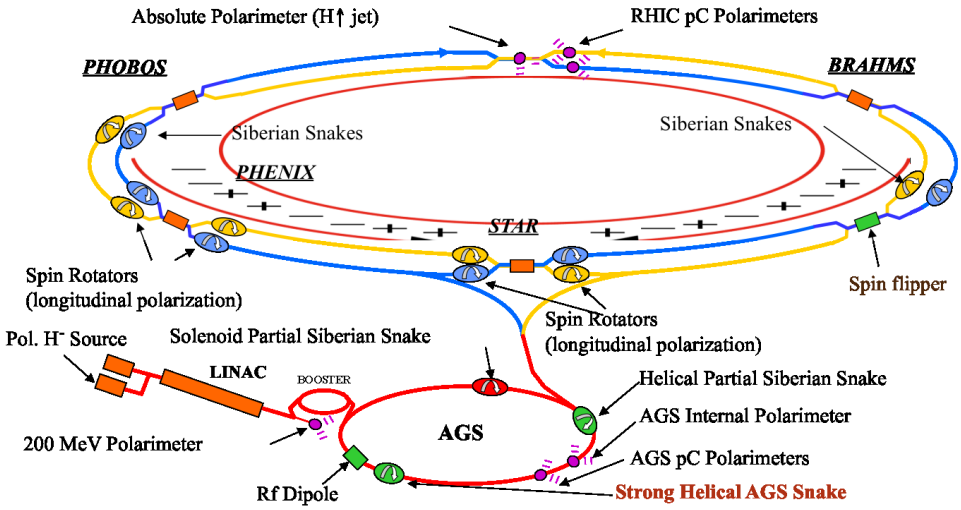

Figure 3.1: The schematics of Relativistic Heavy Ion Collider (RHIC) at Brookhaven National Laboratory

.

The Relativistic Heavy Ion Collider (RHIC) at Brookhaven National Laboratory is one of the heavy ion colliders and the unique spin-polarized proton-proton collider. The main physical goals of RHIC are (1) the study of the high density and high temperature state of matter shortly after the "Big Bang". This phase which is called "quark-gluon plasma (QGP)" or "quark soup" consists of asymptotically free quarks and gluons. This can be achieved at RHIC by Au+Au collisions at center of mass energy $\sqrt{s} = 200GeV$. (2) the study of the spin structure of the proton. By using polarized proton proton at different center of mass energy ($\sqrt{s} = 200GeV$ or $500GeV$), the resolution to the "spin puzzle" (valence quarks only contribute less than 30% to the proton spin) is being explored at RHIC.

RHIC is now the second highest energy heavy ion collider in the world since November 2010, the large hadron collider (LHC) at the European Organization for

Nuclear Research (CERN) started operating heavy ion collisions. Two independent storage rings (denoted as "Blue" and "Yellow" rings) circulate charged particles in opposite directions. The main particle combination groups at RHIC are p+p, d+Au, Cu+Cu and Au+Au. The particles travel the 3.8 kilometer ring at a speed of 99.995% of the speed of light. The center of mass energy varied for different collision particle projectiles, for polarized p+p collision, run-9 achieved 500GeV center of mass energy in February 2009.

The RHIC collider works as follows: The particles first pass the Tandem Van de Graaff accelerator, the Tandem uses static electricity to remove some electrons of the atoms. For example, gold nuclei leave the Tandem with energy about 1 MeV per nucleon and have an electric charge of +31e. The bunches of ions are then injected into the Booster Synchrotron. Protons need to be pre-accelerated in the 200MeV Linear Accelerator (Linac) before transferred to the Booster. The ions observe more energy at the Booster Synchrotron up to 95MeV per nucleon. Bunches of ions are further ionized as they reach the Alternating Gradient Synchrotron (AGS) from the Booster. In the AGS, particles are brought to an energy of 10GeV per nucleon and the charge of the ions equal to their atomic numbers (eg. gold nuclei get +79e charge). Before the ions are injected into the RHIC ring, there is a switching magnet divides the ion bunches into two beams (one in clockwise-circulating and the other in counterclockwise direction) at the end of the AGS-To-RHIC transfer line. The particle beams circulate with the opposite directions in the two RHIC rings, the heavy ions are accelerated up to 100GeV per nucleon and protons up to 250GeV. For polarized proton beams, there are specialized magnet sets called "Siberian snakes" to minimize the polarization loss.

One store can last several hours and defined as "fill", one "fill" is further divided into several runs. Usually, p+p run has longer store time than Au+Au or d+Au run due to smaller inner beam scattering effect. The longitudinal spread of a typical beam bunch is 25 cm. And there are eight spin rotators which rotate the beam polarization directions with one mounted inside a modified RHIC dipole magnet cryostat. There are six intersection points where the two accelerating magnet rings cross. The beam polarization measurements are realized by polarimetry. The fast relative polarimeters at RHIC are based on the asymmetry in proton-carbon (pC) elastic scattering in the Coulomb-nuclear interference (CNI) region. The hydrogen jet polarimetry is the absolute polarimetry which provides the calibration of the pC CNI polarimeter. The schematics of the RHIC are shown in Figure 3.1. The main RHIC detectors are located at two of these intersection points: STAR[74] and PHENIX[75].

3.2 Solenoid Tracker at RHIC (STAR)

The STAR detector (Solenoidal Tracker at RHIC) is one of the two experiments at RHIC. One primary physical task of STAR is to investigate the behavior of strongly interacting matter at high energy density and to search for signatures of the quark

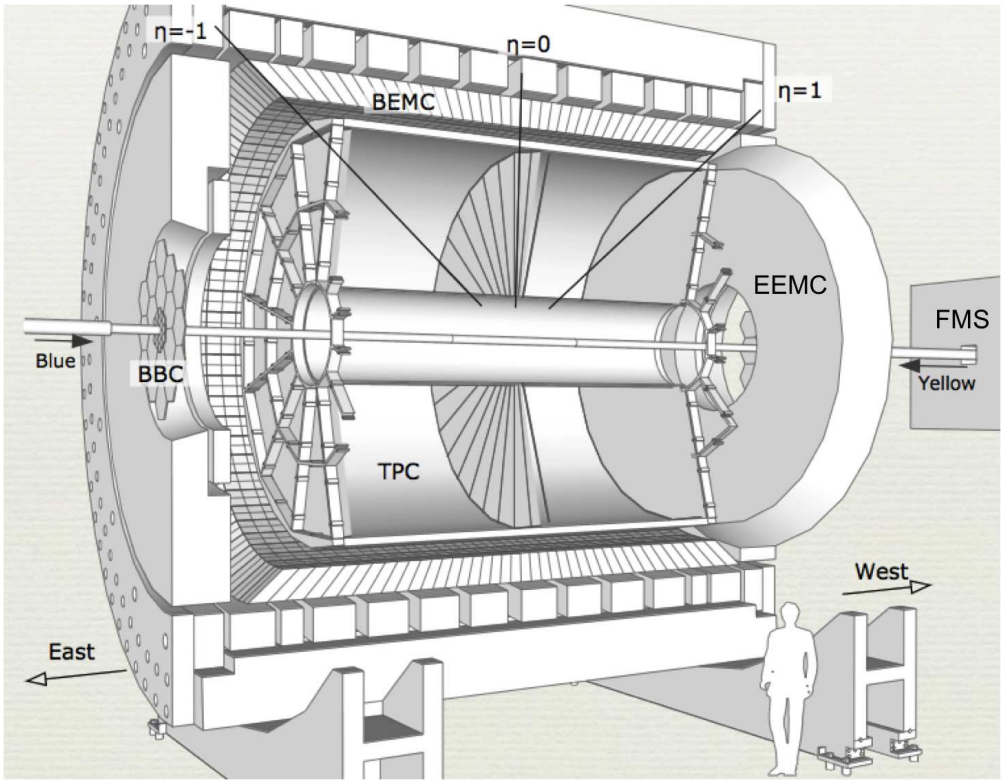

Figure 3.2: The STAR detectors. The midrapidiy detectors include the Time Projection Chamber (TPC, $-1 < \eta < 1$), the Barrel ElectroMagnetic Calorimeter (BEMC, $-1 < \eta < 1$) and the Endcap ElectroMagnetic Calorimeter (EEMC, $1.083 < \eta < 2$). The FMS ($1.5 < \eta < 4.0$) sits in the forward rapidity. Figure from [76].

gluon plasma (QGP) formation. Another physics goal is to study the internal spin structure of the proton. This requires measurements of a large number of particles simultaneously. STAR is designed for measurements of hadron production over a large solid angle, featuring detector systems for high precision tracking and nearly full azimuthal coverage continuous electromagnetic detectors. The 3D frame of STAR detectors are shown in Figure 3.2.

STAR consists of several types of detectors, each specializing in detecting certain types of particles or characterizing their motion. A large volume Time Projection Chamber (TPC) which covers the pseudo-rapidity range $|\eta < 1.0|$ is the main source of particle identification in the mid-rapidity for STAR. The TPC records the tracks of particles by measuring their ionization energy loss (dE/dx) over a large distance. The Time Of Flight (TOF) installed in the outer radius of the TPC provides higher resolution for $p_t > 1GeV/c$ pions, kaons and protons. The outermost middle-rapidity detector is the Barrel ElectroMagnetic Calorimeter (BEMC). It covers the same pseudo-rapidity range of the TPC with full azimuthal acceptance. The BEMC is designed to detect the deposited energy of the photons, electrons and electromagnetically decaying hadrons. The solenoid magnet are placed outside the BEMC and

it provides 0.5T magnetic field for the TPC. Two forward TPC (FTPC) models provide tracking ability at pseudo-rapidity range $2.5 < |\eta| < 4.0$. During RHIC run8 p+p and d+Au collisions, the Endcap ElectroMagnetic Calorimeter (EEMC) which covers pseudo-rapidity $1.083 < \eta < 2.0$ also recorded events. The Forward Meson Spectrometer (FMS) is the most forward electromagnetic calorimeter in STAR. It is a high granularity neutral meson spectrometer with large acceptance in pseudo-rapidity $2.5 < \eta < 4.0$ and full azimuthal coverage. The FMS plays an important role in the correlation analysis, the leading particles are measured in it. In p+p interactions, the Beam-Beam Counters (BBC) which are scintillators annuli provide minimum bias trigger. They are mounted around the beam pipe at 3.7 meters from the nominal interaction point. The Zero Degree Calorimeter (ZDC) models provide the trigger conditions in d+Au interactions. They are located between the DX dipole magnets and the D0 dipole magnets, sited near the RHIC rings 18 meters from the interaction point near the RHIC ring. The detectors that are relevant with the data analysis are described further in the following sections.

3.2.1 Time Projection Chamber

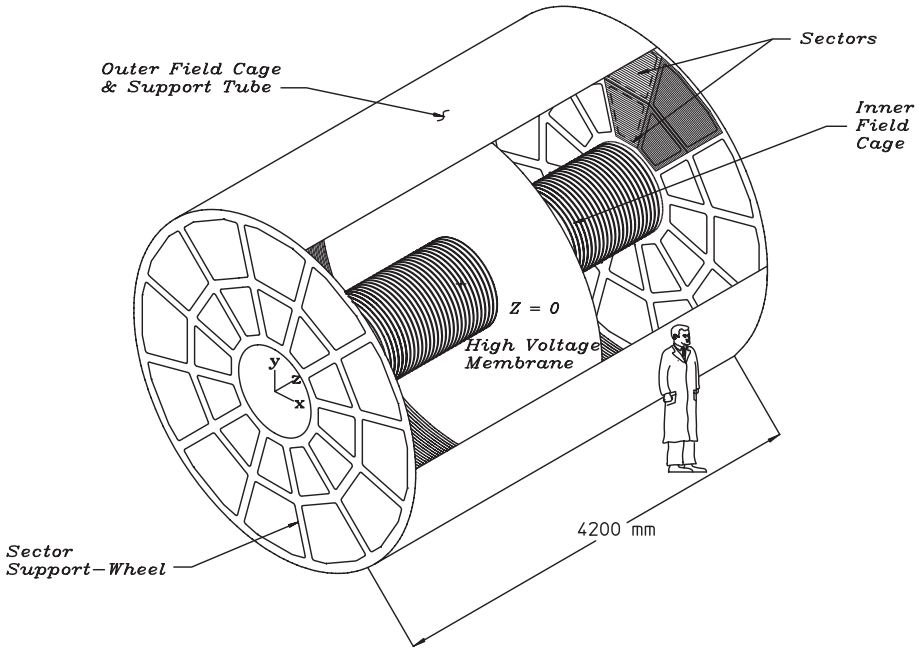

Figure 3.3: Schematics of the Time Projection Chamber (TPC).

STAR uses the Time Projection Chamber (TPC) as its primary tracking detector. It is 4.2 meters long and 4.0 meters in diameter. The TPC records the tracks of particles, measures their momenta above 100MeV/c, and identifies charged particles

(eg. pions, kaons and protons) by measuring the ionized energy loss (dE/dx). It covers ± 1.8 units of pseudo-rapidity with full azimuthal coverage. The tracking efficiency drops at high pseudo-rapidity, so usually the coverage of the TPC is limited to $|\eta| < 1.0$. The 0.5T magnetic field is provided the solenoid magnet and the uniform electric field of about 135V/cm by defined by a conductive Central Membrane (CM) at the center of the TPC. The TPC is filled with P10 gas (10% methane, 90% argon) which provides the ionizing environment. The paths of primary particles passing through the TPC are reconstructed from the released secondary electrons which drifts to the readout end caps at the end of the chamber. The readout system is based on Multi-Wire Proportional Chambers (MWPC) with readout pads [77]. The induced charge from an avalanche is shared with several adjacent pads. The TPC tracks are reconstructed by the hits and their x, y coordinates are recored in the readout pads. The z positions are determined by the time of the secondary electrons from the points of the original to anodes on the endcap and the average drift velocity. The drift velocity is measured every several hours independently using artificial tracks created by laser beams during collisions. The magnetic and electric fields are parallel and nearly uniform in r and z directions. The TPC is designed to work in high multiplicity heavy ion collisions. The TPC has a stable performance in terms of momentum resolution and energy loss measurements during RHIC running.

3.3 Correlation analysis related EM calorimeters

3.3.1 Barrel Electro-Magnetic Calorimeter

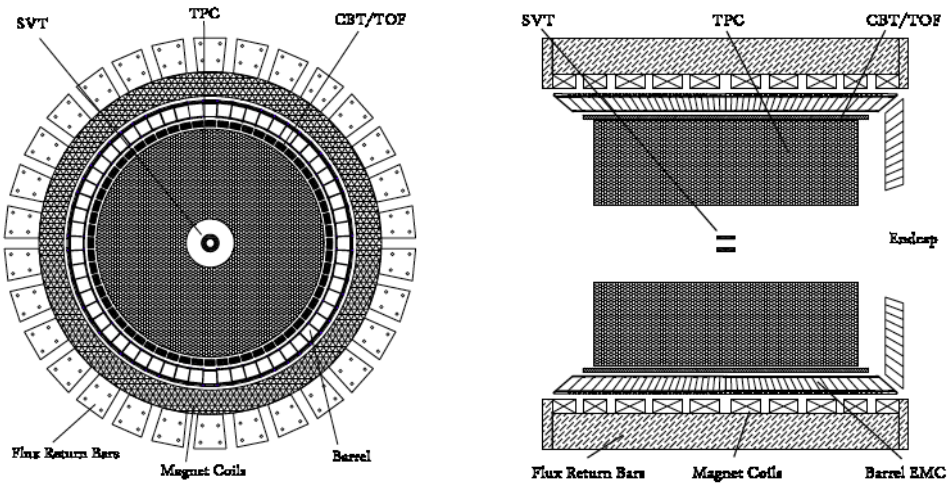

Figure 3.4: The front and side view of the Barrel Electro-Magnetic Calorimeter (BEMC). The BEMC spans $|\eta| < 1.0$, and the SVT detector shown in the plots has been moved out for RHIC Run08.

The Barrel Electro-Magnetic Calorimeter (BEMC) is triggered to provide large acceptance for photons, electrons, π^0 and η mesons, on the other hand, it is designed

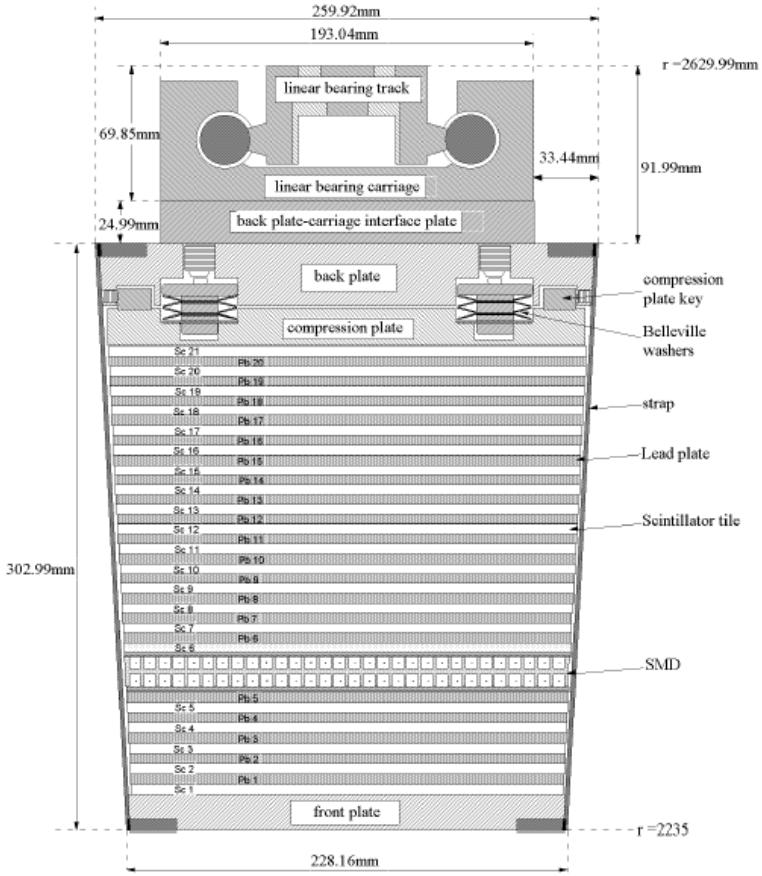

Figure 3.5: Schematics of BEMC module construction in side view. The scintillating plate alternative with the lead absorber layers. The shower maximum detecot (SMD) is at a depth about 5.6 X_0 from the front face.

to study rare process (eg. jets, heavy quarks like charm and beauty). The BEMC is a sampling detector made of lead and plastic scintillator to detect electromagnetic energy in STAR. It spans pseudo-rapidity $|\eta| < 1$ with full azimuthal coverage which matches the TPC tracking. It located outside the solenoid magnet and is at a radius of about 2.2 meters from and parallel to the beam pipe (See Figure 3.4). The BEMC consists of 120 modules, each subtending $\Delta\phi = 6^\circ$ and $\Delta\eta = 1.0$. The modules are segmented into 40 towers with each tower subtending $\Delta\phi = 0.05$ and $\Delta\eta = 0.05$. From the side view of one BEMC module (see Figure3.5), each module has a lead-scintillator stack and shower maximum detectors situated approximately 5.6 radiation lengths from the front of the stack. There are 20 layers of 5 mm thick lead,19 layers of 5 mm thick scintillator and 2 layers of 6 mm thick scintillator [78]. The thicker scintillator layers are used for the preshower detectors which will be described later. The scintillator layers alternative with the lead absorber plates. It has about twenty radiation lengths (20 X_0) at $\eta = 0$.

The plastic scintillator sheets of the modules are machined into isolated 'tiles'

(related with BEMC towers) in each layer. The signal from each scintillating tile is transported though a wavelength shifting (WLS) fiber embedded in a 'σ-groove' that is machined in the tile. Then the signal exits the WLS fiber and go into fibers of the multi-fiber optical cables through the multi-fiber optical connector at the back-plate of the module. The multi-fiber optical cables connected the optical connectors and photomultiplier tubes (PMT) inside detector boxes mounted on the out surface the solenoid magnet. The energy resolution for this calorimeter is estimated to be about $14\%/\sqrt{E} \pm 1.5\%$ (GeV).

The shower maximum detector (SMD) is designed to provide spatial resolution when a calorimeter which has segmentation (towers) significantly larger than an electromagnetic shower size. The SMD of the BEMC is essential for π^0 reconstruction, direct γ identification, and electron identification. It provides shower position and shape. It is a wire proportional counter - strip readout detector using gas amplification. It has two independent planes (marked as η plane and ϕ plane) which are separated by an aluminum extrusion and orthogonal to each other. Each plane has totally 18000 strips. Each tower is correlated with 15 η strips (η plane) and 15 ϕ strips (ϕ plane). The SMD of the BEMC has an energy resolution approximately $86\%/\sqrt{(E)} \pm 12\%$ (GeV) in η plane (while the ϕ plane is $3-4\%$ worse), the position resolution in η plane is $5.8/\sqrt{(E)} \pm 3.2$ (mm) and $5.6/\sqrt{(E)} \pm 2.4$ (mm) in ϕ plane. The preshower detectors made of the first two layers of scintillator provide π^0/γ and *electron/hadron* discriminations. The postshower detectors installed at the end of the stack together with other detectors inside the BEMC help implement the calibrations of the whole tower.The readout from the preshower detectors together with 19 other scintillator layers provides the total tower energy signal. After the BEMC official calibration and quality assurance (QA) check, the tower calibration was found not reliable at the outmost edges of the BEMC. There is a acceptance cut which is $|\eta| < 0.9$ to increase the data quality.

3.3.2 Endcap Electro-Magnetic Calorimeter

The Endcap Electro-Magnetic Calorimeter (EEMC) of STAR provides electromagnetic calorimetry in the pseudo-rapidity region $1.086 < \eta < 2.0$ and full azimuthal coverage $0 < \phi < 2\pi$. One of the primary goals of the EEMC is to determine the helicity preference for gluons ($\Delta G(x_g)$) inside a polarized proton, as a function of the momentum fraction x_g of the proton carried by gluons. The EEMC adds crucial coverage for asymmetric partonic collisions, which is the final-state quarks are boosted forward in the collider frame with momentum fractions $x_q > 0.2$ in proton, to probe gluons with $x_g < 0.1$ in other proton. The EEMC is a lead/plastic scintillating sampling calorimeter. The EEMC consists of 23 layers of radiator embedded with 24 layers of scintillators. The scintillators are stacked on top of each other and alternated by the lead radiators. The calorimeter is physically divided into two halves, with each half offset from x-axis by 15 degrees. It has 12 sectors, each sector contain 5 sub-sectors and each sub-sector has 12 towers (see Figure 3.6). The towers are the same size in ϕ, but they vary in η with the largest towers at small η and the

smallest towers at large η. In total, the EEMC has 720 towers. When we refer to the "tower", we mean the entire section of lead and scintillator, including preshower and postshower layers [79]. Each tower has a depth of 21.4 radiation length (X_0, corresponding to one interaction length for a hadron). This means the electromagnetic shower is fully contained in the calorimeter (the maximum electromagnetic shower length is 5.6 X_0). The energy resolution is $(\frac{\sigma_E}{E}) \leq (\frac{16\%}{\sqrt{E}}) + (2\%)$ and the timing response is less than one RHIC beam period (110 ns).

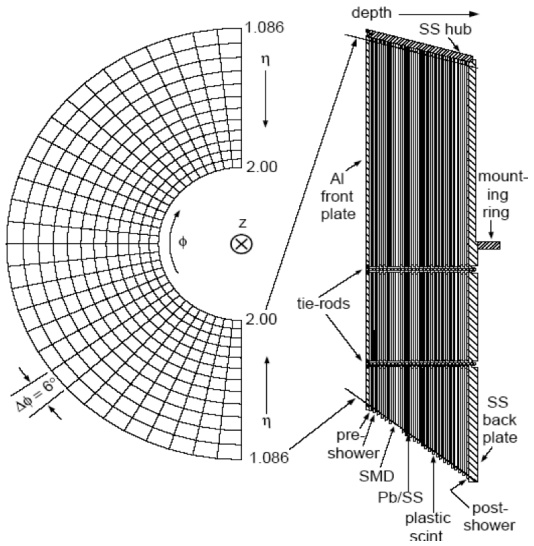

Figure 3.6: Left: The front view and side of EEMC. EEMC has 720 towers, this is one half of the EEMC. Each tower spans $\Delta\phi = 0.1$, $\Delta\eta = 0.057 - 0.099$. Right: The side view of EEMC, Preshower1, Preshower2, Shower Maximum Detector (SMD) and Postshower detectors are indicated in the figure.

The tower segmentation uses megatile construction. In the EEMC, megatiles span either 6° or 12° in azimuthal angle (ϕ). Wavelength-shifting (WLS) optical fibers run through channels in a white plastic fiber-routing layer (FRL) of each magatile. The WLS fibers are connected to photomultiplier tubes (PMT) for towers in that sector. The PMT with optical mixer is used to produce a signal which is proportional to the total deposited energy in the tower. The PMT's are powered by Cockroft-Walton bases which generate a specially tapered high voltage distribution for the dynodes.

The shower maximum detector (SMD) of the EEMC is used to provide fine spacial resolution in a calorimeter, especially to provide π^0/γ discriminations. The SMD promises better performance in both transverse shower profile delineation and energy deposition resolution. The SMD is placed about 5 radiation lengths within the EEMC. The SMD in EEMC made of triangular scintillator strips, is organized into orthogonal u and v planes (shown in Figure 3.7). Light from the SMD is carried by WLS fibers that run along the length of each strip. These fibers transport the light to 16-anode PMTs (Hamamatsu R5900-M16). Twelve multi-anode photo-

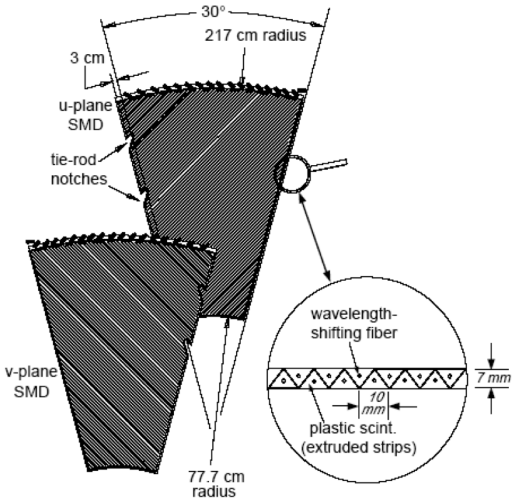

Figure 3.7: One 30° sector Shower Maximum Detector (SMD) of the EEMC. The SMD contains orthogonal u and v planes.

multiplier tubes (MAPMT), along with their Cockroft-Walton bases and front-end electronics, service the strips in each SMD sector. The first two layers of scintillator tiles, and the last layer as well, are read out by two independent WLS fibers. The high voltage on the EEMC is set such that the response of the calorimeter is uniform in transverse energy ($E_T = Esin(\theta)$, θ is the polar angle of from the primary vertex in the collision event to the tower center). The ideal gain is defined as 60 GeV E_T = 4095 ADC, the gain factor varies with pseudo-rapidity η. EEMC use minimum ionizing particles (MIPs) which are charged particles don't shower or don't deposit significant energy to calibrate towers. After the online data acquisition, official calibration procedure, a quality assurance (QA) is performed to mask out the dead or possibly bad towers before data analysis. This will be discussed further in chapter 4 and chapter 5. The EEMC is used to reconstruct π^0 and jet-like clusters in the correlation analysis which will be introduced in chapter 4.

3.3.3 Forward Meson Spectrometer

The Forward Meson Spectrometer (FMS) is a lead-glass electromagnetic calorimeter which located at the west side of STAR interaction region (IR). It faces deuteron beam during run08 d+Au interactions. The FMS is 2 meter by 2 meter matrix at a distance of 7.3 meters from the IR. It covers the forward pseudo-rapidity $2.5 < \eta < 4.0$ with full azimuthal coverage, see Figure 3.8. The FMS extends the STAR electromagnetic capability especially in the forward pseudo-rapidity region. In conjunction with the BEMC ($|\eta| < 1.0$) and the EEMC ($1.083 < \eta < 2.0$), the addition of the FMS realized a nearly hermetic in wide $-1.0 < \eta < 4.0$ electromagnetic calorimetry at STAR. The FMS allows the correlation measurements between forward mesons and photons from the full STAR detector, including the

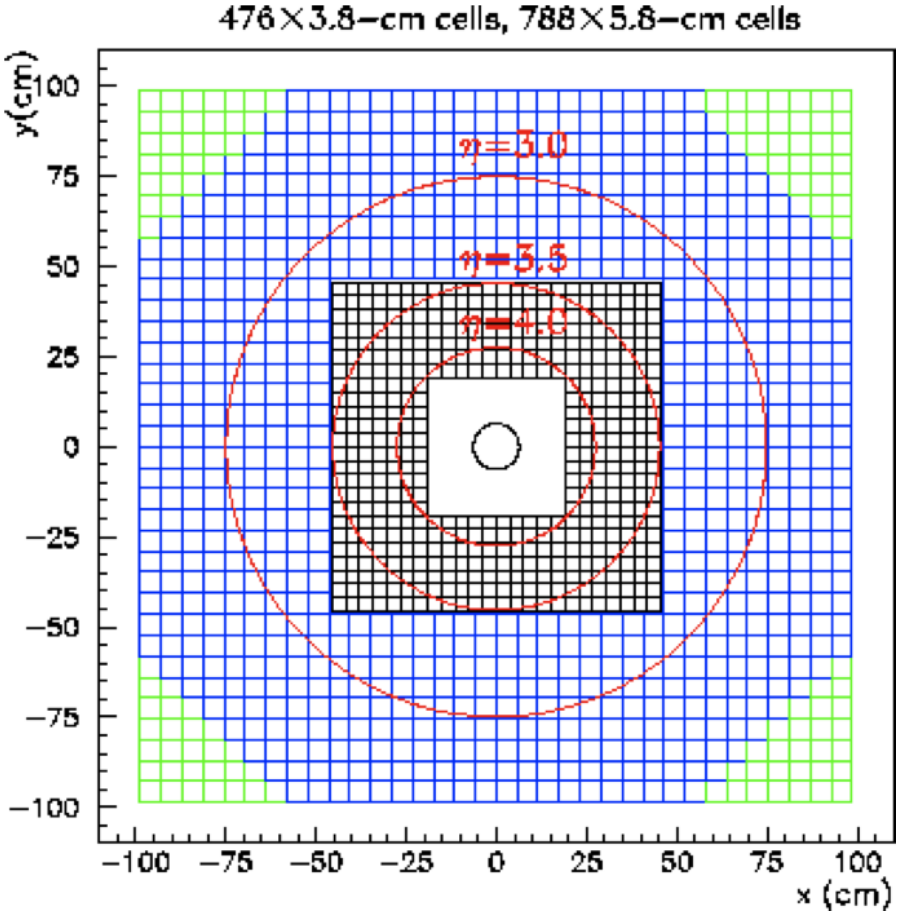

Figure 3.8: Schematics of the Forward Meson Spectrometer (FMS) seen from the interaction point. The FMS contains 476 $(3.8cm)^2$ × 45cm lead glasses and 788 $(5.8cm)^2$ × 60.2cm lead glasses. It covers $2.5 < \eta < 4.0$ with full azimuthal range.

barrel and endcap electromagnetic calorimeters (BEMC, EEMC) and the forward and midrapidity time projection chambers (FTPC, TPC). This provides the capability to probe the gluon distribution function in the gold nuclei down to $x \sim 0.001$.

The physical objects of the FMS are described the following [24],

- A measurement of the gluon distribution distributions, $x_{BJ}g(x_{BJ})$, in gold nuclei for $0.001 < x_{BJ} < 0.1$, thereby extending our current knowledge and including an overlap region that tests the universality of the gluon distribution.
- Characterization of correlated pion cross sections as a function of Q^2 (p_T^2) and η to search for the onset of gluon saturation effects associated with macroscopic gluon fields.
- Measurements with transversely polarized protons that are expected to resolve the origin of the large transverse spin asymmetries in $p_\uparrow + p \to \pi^0 + X$ reactions for forward π^0 production.

3.3. Correlation analysis related EM calorimeters

The FMS can be divided into two detachable halves, North and South. Each of them contains two parts, the inner part ($3.0 < \eta < 4.0$) which consists of small size glasses and outer part ($2.5 < \eta < 3.4$) which consists of large size glasses. There are 476 3.8 cm ×3.8 cm × 45 cm lead glass inner cells with 18 radiation lengths and 788 5.8 cm × 5.8 cm × 60.2cm lead glass outer cells with 18.75 radiation lengths, see Figure 3.8. Each individual lead glass is marked as "cell". They constitute the 2 meters by 2 meters square matrix with corners cut (7×7 cells triangle). The lead glasses collect the Cherenkov light from the electromagnetic shower generated by the particles passing through the calorimeter and interacting with the lead inside the glass. The lead glasses are optically glued to photomultiplier tubes (PMT) that collect and amplify the signal. The PMTs are powered by certain high voltage (HV) systems. The inner cells from the Institute for High Energy Physics (IHEP) connected to FEU84 PMTs are powered by Cockroft Walton bases. A second set of inner cells which are provided by Thomas Jefferson National Accelerator Facility (TJNAF) uses XP2972 PMTs. The outer cells from Fermi National Accelerator Laboratory (FNAL) are coupled with XP2202 PMTs and powered by Zener-diode voltage divider. Each detector unit underwent a series characterization checks before installed in the FMS stacks. The lead glassed are cleaned and wrapped in a thin (0.1mm) foil of reflective aluminized PolyEthylene Terephthalate (Al/PET) in order to contain as much as possible the light from the shower contained in the cell and to get rid of the external and cell-by-cell light contamination. Detector response and positioning checks were completed for each individual cell using a light-emitting diode (LED). In addition, a prototype LED light-flasher board covering a whole FMS quadrant was used to test cell by cell in order to check the presence of dead channels and possible mapping errors. The board was also used in run08 to monitor cell status during collision by allowing LED pulse triggered events to enter the data stream. Such LED events can be clearly clarified from other collision hits and can be removed from the reconstruction algorithm afterwards. The 1264 channels of the FMS readout system is provided by so called QT boards at 9.38MHz. The signals are first collected by 8 channel QT daughterboard cards and then merged into the larger QT32 boards. Each 32 channel QT motherboard records ADC signals and TDC discriminator information from 32 individual cells. The ADC signals are sent to a Field-Programmable Gate Array (FPGA) which compresses the inputs and perform a first trigger selection. Then the signals are passed to the Data Storage and Manipulation (DSM) boards, where more refined trigger algorithms are performed.

The calibration of the FMS is performed in two steps. First, the cell by cell calibration is determined by using the mass distribution of the reconstructed π^0 and this method is called online calibration. Every reconstructed photon cluster pair (π^0 candidate) has the highest energy deposition which is related with one lead glass. For this lead glass, an invariant mass spectrum is generated with multiple events and then fitted with a Gaussian function. The gain of this lead glass PMT is tuned to get the centroid to the nominal π^0 mass ($0.135 GeV/c^2$). After all of the cells are calibrated, the procedure is iterated until reasonable convergence is reached. The online calibration is realized by applying effective gains and modifying the high volt-

age related with a certain PMT, and this is done before the rest part of a run. The second step is called offline calibration. As the peak value of the reconstructed π^0 invariant mass spectrum is dependent on the energy of the reconstructed π^0 energy, the peak position shift to higher value as the energy increases. Dedicated Monte Carlo simulations of full Cherenkov light have shown that the energy dependence may be caused by deeper longitudinal shower profile, transverse leakage at the edges of cells and the ADC granularity. So an overall energy dependent correction is applied to all clusters and this works well for the range $10GeV < E < 65GeV$. The response of the FMS also has run dependence due to different luminosity of collisions. The run dependence is corrected using the LED tagged table before data analysis. Generally, the FMS is proved to be relatively stable for run08 production data. The π^0 mass resolution is expected to around $\sigma_m \sim 23MeV/c^2$.

The FMS has fast readout which give good sampled luminosity for forward particles while the Minimum Bias trigger will collect small fraction in this forward region. In RHIC run08, the FMS with high tower trigger selects triggered forward π^0s for the correlation studies in collision events. Simulation studies predict an energy resolution about $15\%/\sqrt{(E)}$ (GeV) and a position resolution for π^0s better than 0.5 cm.

3.4 Other trigger detectors

3.4.1 Beam Beam Connter

The Beam Beam Counter (BBC) consists of two hexagonal scintillator modules which covers pseudo-rapidity range $3.4 < |\eta| < 5.0|$ with full azimuthal coverage $\Delta\phi = 2\pi$. Each module situated at a distance of 3.7 meters from the interaction region (IR) and mounted around the beam pipe [80]. The modules contain two different types of scintillator and generally can be divided into two rings. The inner ring with 18 tiles covers $3.9 < \eta < 5.0$ and outer ring with 18 tiles covers $3.4 < \eta < 3.9$, the structure of the BBC is shown in Figure 3.9. A coincident signal from any of the 18 tiles on the east side and any of the 18 tiles on the west side of the IR constitutes a BBC coincidence. The coincidence of BBC is a Minimum Bias (MB) trigger during p+p collisions to monitor the collision luminosity. The charge particles multiplicity recorded by the BBC event by event is a measure of centrality in the run08 d+Au interactions. As the electro-magnetic calorimeters at STAR are fast detectors, a fast detector is required to measure the primary vertex in a collision event. The BBC has comparable readout frequency as the fast EM calorimeters, in the data analysis the differences between the time of flight from IR measured in the BBC counters are used to calculated the longitudinal position of primary collision vertex in each event. The transverse spread of the primary vertex is small (of order mm), and can be ignored compared to the large transverse position of the reconstructed particle in the EM calorimeters. During RHIC run08, only the two inner rings of the BBC are active, but this does not impact the position resolution of the measured primary vertex.

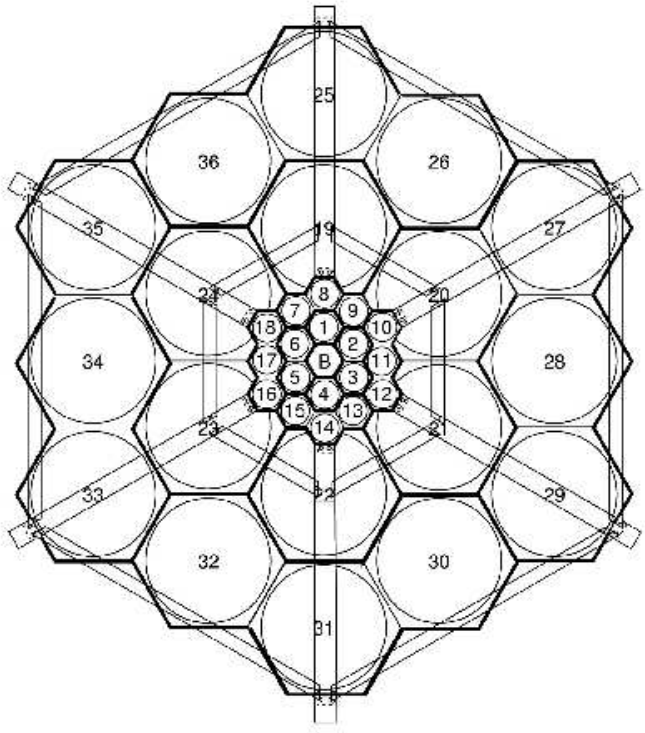

Figure 3.9: The schematics of Beam Beam Counter (BBC) from the beam view.

3.4.2 Zero Degree Calorimeter

The Zero Degree Calorimeter (ZDC) is located downstream of the DX dipole magnet of RHIC (locates west and east side from the interaction region) and it is designed to detected the neutral beam fragments especially neutrons in high energy collisions of nuclei (not deflected by the bending magnets, and contain small scattering angle). It sits between the DX magnet and the D0 magnet, therefore there is zero magnetic field around the ZDC. The ZDC is a event trigger detector and luminosity monitor. The energy is calibrated by the clear single neutron peak in peripheral nuclear collisions. The energy resolution is $\frac{\sigma_E}{E} \leq 20\%$ at $E_n = 100GeV$. The ZDC consists of three models and each one is a sampling hadronic calorimeter made of tungsten plates and fiber ribbon stacks. As the optical fibers only transport Cherenkov light emitted nearly aligned with the fiber axis, this detector is most sensitive to particles cross at approximately 45° to the fiber axis. The lower energy shower is therefore suppressed. The fibers are glued to the tungsten plates with threaded mounting holes. The fiber ribbons were wound on a mandrill and then impregnated with a low viscosity white silicone rubber glue. The glue covers the active region of the fibers (200 mm) and protects the fiber surface in the region of the fiber/absorber sandwich [81]. 12-stage PMT (Hamamatsu R329-2) are connected to the fiber bundles (see Figure 3.10). The ZDC coincidence of two beam directions is a minimal bias selection of heavy ion collisions. In polarized p+p collisions, it helps measure the beam polarization

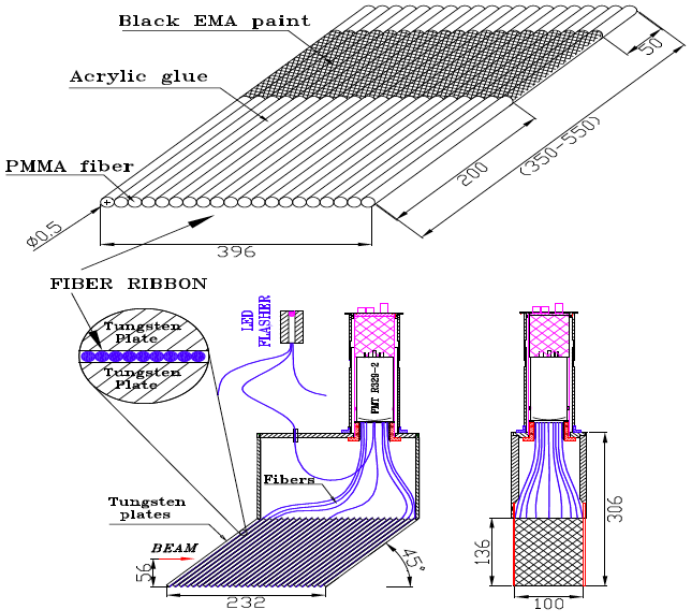

Figure 3.10: Zero Degree Calorimeter (ZDC) construction. The schematics of internal structure of the ZDC.

as a local polarimetry. In the data analysis, we use the spectator neutron measured in the deuteron facing (west) ZDC to approach p+Au collisions, and study the correlation under such conditions.

Chapter 4

Data analysis

4.1 Data stream and triggers

4.1.1 RHIC data stream and STAR Data Acquisition

The RHIC is operated fill by fill and a "fill" is defined as a completed machine cycle time period including the injection, acceleration and storage of colliding beams [82]. The time of one successful fill from beam injection to beam dump can last several hours. A unique fill number is used in identifying and collecting data. Due to the large amount of data, the collision data taking during one fill are divided into several runs and a unique run number stands for a certain time period in one fill. The RHIC beams are divided in term of bunches, the bunch period is 110 ns in 120 bunches (including 10 bunch abort gap) mode.

The RHIC Computing Facility (RCF) allocates large data storage room so that STAR detectors can transfer the online raw data to High Performance Storage System (HPSS) storage system with a steady rate up to 30MB/s [83]. The STAR detectors can be divided into fast detectors and slow detectors according to their data readout rates. For example, due to the limitation of its drift velocity, the rate of TPC recorded events is about 1000Hz. The TPC, FTPC, SMD of the BEMC are slow detectors at STAR. As the BEMC, EEMC, FMS, ZDC and BBC have comparable event rate as the RHIC beam crossing rate ($\sim$ 9.38MHz). The rate of data from STAR detectors during collisions is up to 8000 MB/s. The STAR Data Acquisition (DAQ) system reads the data from detectors and reduce the rate to 30 MB/s, afterwards it stores the data in the HPSS facility.

The interactions are selected based on the distributions of particles and energy obtained from triggered detectors. The digitized signals are examined at the STAR trigger system which is pipelined system. Events that pass the selection criteria of a certain trigger are sent to storage at a rate of about 5Hz ($\sim$ 50 MB/s) [84]. There are four different trigger levels online, Level 0, 1, 2 and 3. The first three trigger levels are based on raw data analyzed within different time budget, while the last trigger makes the final decision based on the tracking in the slow detectors. The data during one RHIC clock tick are recorded in the Data Storage and Manipulation (DSM). After a simple calculation, the data is transferred to Trigger Control Unit (TCU). The TCU boards look at the results and issue trigger commands whether to restore the data to Trigger Clock Distribution (TCD) boards which are the interface between the triggers and detectors. If the events satisfy the trigger conditions, the data from detectors start digitization. The time of digitization is very short, for example, the Level 0 trigger takes less than 1.5 μs to issue a decision after the

interaction. After a store trigger is send to detectors, the time for data digitization around several milliseconds allows more detailed analyses of the trigger data to determine whether the event satisfy more finely grained criteria. For one collision event, the Level 1 trigger works in a time period of about 100 μs and Level 2 with a time budget of about 5 ms.

4.1.2 Trigger types

At STAR, different triggers are performed for different detectors. Some triggers are applied to monitor the status of interactions and some triggers are related with the response of specific detectors. The trigger detectors at STAR are fast detectors, for example, BBC, ZDC, BEMC, EEMC and FMS. The triggers correlated with event selection in the correlation data analysis are introduced in the following.

(1) Minimum Bias Trigger (MB):

Minimum Bias (MB) Trigger is the basic trigger to judge whether a collision happens or not. In Au+Au interactions, ZDC detectors are used as the MB trigger detectors. A coincidence between west ZDC and east ZDC is required for MB trigger, meaning both detectors detect at least one neutron. In addition, the time differences of such signal between west/east ZDC is within the correct time window (the interaction is not far from the center of the TPC). In d+Au interactions, the east ZDC facing Au beam is required to have at least one neutron detected. This leaves room for background events like single beam remnant to be marked as collisions events. Although the high multiplicity in Au+Au or d+Au collisions may lead to ADC saturation in the BBC detectors, the BBC can precisely measure the charged particle multiplicity. The MB trigger detectors change to the BBC detectors in p+p collisions. A coincidence of west and east BBC are required when both detectors have signals above a certain threshold in a constrained time window. The design of the interaction point is different form the real or physics interaction point (IP) for collider experiment. The real IP is the primary vertex of the particle collision, and it varies event by event. The time difference between BBC west and east modules are used to calculate z position of the primary vertex. This technique is applied both in p+p events and d+Au events to determine the primary vertex for the FMS-BEMC, FMS-EEMC and FMS-FMS correlation analysis. As the TPC which usually provide primary vertex information for charged particles is the slowest detector at STAR, the detectors used in the correlation analysis are not synchronous with the TPC:

(2) FMS High Tower Trigger (HT):

The MB triggers are not optimized to select forward particle productions. The π^0's in the FMS play an important role in the correlation analysis, and a trigger that requires one FMS cell ADC value above a certain threshold (High Tower) is developed during RHIC run08 p+p and d+Au collisions to pursue forward particle triggered events. The gains of the FMS PMTs vary cell by cell, and the energy threshold for the high tower trigger is computed with gain and correct factors in offline reconstruction. The threshold for inner cells and outer cells in the FMS are different, and generally inner cells have 400 ADC counts threshold and outer cells

have 200 ADC counts threshold during online operations. For the FMS triggered events, the Minimum Bias conditions are not claimed due to the high threshold in the FMS which has already suppressed the non-collision events or background fluctuations. The FMS triggered events can be further divided into two types depending on the condition of the TPC,

(I) FMS slow trigger events: Events including information from all the sub-detectors at STAR during collision operations. The rates of such events are restricted by the response of the TPC. Slow is marked on these events due to the low rates. Previous FMS π^0 + TPC charged particle azimuthal correlations are studied with these events [12].

(II) FMS fast trigger events: When the TPC are digitizing its data, other fast detectors are ready for new trigger commands. The FMS fast trigger events are under the same FMS trigger conditions as in the FMS slow trigger events but with no requirement on the slow detectors (eg. TPC). These events are not affected by the slow detectors, so the readout rates are much higher than the FMS slow trigger events. The data from fast detectors like FMS, BEMC, EEMC are stored in a different data stream before the DAQ system rates get reduced. The FMS-EEMC correlation analysis are studied using the FMS fast trigger events.

As run8 is the first run of the FMS at STAR, there are some tests for the FMS commissioning at the beginning of this run. Then in d+Au collisions, the data from north part of the FMS is found recorded later than the DAQ data writes due to longer cable connected to the north part than the south part of the FMS. The correlation between FMS and BEMC, TPC and EEMC requires the information from the FMS should be triggered crossing the DAQ data writing. Therefore, only the south part of the FMS is used for the FMS-EEMC correlations in d+Au collisions. But the FMS L2 trigger includes the data from the RHIC tick 107 ns before the trigger (pre-crossing) and the data from the RHIC tick 107 ns after the trigger (post-crossing). The FMS-FMS correlations contain full azimuthal coverage of the FMS detector. This problem gets resolved in p+p collisions. This does not affect the azimuthal correlations between a triggered particle measured in the FMS and an associated particle in the EEMC, which will be discussed later, as the correlations between two independent detector do not require full azimuthal coverage.

4.1.3 Data set

In our data analysis, we use the RHIC run08 p+p collision and d+Au collision data recorded at STAR. The center of mass energy for both p+p and d+Au interaction is 200GeV. In high energy experiments, luminosity $\mathcal{L}$ is a characteristic scale to describe the interaction cross section, which is the number of interacting particles per unit area per unit time. Assuming the beam profile follows a Gaussian function, the instantaneous luminosity can be written as [85],

$$\mathcal{L} = \frac{f_{rev} K}{2\pi\sigma_x\sigma_y}, \tag{4.1}$$

where σ_x and σ_y are the transverse widths of the beam overlap region, f_{rev} is the revolution frequency, K is bunch intensities of the two beams summed over all bunches. The average store luminosity in RHIC run8 for d+Au collision is $14 \times 10^{28} cm^{-2} s^{-1}$ and the average store luminosity in transverse polarized p+p collision is $40 \times 10^{30} cm^{-2} s^{-1}$. Due to the inefficiency of detector response, STAR does not see all of the store luminosity. The BBC introduced in chapter 2 plays an important role in measuring the integrated luminosity at STAR. The cross section measured with BBC is determined from VanderMeer scan [86],

$$\sigma_{BBC} = \frac{R_{BBC}}{\mathcal{L}_{vaneer}}, \tag{4.2}$$

where R_{BBC} is the collision rate detected in the BBC, $\mathcal{L}_{vaneer}$ is the luminosity determined in the VanderMeer scan run and σ_{BBC} is the BBC cross section. The BBC cross section σ_{BBC} is about 26mb from VanderMeer scan operation for p+p collisions. Then the effective integrated luminosity at STAR $\mathcal{L}_{STAR}$ is,

$$\mathcal{L}_{STAR} = \frac{N_{BBC}}{\sigma_{BBC}}, \tag{4.3}$$

where N_{BBC} is the total number of events recorded in the BBC. The BBC cross section σ_{BBC} is independent of the collision time, but the luminosity does rely on time. The luminosity per run can be measured according to the following equation,

$$\mathcal{L} = \frac{dN}{\sigma_{BBC} dt}, \tag{4.4}$$

$$\mathcal{L}_{integral} = \frac{N}{\sigma}, \tag{4.5}$$

where $\mathcal{L}$ is the store luminosity, $\mathcal{L}_{integral}$ is the integrated luminosity, N is the number of particles involving in interaction and σ is the interaction cross section. With the FMS high tower trigger, the integrated luminosity of d+Au run is $49 nb^{-1}$ and the integrated luminosity of p+p run is $7.6 pb^{-1}$ at 100 GeV/nucleon beam energy during run8.

In perturbative QCD, the p+p collision di-hadron correlations are described as a $2 \rightarrow 2$ parton scattering in parton level. With high gluon density inside the Au nuclei, more gluons may interact with the scattering partons before or after the $2 \rightarrow 2$ parton scattering. As it is hard to disentangle the medium interactions in Au+Au collisions, the correlation studies in d+Au collisions provide a good path to isolate cold nuclei effect. The correlation analysis require coincident hadrons measured in both the FMS and the EEMC. In addition to the response of the FMS in FMS triggered events, the EEMC should be active with information about deposited energy of passing through particles. The unit of deposited energy is hit in the FMS and the EEMC.

There are 340 p+p collision runs and 224 d+Au collision runs with the FMS high tower trigger. These runs contain both the FMS and the EEMC hit records. The collision events in the data stream for p+p production is about 270M events and the number of d+Au events is about 117M.

4.2 Monte Carlo data

In experiment, what happens during collision is described through reconstruction methods and data analysis. With proper physics models, the whole process of high energy interactions can be simulated with Monte Carlo methods which are based on computational algorithms that rely on repeated random sampling to compute results. The Monte Carlo methods contain giant statistics of sampling events which obey a deterministic algorithm. Usually such calculations are performed on computers. The implementation process is as the following,

- Define a domain of inputs and specific parameters.
- Generate inputs randomly from a probability distribution over the domain.
- Perform a deterministic computation on the inputs.
- Accumulate results over a certain amount.

The Monte Carlo simulation can contain multiple freedom of degrees, It is a powerful tool to solve the many body problems in quantum systems. In the data analysis mentioned in this thesis, the event generators PYTHIA, HIJING and the detector simulator GEANT have been used to compare with experimental data. The event generators generally factorize the full high energy scattering process into individual sub-processes, and include a series of modifications for the tree-level pQCD diagrams such as photon and gluon bremsstrahlung or higher order corrections. The generated simulation samples are in the same form as real data.

PYTHIA is a leading order high energy hadronic interaction event generator [87]. It contains theory and model predictions for hard parton scattering, initial- and final-state parton showers, fragmentation functions and particle decay pattens. Parameters are tuned by experimental results and varied in different version. For the correlations studies in this thesis, the relevant region is forward pseudo-rapidity. The version of PYTHIA is selected to be 6.222 for p+p collisions at $\sqrt{s} = 200GeV$, due to good agreement between data and simulation in the forward region. The events in data are triggered by forward rapidity π^0's, and a specific filter which only records events with forward π^0 ($2.5 < \eta < 4.0$) carrying $p_t > 1GeV/c$ is applied on the p+p simulation to reduce CPU time.

Heavy Ion Jet Interaction Generator (HIJING) was developed by M. Gyulassy and X.-N. Wang to simulate p+p, p+A and A+A reactions [88]. HIJING contains parameters related with hard QCD interactions and soft string dynamics. In particular, HIJING reproduces many inclusive particle spectrum and two particle correlation results observed in experiment. We use HIJING 1.38 with the same filter set up in PYTHIA to study the FMS π^0 - EEMC π^0 or jet-like clusters azimuthal correlations in d+Au collisions at $\sqrt{s} = 200GeV$.

The event generator only provide information about final particles, while the identifications of particles rely on detector performance in high energy experiments. GEANT is a system of detector description and simulation tools which includes the

detector response to interpret the experimental data [89]. It simulates the passage of high energy elementary particles through the matter. In GEANT program, the detector response be studied by transport of particles through experimental setup, the setup and the particle trajectories can visually seen in graphics. In STAR group, a specific detector simulator based on GEANT3 including the material and response parameters for STAR detectors is named GSTAR. The simulation samples in both p+p collisions and d+Au collision for the analysis of this thesis use GSTAR to simulate the response of STAR detectors.

4.3 Triggered π^0 reconstruction in the FMS

4.3.1 π^0 decay kinematics

The mean life time (τ) of π^0 is 8.4×10^{-17} s [22]. The π^0 converts into photon pairs shortly after its generation with branching ratio of 98.8%. Most of the π^0's are from primary collisions and the fraction from decay contribution is small. So the reconstruction is assuming that π^0 is generated from the primary vertex of collision as its decay length is only 25.1 nm. From energy conservation and momentum conservation, the mass of photon pair is,

$$M_{\gamma\gamma} = E_{\gamma\gamma}\sqrt{1 - z_{\gamma\gamma}^2} sin(\frac{\phi_{\gamma\gamma}}{2}), \tag{4.6}$$

where $E_{\gamma\gamma}$ is the sum of photon energy in the pair, $\phi_{\gamma\gamma}$ is the angle between the momenta of the two photons. In equation 4.6,

$$z_{\gamma\gamma} = \frac{|E_1 - E_2|}{E_1 + E_2}, \tag{4.7}$$

$z_{\gamma\gamma}$ is defined as the energy sharing for the two photons. The minimum $\phi_{\gamma\gamma}$ is achieved when the decayed photons have equal energy. The FMS locates at a long distance (7.3 meters) from the interaction point of STAR. Therefore, the photons decayed from π^0 cover more area in the FMS than that in the EEMC (or BEMC) at the same $\phi_{\gamma\gamma}$. As the FMS cells (inner cell: $3.8cm \times 3.8cm$, outer cell: $5.8cm \times 5.8cm$) are much smaller than the EEMC (BEMC) towers (around $10cm \times 10cm$), the photon showers stretch along more towers in the FMS. The high granularity of the FMS provides good resolutions for π^0 measurements. π^0's detected in the FMS have higher energy than those in the EEMC (or BEMC), and the relevant $\phi_{\gamma\gamma}$ shown in Eq.(4.6) tends to small. The projection of the π^0 decayed photon separation in the FMS ($d_{\gamma\gamma}$) is small compared to the distance from primary vertex to the front surface of the FMS (Z_{FMS}), thus $\phi_{\gamma\gamma} \approx \frac{d_{\gamma\gamma}}{Z_{FMS}}$. With this approximation, equation 4.6 can be rewritten as follows,

$$M_{\gamma\gamma} \approx E_{\gamma\gamma}\sqrt{1 - z_{\gamma\gamma}^2} \frac{d_{\gamma\gamma}}{2Z_{FMS}} \tag{4.8}$$

The nominal mass of π^0 is $134.98 MeV/c^2$ [22], and the mass window is selected to be (0, 0.2) (GeV/c^2) for the π^0 reconstructions in the FMS. The key point is to

i	1	2	3
a_i	0.8	0.3	-0.1
b_i	0.8 cm	0.2 cm	7.6 cm

Table 4.1: Parameter a_i, b_i in Eq.(4.9).

find reasonable photons candidates in the FMS. The algorithm which characterizes the transverse shower shape of clusters associated with photons and the method of isolating single photon from two photon signals will be introduced in next section.

4.3.2 FMS cluster finding algorithm

The transverse electromagnetic profile is parameterized using the method mentioned in [90]. This had already been used in RHIC run3 FPD analysis [91], and inherited by the FMS reconstruction codes. The transverse electromagnetic shower energy density is characterized in a two-dimensional cumulative function,

$$F(x,y) = \frac{1}{2\pi}\sum_{i=1}^{3} a_i(arctan\frac{xy}{b_i\sqrt{b_i^2+x^2+y^2}}), \tag{4.9}$$

Energy deposited in a cell is calculated from the cumulative function (see Eq.(4.9)) at corners.

$$G(x,y) = F(x+\frac{d}{2},y+\frac{d}{2})-F(x+\frac{d}{2},y-\frac{d}{2})-F(x-\frac{d}{2},y+\frac{d}{2})+F(x-\frac{d}{2},y-\frac{d}{2}), \tag{4.10}$$

where x and y are the cell center positions, d is the cell transverse width, and the values of the parameter a_i and b_i are put in Table 4.1. Integral of G(x, y) equals to 1, which sets the condition of $a_1 + a_2 + a_3 = 1$.

The longitudinal function of the electromagnetic shower is assumed to be independent of energy. The deposited energy in tower is the integral of the overall longitudinal profile of tower, they will be mentioned in the following section. As the Moliere radius R_M which characterizes the transverse dimension of fully contained electromagnetic showers in inner cells and outer cells are similar, the FMS is taken as a homogeneous detector for the cumulative function (Equation 4.9). The estimated x, y positions and energy deposition for photon are obtained from the fit results. The low energy π^0 (E $<$ 30GeV) decayed photons have sufficiently large separation in the FMS. This leaves two distinct peak in energy distribution of the whole detector. For this case, the two photons can be distinguished by fitting them independently. As the energy of π^0 increases (E $\sim$ 50-60 GeV), the separation $d_{\gamma\gamma}$ becomes smaller and the two photons will get merged in the FMS. The fitting will not work if a clear two peak can not be found in the deposited energy spectrum. To address the problem in the second case, a moment analysis are integrated in the FMS cluster finding algorithm, which will be introduced later.

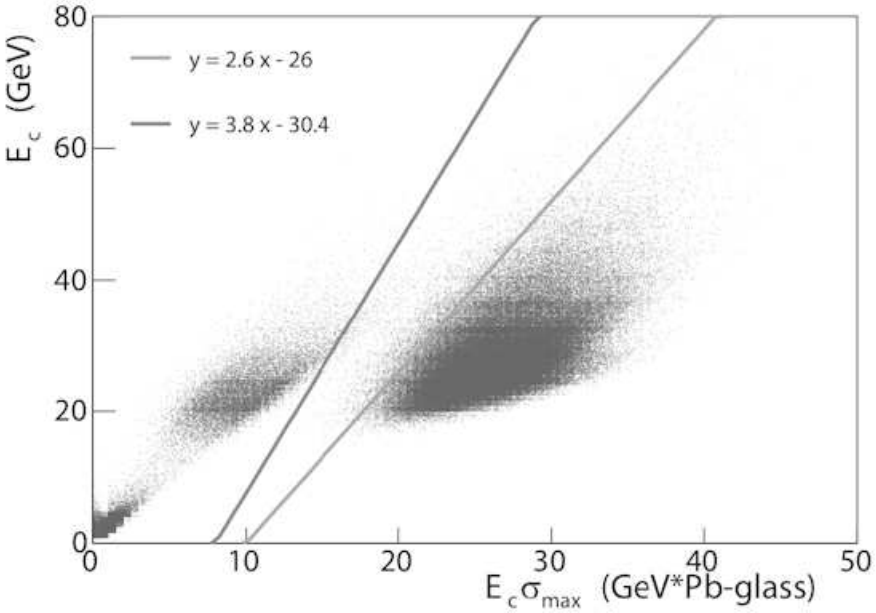

Figure 4.1: E_C VS $E_C\sigma_{max}$ of clusters in simulated single pion events. The clusters are reconstructed in the FPD++ small cells by the default cluster finding algorithm. The two lines divide the E_C-$E_C\sigma_{max}$ plane into three regions, where one-photon, double-photon or both fits are applied on clusters. Figure from [91]

The cluster in the FMS is defined as a group of non-zero energy towers, and these towers are next to each other. The cluster is formed starting from a peak energy tower and incremented by neighboring towers with lower and lower energy deposition. Generally, clusters are surrounded by zero-energy towers which make up the boundaries. When two peak towers are relatively close to each other (eg. one tower distant to each other), the towers between them look like a valley and the towers are added to cluster which has the peak tower with closest distant to the valley. Moreover, if multiple equidistant peaks happen, the valley towers are defined to belong to partial cluster with highest energy. Collections of towers with multi-peak structure are split into pieces and each of them stands for one single photon candidate. To reduce the contamination from statistical fluctuation or energy deposited by MIPs, the energy of cluster is required to be great than 2GeV. Further $z_{\gamma\gamma}$ cut will cut out low energy clusters. The energy threshold restriction does not impose additional bias in event selection.

When the hits of the two photons decayed from the same π^0 are too close to each other, the two photons are grouped in single cluster as there is no obvious valley. In this case, the one photon fit will be applied erroneously. To distinguish single photon clusters from two photon clusters, a moment analysis is performed to each cluster to characterize the transverse area of its energy deposition. Singe photon clusters most

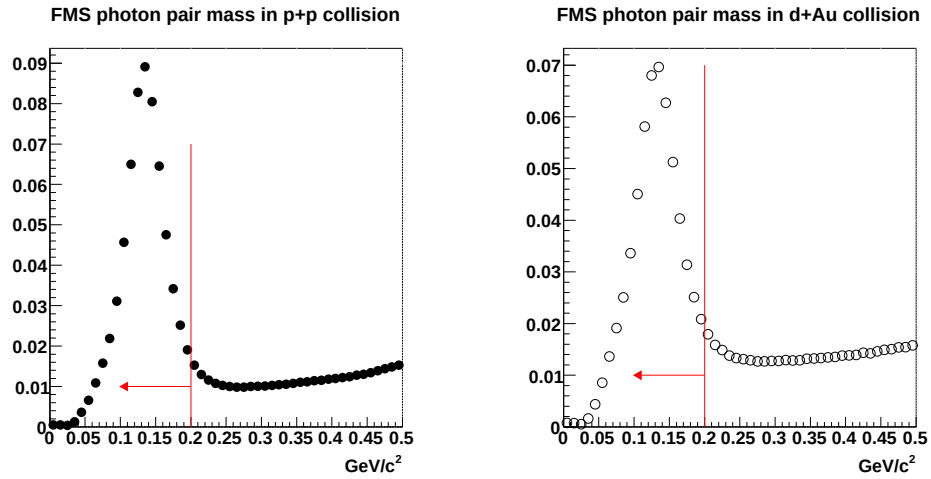

Figure 4.2: The normalized distribution of the invariant mass of the photon pair with $p_t^{FMS} > 2.0 GeV/c$ in the FMS in p+p collisions (left panel) and d+Au collisions (right panel). The π^0 candidates are selected within $mass < 0.2 GeV/c^2$ region.

likely have smaller transverse spreading size than the two photon clusters. One can characterize a clusters as a group of towers from its first three orders of moments. The deposited energy E_i of tower i is treated deposit in the center of the tower. The 0th order of moment is energy sum of cluster E_C,

$$E_C = \sum_i E_i, \tag{4.11}$$

The two 1th moments give the averaged x, y positions (i.e. the positions of center of gravity) of clusters,

$$x_0 = \frac{\sum_i E_i x_i}{\sum_i E_i} = \frac{\sum_i E_i x_i}{E_c}, \tag{4.12}$$

$$y_0 = \frac{\sum_i E_i y_i}{\sum_i E_i} = \frac{\sum_i E_i y_i}{E_c}, \tag{4.13}$$

The second order moments form a matrix. The elements listed as follows provide information about orientation and transverse size of the cluster,

$$\sigma_{xx} = \frac{\sum_i E_i (x_i - x_0)^2}{\sum_i E_i} = \frac{\sum_i E_i x_i^2}{E_c} - x_0^2, \tag{4.14}$$

$$\sigma_{yy} = \frac{\sum_i E_i (y_i - y_0)^2}{\sum_i E_i} = \frac{\sum_i E_i y_i^2}{E_c} - y_0^2, \tag{4.15}$$

$$\sigma_{xy} = \sigma_{yx} = \frac{\sum_i E_i(x_i - x_0)(y_i - y_0)}{\sum_i E_i} = \frac{\sum_i E_i x_i y_i}{E_c} - x_0 y_0. \quad (4.16)$$

Since the matrix is symmetric, one can diagonalize it and we take the larger eigenvalue σ^2_{max},

$$\sigma^2_{max} = \frac{(\sigma_{xx} + \sigma_{yy}) + \sqrt{(\sigma_{xx} - \sigma_{yy})^2 + 4\sigma^2_{xy}}}{2}. \quad (4.17)$$

The clusters containing two photon (photon 1 and photon 2) information are superposition of two single-photon cluster [91]. The resultant second order moment of such cluster is,

$$E^2\sigma^2 = E(E_1\sigma_1^2 + E_2\sigma_2^2) + \frac{E^2}{4}(1 - z^2_{\gamma\gamma})d^2_{\gamma\gamma}. \quad (4.18)$$

Comparing with Eq.(4.6), the two photon cluster $E^2\sigma^2$ is associated with the invariant mass of π^0. Figure 4.1 (from [91]) shows E_C versus $E_C\sigma_{max}$ for both single photon clusters and clusters containing two photons. Two lines divide the E_C-$E_C\sigma_{max}$ plane into three regions,

(1) Category-1: clusters with small size relative to the energy most likely contain one photon, and single photon fit is applied.

(2) Category-2: clusters with large size relative to the energy most likely contain two photon, and double-photon fit is tried.

(3) Category-0: clusters populate between Category-1 and Category-2, which are ambiguous clusters. Both single photon fit and double photon fit are tried, and the one to be chosen is based on the χ^2 of the fitting.

This category method is proved to work well and its performance in RHIC run3 FPD analysis was presented in [91]. The same method is imported from the FPD++ analysis and adapted in the FMS to reconstruct π^0. The parameters of the two lines which distinguish single photon cluster, double photon cluster and ambiguous clusters are optimized for the FMS. The reconstruction efficiency and position resolution have been studied for single pion events simulated with GEANT and for full PYTHIA+GEANT events [12]. The position resolution is half cell width and the spread of energy from simulated energy to reconstructed energy of single photon or pion is 0.79GeV.

During RHIC operation, due to bad electronic channel, not expected performance of bad PMT base or broken optical connection, there are cells not active which generate holes in the readout of the FMS matrix. A map which records the status of cells in the FMS is continuously updated to mask out the bad channels. The impacts of dead cells on the cluster finding algorithm have been studied systematically [12]. Photons hits in the dead cells are poorly reconstructed both in energy and position. However, the poor reconstruction efficiency is constrained to a small area around the dead cell. Photons hit around one cell width from the dead cell can be well reconstructed in position, especially compared with the same case without the presence of dead cell. Thus removing dead cells does not affect the reconstruction of photons with the default cluster finding algorithm.

A good photon table is organized after the offline gain correction, after removing dead cells with the default cluster finding algorithm in each event. The good photon clusters are paired to search possible π^0 candidates, and the mass spectrum of the photon pair with $p_t^{FMS} > 2.0 GeV/c$ in p+p collisions and d+Au collisions are shown in Figure 4.2. Combination of any two good photons with mass less than 0.2 GeV/c^2 are treated as π^0's candidates in the FMS. The normalized distributions of the invariant mass spectrum of photon pair reconstructed in the FMS in p+p and d+Au collisions is shown in Figure 4.2, the background fraction in the mass window ($M < 0.2 GeV/c^2$) is low. The mass distributions look similar in p+p collisions and d+Au collisions. The fraction of the background underneath the π^0 peak is small. Further study on subtracting the background of the FMS π^0 is ongoing, but this will not change the correlation results much.

4.4 Associated π^0 reconstruction in the BEMC and EEMC

Pion particles (π^+, π^- and π^0) occupy most of the multiplicity in particle production of collisions. Electromagnetic calorimeter like the BEMC or the EEMC has better characterization of neutral pions than charged hadrons. Consequently, π^0 meson is the primary particle reconstructed in the EEMC (or BEMC). Although the FMS-BEMC π^0-π^0 azimuthal correlations have been introduced in [12]. The FMS-BEMC correlation with a different threshold cluster finder from the cluster algorithm mentioned in [12] is treated as a reference for the FMS-EEMC correlation analysis, due to the larger coverage in η but lower pseudo-rapidity of BEMC compared to the EEMC. Another reason to do such study is both BEMC and EEMC has similar machine design, the reliability of the threshold bounded cluster finder can be test through the FMS-BEMC correlation by comparing the previous results in [12].

A tower energy threshold is needed to discriminate energy deposition of particles produced by collisions from electronic noises and fluctuation background. Simulation has ideal environment setting, thus there is no background produced by instrumental fluctuation effects. To find a reasonable energy threshold for further cluster finding algorithm for the EEMC, 1M PYTHIA [87]+GSTAR (GEANT 3 [92] with STAR geometry) simulated events of p+p collisions and 400K HIJING [88]+GSTAR simulated events with shadowing setup on or off are used to compare with FMS triggered data. The simulation samples are generated in the STAR detector running environments and have the RHIC run8 calibration table which are related with the online performance of the STAR detectors.

As the FMS has good resolution for π^0 and small background in the π^0 mass window ($M < 0.2 GeV/c^2$), there is no background subtraction in data in the current analysis. The tower multiplicity and tower energy after calibration in both BEMC and EEMC in data are compared with simulation. Threshold of the BEMC(EEMC) tower energy is tuned from 70MeV, 100MeV, 150MeV, 200MeV, 250MeV, 300MeV to 350MeV. Consequently, 250MeV is initially selected as threshold for data analysis

due to better agreement between data and simulation. With FMS π^0 ($p_t^{FMS} > 2.0 GeV/c$), for data and simulation comparison, the BEMC tower multiplicity and tower energy with 250MeV energy threshold in p+p and d+Au interactions are shown in Figure 4.3. The comparison for EEMC is shown in Figure 4.4. The distributions are normalized by number of events, 69 runs in p+p collisions and 38 runs in d+Au collisions are used in these comparisons.

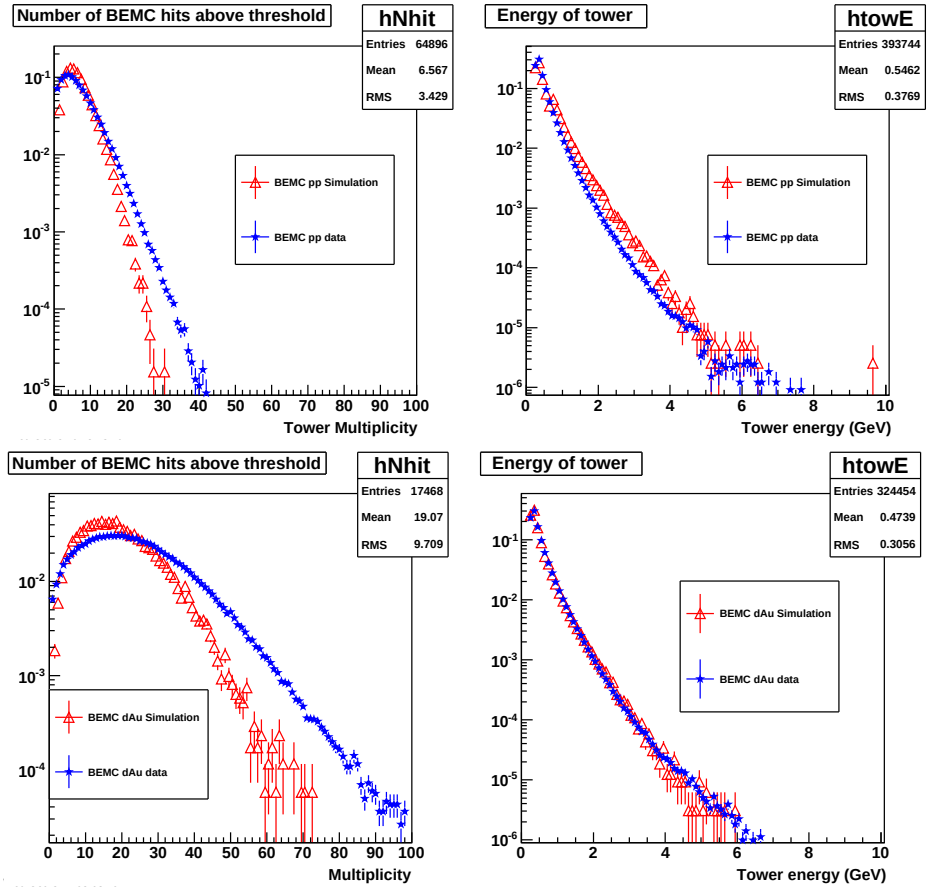

Figure 4.3: The distribution of the tower multiplicity (left) and the tower energy (right) in the BEMC with tower threshold 250MeV and FMS π^0 $p_t^{FMS} > 2.0 GeV/c$. The results in p+p collisions are presented in the top row and the results in d+Au collisions are shown in the bottom row.

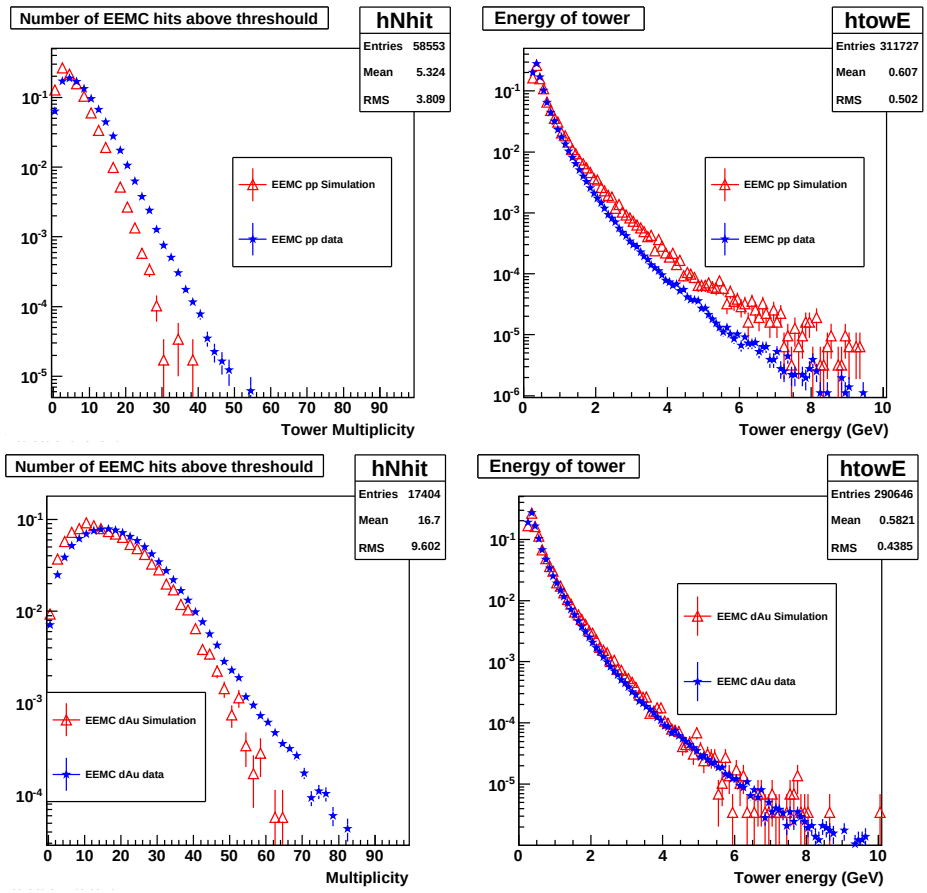

Figure 4.4: The tower multiplicity (left) and the tower energy (right) in the EEMC with tower threshold 250 MeV and FMS π^0 $p_t^{FMS} > 2.0 GeV/c$. The open triangular points stand for simulation and the solid star points stand for data. The results in p+p collisions are presented in the top row and the results in d+Au collisions are shown in the bottom row.

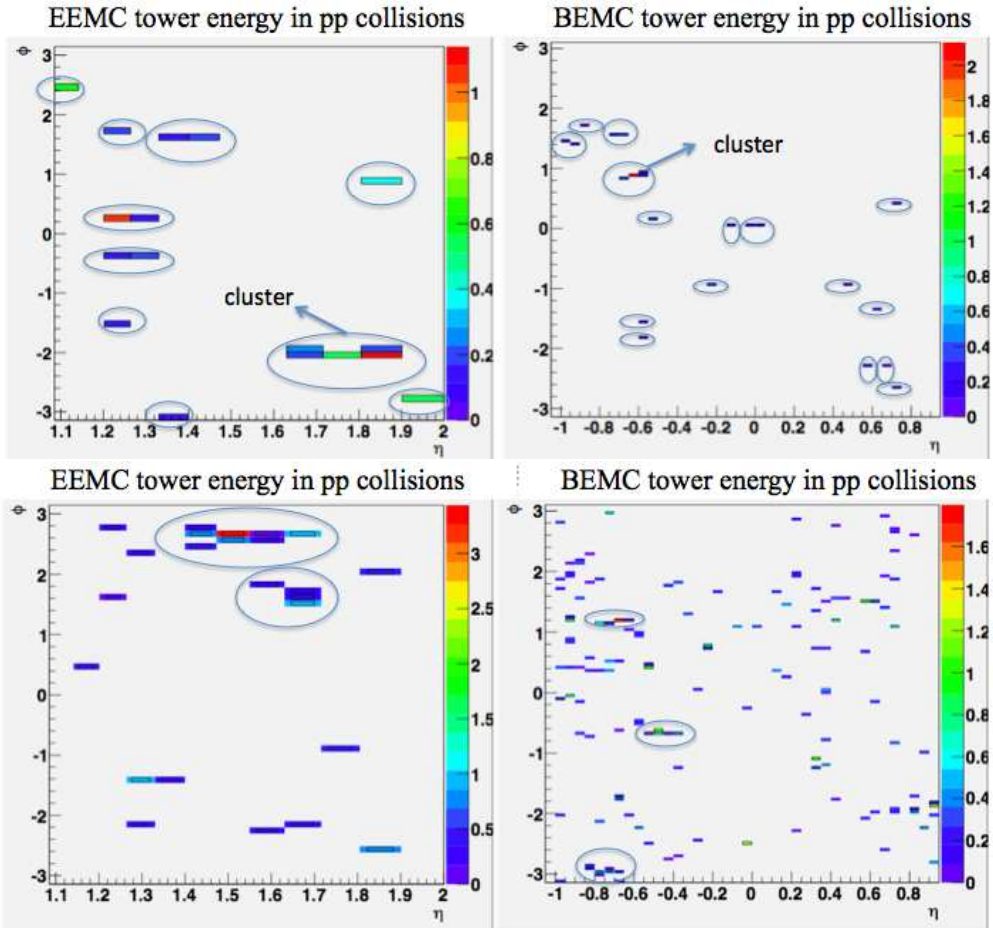

Figure 4.5: The EEMC tower energy deposited in one p+p collision event with FMS π^0 $p_t^{FMS} > 2.0GeV/c$ in $\eta\phi$ plane (x : η, y : ϕ) is shown in the top left panel. BEMC tower event display in one p+p event is shown in the top right panel. The color stands for the energy (GeV) of the tower. Circles stand for clusters found by the cluster finder. The results in d+Au collision event is show in the bottom plots.

A threshold (tower energy above 250MeV) bounded cluster finder is developed independently to search for photon candidates assuming the energy is from electromagnetic showers and the energy deposited by hadrons is small. Towers with energy below threshold are ignored in the analysis. The cluster finder uses the highest energy tower as seed, then find the adjacent towers connected to the highest energy tower. The adjacent tower is included in the cluster if its energy is above the energy threshold. This process continues until there are no towers above the energy threshold connected to the current cluster. Once a cluster is found, the cluster finder starts searching for the highest energy tower in the rest towers as a seed for the next cluster and so on until the towers are used up. The event display of tower energy and cluster schematics for EEMC and BEMC with 250MeV energy threshold in p+p collisions and d+Au collisions are shown in Figure 4.5. The energy of cluster

is defined as the sum of tower energy, and the x, y and z positions of clusters are calculated by the energy weighted mean values of towers composing cluster.

$$E_{cluster} = \sum_i E_i,$$
$$x_{cluster} = \frac{\sum_i E_i \times x_i}{E_{cluster}},$$
$$y_{cluster} = \frac{\sum_i E_i \times y_i}{E_{cluster}},$$
$$z_{cluster} = \frac{\sum_i E_i \times z_i}{E_{cluster}},$$

where i stands for the tower index in the cluster, x_i, y_i are the transverse components of center position of tower (index i) in the cluster and z_i is the distance from primary vertex to the SMD plane of EEMC or BEMC in z axis.

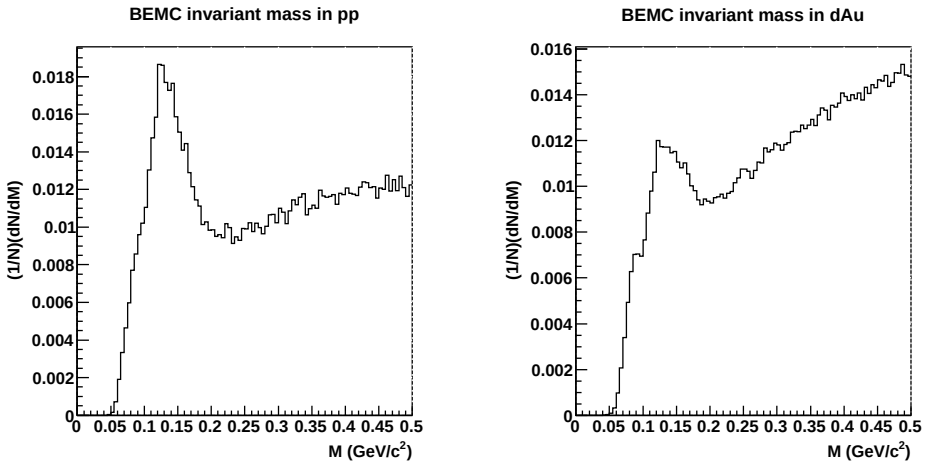

Figure 4.6: With FMS π^0 $p_t^{FMS} > 2.5 GeV/c$, the photon cluster pair masses in the BEMC with $1.5 GeV/c < p_t^{EEMC} < p_t^{FMS}$ in p+p collisions are shown in the left panel and the masses of the BEMC photon cluster pairs in d+Au collisions are shown in the right panel.

4.4.1 π^0 reconstructions in the BEMC

In order to check the consistence with the previous results of the FMS π^0 - BEMC π^0 azimuthal correlations [12], the threshold bounded cluster finder is firstly applied on the BEMC towers to get single photon clusters. As the the electromagnetic showers can be well determined in the electromagnetic calorimeters and the photon shower does not occupy large spatial area, photon candidates are searched in single clusters. Reconstruction of π^0 is realized by pairing photon candidates. The efficiency drops rapidly at the edges of the BEMC, so a fiducial volume cut $|\eta| < 0.9$ is applied to the clusters in the BEMC. The BEMC tower size is large compared to the photon electromagnetic shower size. The high multiplicity at RHIC leaves a large number

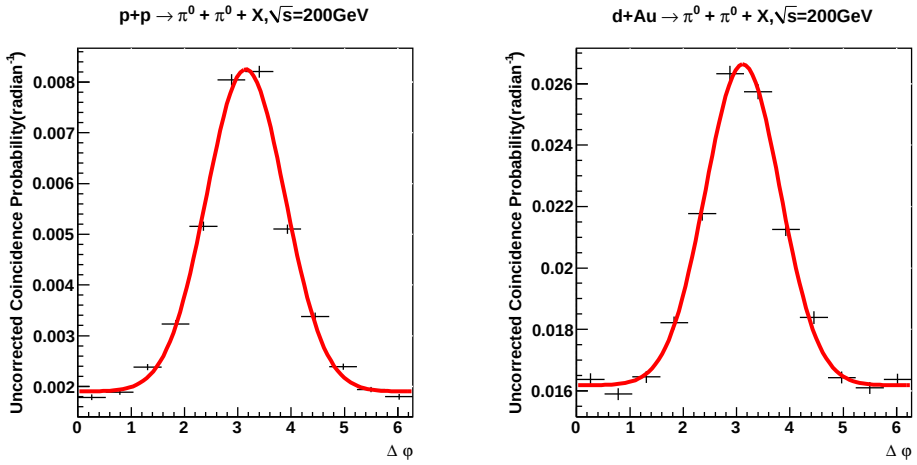

Figure 4.7: (Left) The uncorrected coincidence probability of FMS π^0 - BEMC π^0 azimuthal correlations with FMS π^0 $p_t^{FMS} > 2.5 GeV/c$ and BEMC π^0 $1.5 GeV < p_t^{BEMC} < p_t^{FMS}$ in p+p collisions. (Right) The azimuthal correlations of FMS π^0 - BEMC π^0 with the same p_t cuts in d+Au collisions.

of hits from multiple particles in the same electromagnetic calorimeter tower. A energy ratio defined as seed energy (E_{seed}) over cluster energy ($E_{cluster}$) is selected to be larger than 0.9 to suppress possible background. Clusters that satisfy these cuts are put into a photon candidates list. Two photon clusters are combined to form a photon cluster pair for further π^0 reconstructions. The energy sharing named with $z_{\gamma\gamma}$ is defined as,

$$z_{\gamma\gamma} = \frac{|E_1 - E_2|}{E_1 + E_2}, \tag{4.19}$$

where E_1 is the energy of one photon and E_2 is the energy of the other photon. Usually the energy sharing $z_{\gamma\gamma}$ of π^0 decayed photons are not large. In the BEMC π^0 reconstructions, cluster energy in associated pair is taken as E_1 or E_2 in Eq.(4.19). Di-photon pair is reconstructed with the energy sharing $z_{\gamma\gamma}$ less than 0.7. The energy of di-photon pair is defined as the sum of two photon cluster energy. The momentum of di-photon pair is the sum of photon cluster momentum vector and the mass is derived from its energy and momentum,

$$\begin{aligned} E_{di-clu} &= E_1 + E_2, \\ \vec{p}_{di-clu} &= \vec{p}_1 + \vec{p}_2, \\ M_{di-clu} &= \sqrt{(E^2_{di-clu} - \vec{p}^2_{di-clu})}. \end{aligned} \tag{4.20}$$

where E_{di-clu} is the energy of the di-photon pair, E_1 (or E_2) is the energy of the single photon cluster, $\vec{p}_{di-clu}$ is the momentum vector of the di-photon pair, $\vec{p}_1$ (or $\vec{p}_2$) is the momentum vector of the single photon cluster, and M_{di-clu} is the mass of the di-photon pair.

The invariant masses of photon cluster pairs in the BEMC for p+p and d+Au collisions with FMS triggered π^0 $p_t^{FMS} > 2.5 GeV/c$ and the BEMC cluster pair

$1.5GeV/c < p_t^{EEMC} < p_t^{FMS}$ are shown in Figure 4.6. As there are huge combinatory background (eg. photons not decayed from the same neutral meson) for $mass > 0.2GeV/c^2$ part, the photon cluster pairs with $mass < 0.2GeV/c^2$ are taken as π^0 candidates in the BEMC.

The uncorrected coincidence probabilities of FMS π^0 - BEMC π^0 azimuthal correlations in p+p and d+Au collisions are shown in Figure 4.7. To characterize the azimuthal correlations, results are fitted with a function $G(x)$ which is a constant plus a Gaussian function. The constant is to fit the background related with non-correlation part and the Gaussian function is to fit the peak of the correlation,

$$G(x) = A_0 + \frac{A_1}{\sqrt{2\pi}A_3} \times exp(-\frac{1}{2}(\frac{(x-A_2}{A_3})^2), \tag{4.21}$$

where A_0 is the constant, A_1 is the integral of the Gaussian function, A_3 is the width of the Gaussian function and A_2 is the centroid of the Gaussian function. The fitted parameters of $G(x)$ for correlations with different p_t cuts are summarized in Table 4.2. Two different p_t cuts are used. The one marked as "low p_t" is FMS π^0 $p_t^{FMS} > 2.0GeV/c$ and BEMC π^0 $1.0GeV/c < p_t^{BEMC} < p_t^{FMS}$. The other one marked as "high p_t is FMS π^0 $p_t^{FMS} > 2.5GeV/c$ and BEMC π^0 $1.5GeV/c < p_t^{BEMC} < p_t^{FMS}$. The fitted parameters look similar with previous results and the conclusion remains the same as shown in [12]. There is no significant broadening for FMS π^0 - BEMC π^0 azimuthal correlations from p+p interactions to d+Au interactions. This confirms the threshold bounded cluster finder works in the BEMC region.

4.4.2 π^0 reconstructions in the EEMC

As the EEMC has similar construction configuration as the BEMC, the same cluster finder can be applied to the EEMC. The rapidity dependence of the azimuthal correlations with FMS triggered π^0 provides sensitivity to the gluon density in different x_{BJ} regions. The EEMC covers the intermediate region $1.083 < \eta < 2.0$ between the BEMC ($|\eta| < 1.0$) and the FMS ($2.5 < \eta < 4.0$). Azimuthal correlations of FMS π^0 and EEMC hadron can probe lower x_{BJ} region than the FMS-BEMC correlations. EEMC is a fast detector and it has comparable readout rate as the FMS, which allows us to study the correlations of FMS π^0 and EEMC hadron. We will first represent details about the π^0 reconstruction in the EEMC, and next introduce the correlation results of FMS π^0 - EEMC π^0.

During data taken with the EEMC, several hot towers (towers always have signal due to electronic noise or something else) are identified. These hot towers have much higher (over 2 times) appearing frequency than other towers of the EEMC. These hot towers (ID = 456, 457, 458, 464, 526 and 697) are removed from the data analysis to reduce false signals. The threshold bounded cluster finder tested with the BEMC π^0 reconstruction is applied to the EEMC towers. The energy threshold is still 250MeV, which is about 4 ADC counts above pedestal for the EEMC. The event display has already been shown in Figure 4.5, circles stand for the clusters found by the threshold bounded cluster finder. Through the QA check over more

	FMS(π^0)-BEMC(π^0) in p+p (low p_t)	FMS(π^0)-BEMC(π^0) in d+Au (low p_t)
Constant	0.01303 ± 0.00005	0.1092 ± 0.0002
Integral	0.0535 ± 0.0003	0.08765 ± 0.0009
Centroid	3.1582 ± 0.00362	3.1769 ± 0.00607
Width	0.8556 ± 0.0049	0.798 ± 0.007
	FMS(π^0)-BEMC(π^0) in p+p (high p_t)	FMS(π^0)-BEMC(π^0) in d+Au (high p_t)
Constant	0.0019 ± 0.0000	0.01618 ± 0.00009
Integral	0.01172 ± 0.00017	0.01841 ± 0.00046
Centroid	3.1486 ± 0.0090	3.1181 ± 0.01384
Width	0.7361 ± 0.0112	0.7018 ± 0.0166

Table 4.2: Comparison between uncorrected correlations of FMS π^0 - BEMC π^0 in p+p interactions and d+Au interactions. The low p_t cut means the FMS π^0 $p_t^{FMS} > 2.0 GeV/c$ and BEMC π^0 (photon cluster pair $M < 0.2 GeV/c^2$) $1.0 GeV/c < p_t^{BEMC} < p_t^{FMS}$. The high p_t cut means the FMS π^0 $p_t^{FMS} > 2.5 GeV/c$ and BEMC π^0 (i.e. photon cluster pair with $M < 0.2 GeV/c^2$) $1.5 GeV/c < p_t^{EEMC} < p_t^{FMS}$. "Constant" stands for the pedestal below the Gaussian function, "Integral" is the integral of the Gaussian function above pedestal and "Width" stands for the σ of the Gaussian function. See the definitions in Eq.(4.21).

events, the threshold bounded cluster finder applied on the EEMC detector has been proved to work well in both p+p and d+Au collisions.

Although the EEMC tower size is larger than BEMC tower, the π^0's are reconstructed by taking single clusters as single photon candidates in the beginning. Clusters within $1.1 < \eta < 1.9$ and ratio of seed energy over cluster energy ($E_{seed}/E_{cluster}$) larger than 0.9 are included in the photon list. Moreover, combinatory pair of any two candidates in the photon list satisfying energy sharing $z_{\gamma\gamma} < 0.7$ (see Eq. 4.19) are taken as photon pair measured in the EEMC. The invariant mass of the EEMC photon cluster pairs with "high p_t" cuts and "low p_t" cuts in both p+p interactions and d+Au interactions are presented in the middle column of Figure 4.8. From Figure 4.8, data and simulation show good agreement for energy, invariant mass and p_t spectrum for the photon pair in both p+p collisions and d+Au collisions. There is a clear π^0 peak around $0.135 GeV/c^2$ above background in the invariant mass distributions of EEMC photon pairs in both p+p collisions and d+Au collisions. The background underneath the π^0 peak in d+Au collisions is larger than that in p+p collisions, which is related with higher particle multiplicity in d+Au interactions. The photon cluster pairs with $mass < 0.2 GeV/c^2$ are taken as π^0's candidates for the azimuthal correlation studies.

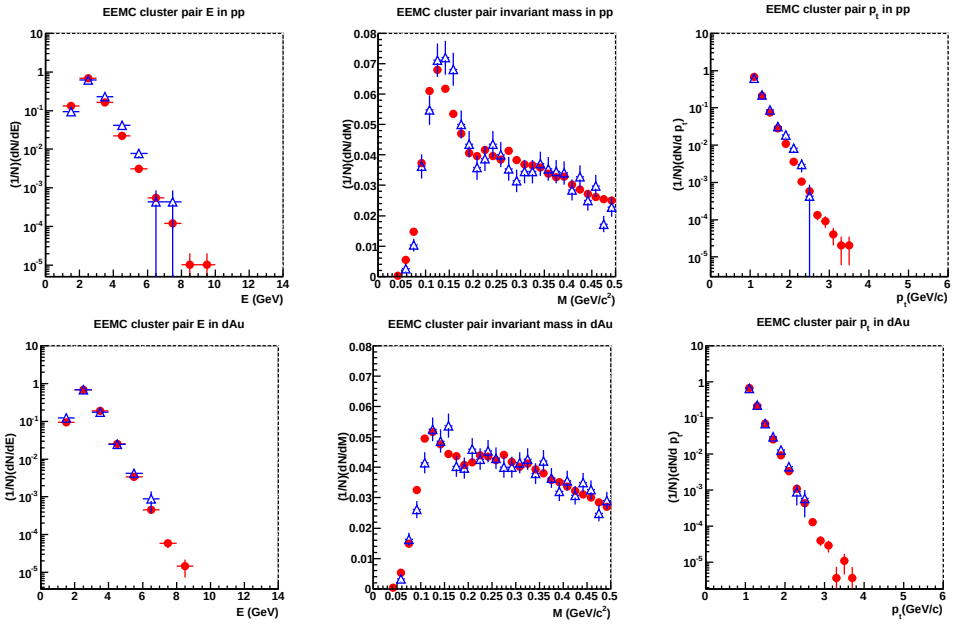

Figure 4.8: The energy (left) , invariant mass (middle) and p_t (right) distributions in data and simulation for EEMC cluster pairs with $1.0GeV/c < p_t^{EEMC} < p_t^{FMS}$ in events triggered by FMS π^0 with $p_t^{FMS} > 2.0GeV/c$. The results in p+p interactions are shown in the top row and d+Au studies are shown in the bottom row. Blue open triangle points stand for simulation and red solid circles stand for data.

The uncorrected coincidence probability of the FMS π^0 - EEMC π^0 correlations with different p_t cuts are shown in Figure 4.9. The azimuthal results with high p_t cut was released as STAR preliminary results in [1]. The correlations are also fitted with the same function $G(x)$ (see definition in Eq.(4.21)) used for the FMS-BEMC azimuthal correlations. The related parameters after fitting are shown in Table 4.3. The ratio of the integral of the Gaussian function over constant in d+Au collisions is much less than the same ratio in p+p collisions. The width difference between p+p collisions and d+Au collisions $\Delta(\sigma_{dAu} - \sigma_{pp})$ with "low p_t" cut is 0.372 ± 0.0651 and value for "high p_t" cut is 0.278 ± 0.0632. Therefore broadening signals for the FMS π^0 - EEMC π^0 azimuthal correlations from p+p interactions to d+Au interactions are observed with both low p_t cuts and high p_t cuts.

	FMS(π^0)-EEMC(π^0) in p+p (low p_t)	FMS(π^0)-EEMC(π^0) in d+Au (low p_t)
Constant	0.00123 ± 0.00002	0.005462 ± 0.000095
Integral	0.005193 ± 0.000107	0.008611 ± 0.000629
Centroid	3.187 ± 0.012	3.098 ± 0.025
Width	0.89 ± 0.02	1.262 ± 0.062
	FMS(π^0)-EEMC(π^0) in p+p (high p_t)	FMS(π^0)-EEMC(π^0) in d+Au (high p_t)
Constant	0.001269 ± 0.000025	0.006106 ± 0.000102
Integral	0.006122 ± 0.000154	0.008943 ± 0.000639
Centroid	3.173 ± 0.015	3.096 ± 0.031
Width	0.8247 ± 0.0197	1.103 ± 0.06

Table 4.3: Comparison between uncorrected correlations of FMS π^0 - EEMC π^0 in p+p interactions and d+Au interactions. The low p_t cut means the FMS π^0 $p_t^{FMS} > 2.0 GeV/c$ and EEMC π^0 (photon cluster pair $M < 0.2 GeV/c^2$) $1.0 GeV/c < p_t^{EEMC} < p_t^{FMS}$. The high p_t cut means the FMS π^0 $p_t^{FMS} > 2.5 GeV/c$ and EEMC π^0 (photon cluster pair $M < 0.2 GeV/c^2$) $1.5 GeV/c < p_t^{EEMC} < p_t^{FMS}$. "Constant" stands for the pedestal below the Gaussian function, "Integral" is the integral of the Gaussian function above pedestal, "Centroid" is the mean value of the Gaussian function and "Width" stands for the σ of the Gaussian function.

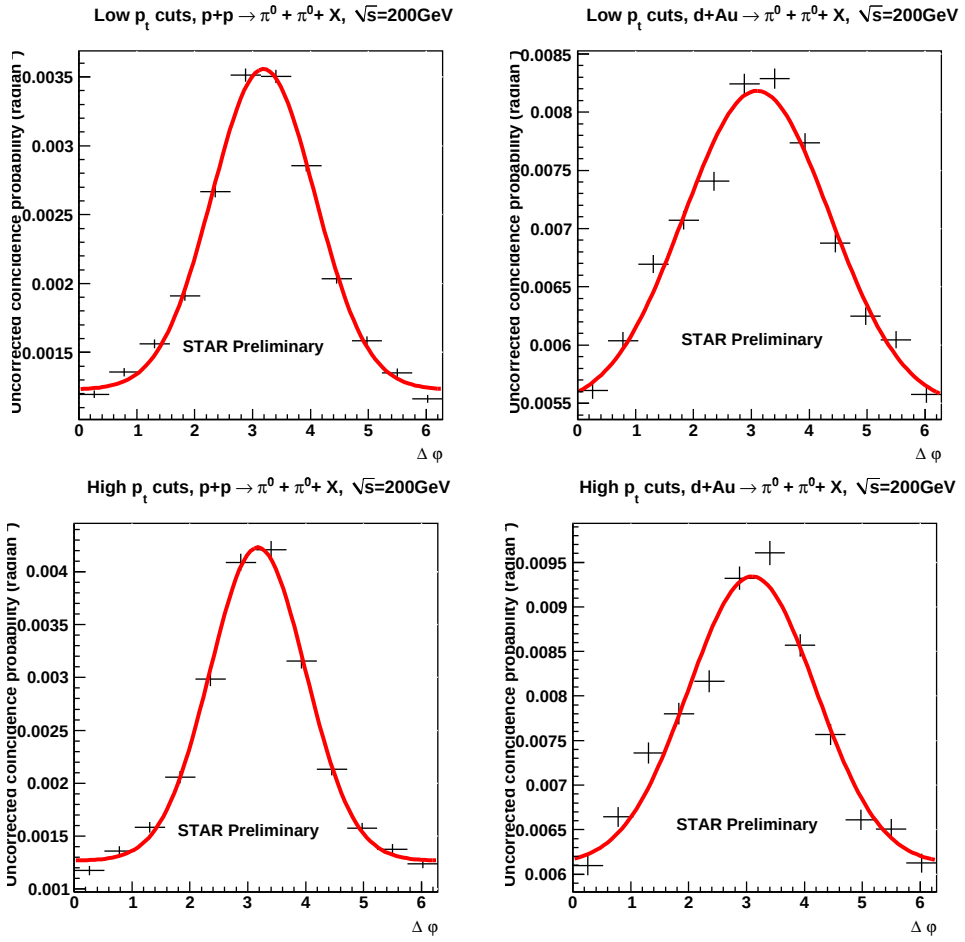

Figure 4.9: Top row: The uncorrected coincidence probability of FMS π^0 - EEMC π^0 azimuthal correlations with FMS π^0 $p_t^{FMS} > 2.0GeV/c$, EEMC π^0 $1.0GeV < p_t^{EEMC} < p_t^{FMS}$ in p+p collisions are shown in the left. The right panel shows the azimuthal correlations of FMS π^0 - EEMC π^0 with the same p_t cuts in d+Au collisions. Bottom row: With FMS π^0 $p_t^{FMS} > 2.5GeV/c$, EEMC π^0 $1.5GeV < p_t^{EEMC} < p_t^{FMS}$, the uncorrected coincidence probability of FMS π^0 - EEMC π^0 azimuthal correlations in p+p collisions are shown in the left. The right panel shows the azimuthal correlations of FMS π^0 - EEMC π^0 with the same p_t cuts in d+Au collisions. The red line stand for the fiting function $G(x)$ (see definition in Eq.(4.21)). The fitted parameters are shown in Table 4.3.

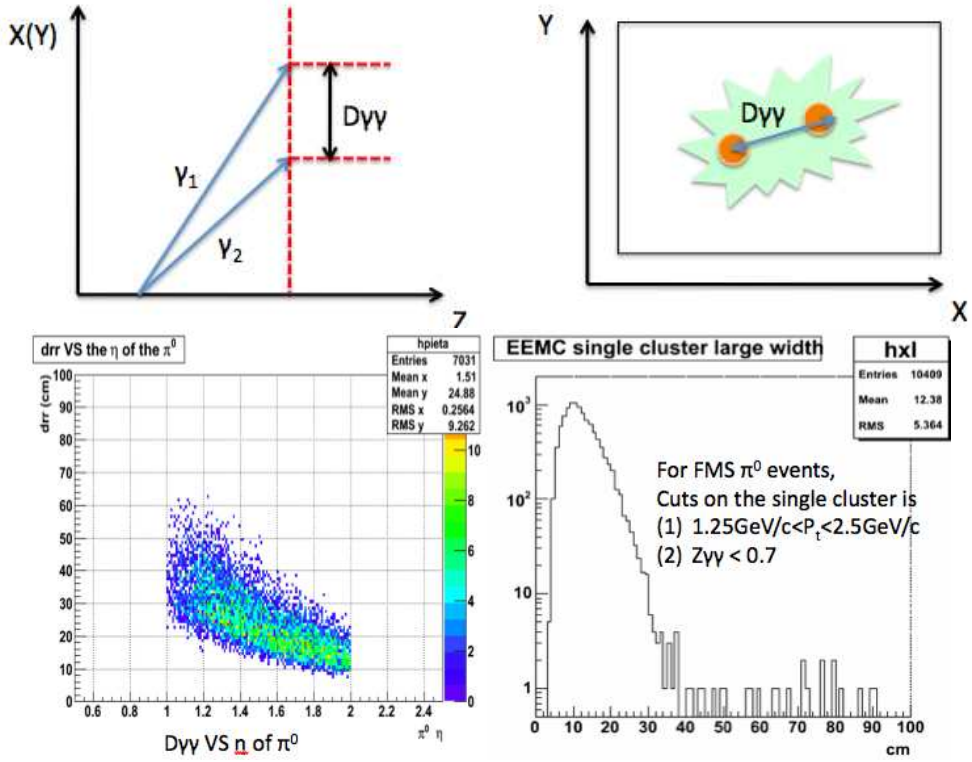

Figure 4.10: π^0 decay kinematics in the EEMC region. Projections of π^0 decay photon separation $d_{\gamma\gamma}$ in x(y)z plane or xy plane is shown in the top row. $d_{\gamma\gamma}$ versus the η of π^0 with $1.25GeV/c < p_t < 2.5GeV/c$ and energy sharing $z_{\gamma\gamma} < 0.7$ in fast simulator presented in the left bottom panel and the maximum width along major axis of EEMC single photon cluster with (1) $1.25GeV/c < p_t < 2.5GeV/c$ and (2) the energy sharing between the leading two towers inside the cluster less than 0.7 is shown in the right bottom panel. See the fitted parameters in Table 4.3

The uncorrected coincidence probability of FMS π^0 - EEMC π^0 azimuthal correlations with the di-cluster method is much lower than the FMS π^0 - BEMC π^0 correlations. With the same transverse momentum p_T, the particle energy at high pseudorapidity η_1 is larger than the particle energy at low pseudorapidity η_2 ($p_t \sim Esin(\theta) = E/cosh(\eta)$). The cross section drops exponentially as a function of energy, and this corresponds to the suppression of particle production at forward rapidity. For investigation, a fast simulator based on π^0 decay kinematics is developed to get the projection of the π^0 decayed photon separation in the EEMC. The top row of Figure 4.10 shows the schematics of the π^0 decayed photons in x(y)z plane and their separation $d_{\gamma\gamma}$ projected in the yz or xy two dimensional plane. To look more like real collisions, the primary vertex of a simulated event in the fast simulator is set to obey a Gaussian function with centroid at 0 cm and $\sigma = 30cm$. Separation of photons decayed from π^0 with $1.25GeV/c < p_t < 2.5GeV/c$ are projected in xy plane with z equal to the z position of the EEMC. Furthermore, the

π^0 is selected only with its decay daughter photons energy sharing $z_{\gamma\gamma} < 0.7$ to compare with data. With these cuts, the separation $d_{\gamma\gamma}$ versus the pseudorapidity of π^0 in $1.0 < \eta < 2.0$ region in the fast simulator is shown in the left bottom panel of Figure 4.10. The most probable value of $d_{\gamma\gamma}$ is around 25cm and $d_{\gamma\gamma}$ decreases as the η of π^0 increases.

The cluster pair usually has a large distance between each other in xy plane. A special case is considered when the two photons have energy deposited in the same cluster. π^0 signal is assumed to exist in single cluster. Then the leading two towers with maximum energy and second maximum energy are treated as surrogates of the photon inside the single cluster. The major axis width σ_{max} (see definition in Eq.(4.17)) stands for the maximum length of the single cluster. The energy inputs for the energy sharing $z_{\gamma\gamma} = \frac{|E_1 - E_2|}{E_1 + E_2}$ are different from cluster pair calculations. Here E_1 is the energy of leading tower and E_2 is the sub-leading tower energy in EEMC single cluster. Distribution of σ_{max} with requirements that transverse momentum of single cluster $1.25GeV/c < p_t < 2.5GeV/c$ and $z_{\gamma\gamma} < 0.7$ in p+p collisions (d+Au interaction have similar results) is shown in the right bottom panel of Figure 4.10. Although the average separation is about 12 cm, the width of EEMC tower (varied with different η region and a bit over 10cm) needs to be added as the calculation is based on tower center. Consequently, the separation value for π^0 decayed photon in fast simulator is not larger than the average major axis width of the single cluster in the EEMC. This applies to most of the π^0s in single clusters of the EEMC. The statistics of π^0 reconstruction in the EEMC is limited by the cluster pair strategy applied on larger towers and larger pseudo-rapidity coverage in the EEMC than the BEMC. Background subtraction to get clean π^0 candidates will reduce the coincidence probability of the FMS π^0 - EEMC π^0 further.

π^0 reconstructions within single cluster is tried but the resolution of the π^0 peak in the mass spectrum is not good as there is no clear photon identification in single cluster on tower level analysis. The absence of SMD in the EEMC (ESMD) information in the single cluster analysis leaves poor resolution of identifying isolated photons. The two ESMD planes which are orthogonal to each are designed to provide better position resolution and energy resolution for electromagnetic showers than the towers of the EEMC. A cluster finder with threshold is also created for the ESMD strips. The threshold is selected to be 2MeV which is a bit above the deposited energy from MIP in the scintillation of the ESMD strips. Energy deposited in the ESMD strips from single photons are studied event by event, but attempts to use the ESMD for π^0 reconstruction met some difficulties. One reason is that the ESMD strips are long enough to across several towers, and the energies measured in them have multiple sources. Another one is that the calibration of the nearly 7000 ESMD strips. The ESMD strips energy scales are calibrated using minimum ionizing particles (MIP) deposited energy. This is based on mean expected energy loss of a MIP in the scintillator. Identified electron from tracking system has well measured momentum, and ideally the energy of cluster in the calorimeter related to the electron equals to its momentum. So the energy measured in calorimeters can be calibrated properly with the help of tracking systems. The calibration of

the EEMC is expected to get improved with E/p method after the installation of the Forward GEM Tracker (FGT) in future, which provides tracking measurements covering the EEMC pseudo-rapidity range.

The FMS π^0 - EEMC π^0 azimuthal correlations are statistics limited due to the π^0 reconstruction in the EEMC is based on tower level. The EEMC tower size is larger compared to the FMS tower, therefore the energy of π^0 decayed photon pairs get merged in single tower in most events. On the other hand, a π^0 usually is the leading particle of a jet reconstructed in the electromagnetic calorimeters. The initial parton state should be independent of the final fragmentation process, the FMS π^0 + EEMC jet-like cluster azimuthal correlations can be another path to probe the gluon density inside the gold nuclei within the low x_{BJ} region between 0.003 and 0.02. The jet-like cluster reconstruction in the EEMC will be discussed in the following section.

4.5 Jet-like cluster reconstructions in the EEMC

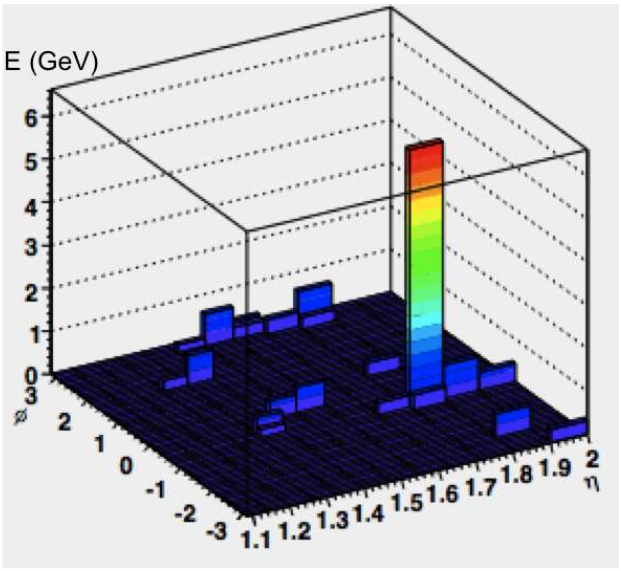

Figure 4.11: The 3D view of the EEMC energy deposition of one event in p+p collisions at 200GeV. The x axis stands for η, the y axis stands for ϕ and the z axis stands for energy (GeV).

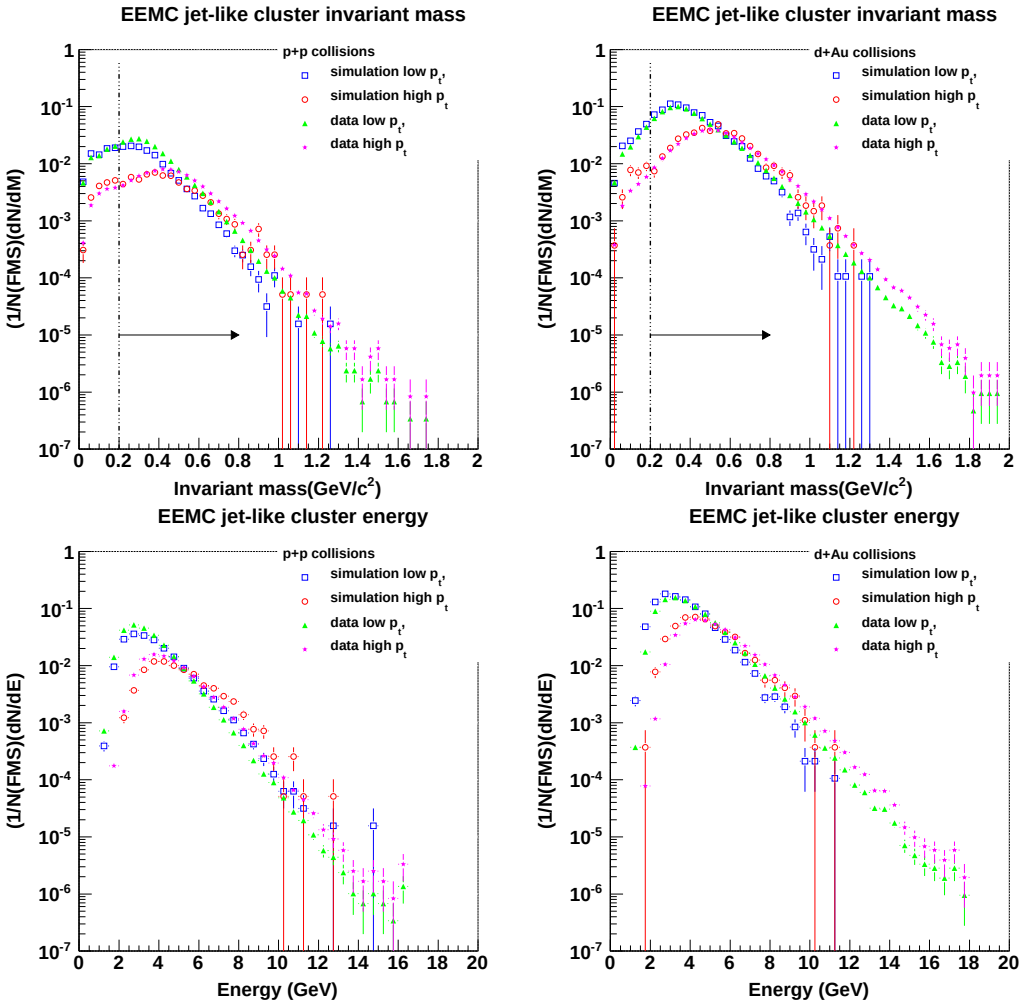

Figure 4.12: Left top panel: Mass spectrum of the EEMC jet-like cluster in p+p collisions. Left bottom panel: Energy spectrum of the EEMC jet-like cluster in p+p collisions. Right top panel: Mass spectrum of the EEMC jet-like cluster in d+Au collisions. Right bottom panel: Energy spectrum of the EEMC jet-like cluster in d+Au collisions. Blue empty squares stand for results with low p_t cuts in simulation, red empty circles stand for results with high p_t cuts in simulation, green solid triangles stand for results with low p_t cuts in data and magenta solid stars stand for results with high p_t cuts in data. The vertical dashed line in the mass spectrum stands for the mass equals to 0.2 GeV/c^2.

4.5. Jet-like cluster reconstructions in the EEMC

The initial states of partons before hard scattering are independent from the final hadron productions. Jets generated from partonic scattering keep the direction of the scattered partons, which is related with the kinematics of initial states. π^0's are usually the leading particles inside a jet. It's hard to track origins of final state hadrons in experiment. The jet measurement instead of π^0 can suppress the fluctuations from fragmentation processes. The FMS, BEMC and EEMC in our analysis are all electromagnetic calorimeters. A broad distribution of the deposited energy from hadronic shower makes it difficult to reconstruct full jet in the electromagnetic calorimeters. As the p_t region of interest for the correlation studies are low, jet-like clusters are reconstructed in the BEMC and EEMC based on cone algorithm with cone radius R = 0.6. Although the cone radius 0.6 is a bit large compared to the EEMC detector coverage, most of the energy of a jet is carried by several towers as shown in Figure 4.11. This means most of energy is accumulated around the center of a jet and the direction of a jet is determined by the several most energetic towers. As the azimuthal correlations are more sensitive to the jet direction not the jet energy, the results do not strongly depend on the cone radius selection for the jet-like clusters. Further studies including jet-shape analysis and cone radius dependence will be discussed later. The jet-like clusters reconstruction procedure is defined as the following:

(1) The x, y and z positions (using the SMD z position as the mean z position of whole tower) of towers inside the EEMC and BEMC are translated into η and φ values considering the primary vertex positions measured by the BBC event by event.

(2) Use the highest energy cluster as seed of super cluster and search through the towers. If the towers are within cone centered at the seed and radius $R = 0.6$ ($R = \sqrt{\eta^2 + \phi^2}$), the towers are included in the super cluster. The energy, averaged x, y and z positions and averaged η and ϕ values of the super cluster are calculated as the following,

$$
\begin{aligned}
E_{super} &= \sum_i E_i, \\
x_{super} &= \frac{\sum_i E_i \times x_i}{E_{super}}, \\
y_{super} &= \frac{\sum_i E_i \times y_i}{E_{super}}, \\
z_{super} &= \frac{\sum_i E_i \times z_i}{E_{super}}, \\
\eta_{super} &= \frac{\sum_i E_i \times \eta_i}{E_{super}}, \\
\varphi_{super} &= \frac{\sum_i E_i \times \varphi_i}{E_{super}},
\end{aligned}
\tag{4.22}
$$

where index "*super*" stands for super clusters, i stands for tower i inside the super cluster. A new iteration starts from the center of the super cluster to search whether more towers are within the cone radius ($R = 0.6$). This process will repeat until a stable super cluster is found or the iteration times reach the maximum iteration

number 5 (This number is set to avoid oscillation of the super cluster center). The last step is to remove towers outside the cone radius and all the parameters shown in equation 4.22 will be recomputed. Once a super cluster is found, the cone super cluster finder continues working on the rest towers until all towers are divided into different super clusters.

(3) As there is no fast tracking system which provides good momentum measurements in the EEMC, the momentum of each tower approximately equals to it energy. The direction of momentum vector of tower is from primary vertex to the tower center. The magnitude of the super cluster momentum vector is defined to be equal to the sum of momentum vector of towers inside the super cluster,

$$p_{super} = |\sum_i \vec{p}_i|. \tag{4.23}$$

The direction of the super cluster momentum is taken as the direction from the primary vertex to the super cluster center. The mass of the super cluster is,

$$M_{super} = \sqrt{E_{super}^2 - p_{super}^2}. \tag{4.24}$$

From previous studies of π^0 reconstruction, the mass of π^0 candidates are selected to be below $0.2GeV/c^2$. So the jet-like clusters are chosen to be super clusters with mass larger than $0.2GeV/c^2$ to get rid of single hadron component like π^0.

Events with FMS π^0s in a certain p_t region are used for jet-like cluster reconstruction in the EEMC (or BEMC). Same p_t cuts are applied to the associated jet-like clusters as for the associated π^0. There are two different p_t cuts: (1) high p_t cuts: FMS π^0 $p_t^{FMS} > 2.5GeV/c$ and EEMC(BEMC) jet-like cluster $1.5GeV/c < p_t^{EEMC} < p_t^{FMS}$; (2) low p_t cuts: FMS π^0 $p_t^{FMS} > 2.0GeV/c$ and EEMC(BEMC) jet-like cluster $1.0GeV/c < p_t^{EEMC} < p_t^{FMS}$. 1×10^6 PYTHIA+GSTAR events and 2×10^5 HIJING+GSTAR simulation events are used to compare with data. The mass and energy spectra of super clusters in the EEMC with the two different p_t cuts in both data and simulation are shown in Figure 4.12. The distributions of super cluster mass (or energy) are normalized by the number of FMS triggered π^0 to show the probability per trigger. For the normalized mass (see the top panel of Figure 4.12) and energy distribution (see the bottom panel of Figure 4.12), data and simulation are in good agreement both in p+p collisions and in d+Au collisions. There are no significant differences for the shape of the jet-like cluster mass between p+p and d+Au interactions. This suggests that the jet-like clusters are not dependent on the collision system although d+Au collisions have higher multiplicity than p+p collisions. The FMS π^0 - EEMC jet-like cluster azimuthal correlations will be studied in next chapter.

The spatial distribution of energy inside the jet-like cluster in $\eta - \phi$ plane which characterizes the jet-like cluster jet shape is studied. The schematics of a jet-like cluster using cone radius 0.6 cluster finder is shown in Figure 4.13. The jet-like cluster center is calculated from the energy weighted positions. The distance from the tower center inside jet-like cluster to the jet-like cluster center is marked as r_i,

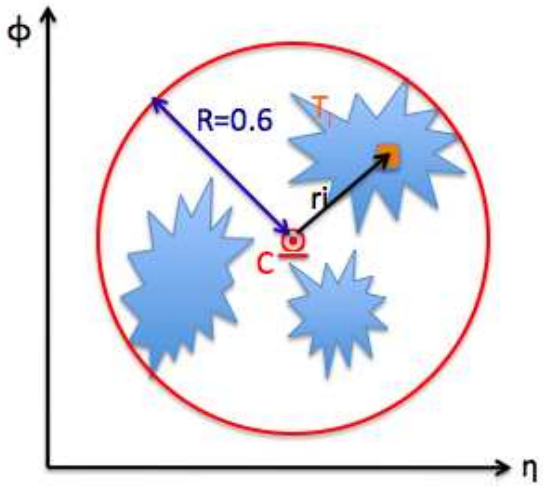

Figure 4.13: Schematics of jet-like cluster in $\eta - \phi$ plane. The distance from tower i center T_i to the jet-like cluster center C is marked as r_i. The radius of the cone cluster finder to reconstruct the jet-like clusters is R = 0.6.

and the ratio of tower energy over total jet-like cluster energy (dE/dR) versus r_i represents the energy spatial distribution inside the jet-like cluster. The η, φ of the vector from primary vertex to the jet-like cluster center is defined as the jet-like cluster η, φ values which are used for further detector acceptance studies.

The jet shape studies for the EEMC jet-like cluster in p+p and d+Au collisions including simulation and data are shown in Figure 4.14. The jet shape of EEMC jet-like clusters dE/dR has good agreement between data and simulation with both low p_t and high p_t cuts.

The jet profiles ($(1/\sum E)dE/dR$) of the EEMC jet-like clusters with high p_t cut and low p_t cut have good agreements between data and simulation (see Figure 4.14). Although the jet shape of jet-like clusters in p+p collisions is generally comparable with that in d+Au collisions, the energy inside the jet-like cluster decreases more rapidly from the jet-like cluster center to its edge in p+p collisions than in d+Au collisions. This indicates that there are more underlying events contributions to the jet-like clusters in d+Au collision due to higher multiplicity of particles than in p+p collisions provides a broad jet shape. The jet-like clusters with low p_t cuts have a broad jet shape than those with high p_t cuts. This reflects that the underlying events have p_t dependence and their contribution decreases as p_t increases.

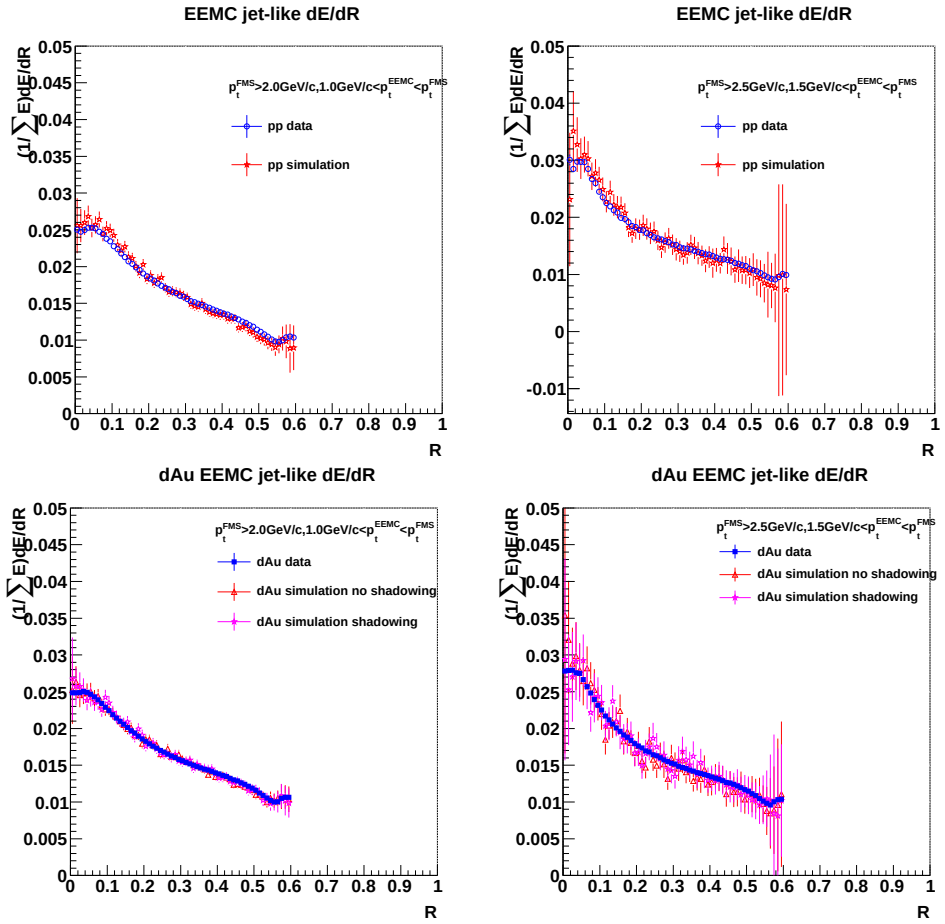

Figure 4.14: The jet shape studies in p+p interactions (top row) and d+Au interactions (bottom row). The jet profile of the EEMC jet-like cluster ($(1/\sum E)dE/dR$) with $mass > 0.2GeV/c^2$ and low p_t cuts ($1.0GeV/c < p_t^{EEMC} < p_t^{FMS}$ with coincident FMS π^0 $p_t^{FMS} > 2.0GeV/c$) is shown in the left panel and the jet profile of the EEMC jet-like cluster ($(1/\sum E)dE/dR$) with $mass > 0.2GeV/c^2$ and high p_t cuts ($1.5GeV/c < p_t^{EEMC} < p_t^{FMS}$ with coincident FMS π^0 $p_t^{FMS} > 2.5GeV/c$) is shown in the right panel.

4.5.1 Quality check : run dependence studies

The above section shows the jet-like cluster reconstruction without run selections in both p+p collisions and d+Au collisions. As the performance of the RHIC collider and STAR detectors may change in different time periods, we study the run dependence of the EEMC jet-like cluster characteristic parameters. One quantity is the average number of the EEMC jet-like clusters per FMS π^0 trigger $\frac{<N_{EEMC}(jet)>}{<N_{FMS}(\pi^0)>}$ in each run which shows the coincident probability of the EEMC jet-like clusters per FMS π^0 trigger. The other is the average energy of EEMC jet-like clusters $< E_{EEMC}(jet) >$ (GeV) in the FMS π^0 triggered events for each run which reflects the gain shifts for the EEMC tower run by run. Figure 4.15 shows the run dependence for the EEMC jet-like clusters ($M > 0.2GeV/c^2$) with $1.0GeV/c < p_t^{EEMC} < p_t^{FMS}$ in events triggered by FMS π^0 ($p_t^{FMS} > 2.0GeV/c$) in p+p collisions. The results in d+Au collisions are presented in Figure 4.16. The QA studies in high p_t cuts events which contain the coincident pairs of FMS π^0 with $p_t^{FMS} > 2.5GeV/c$ and the EEMC jet-like clusters with $1.5GeV/c < p_t^{EEMC} < p_t^{FMS}$ have similar structure as the low p_t cuts events.

A criteria defined as $0.12 < \frac{<N_{EEMC}(jet)>}{<N_{FMS}(\pi^0)>} < 0.14$ (dashed lines in the top panel of Figure 4.15) stands for the upper and lower limits for the good run criteria in p+p collisions. Runs outside such region are excluded for the further data analysis. The quality check is studied in d+Au collision independently (see the top panel of Figure 4.16) and the criteria is set as $0.33 < \frac{<N_{EEMC}(jet)>}{<N_{FMS}(\pi^0)>} < 0.4$. The mean values of the EEMC jet-like cluster energy in p+p collisions and d+Au collisions are shown in the bottom panels of Figure 4.15 and 4.16. The coincident yield of the EEMC jet-like clusters (the top panel) is correlated with the energy spectrum of the EEMC jet-like clusters (the bottom panel). There are around 5% variances in the EEMC jet-like cluster energy run dependence distribution, which is related with the EEMC detector gain shifts between different towers. The average $\frac{<N_{EEMC}(jet)>}{<N_{FMS}(\pi^0)>}$ shown in the top panel of Figure 4.15 and 4.16 has larger variances. As the energy spectrum dN/dE is a steeply decreasing distribution, the 5% change of the energy can lead to about 20% variances of the EEMC jet-like cluster yields. Only the good runs are used in the data analysis which will be introduced in the next chapter.

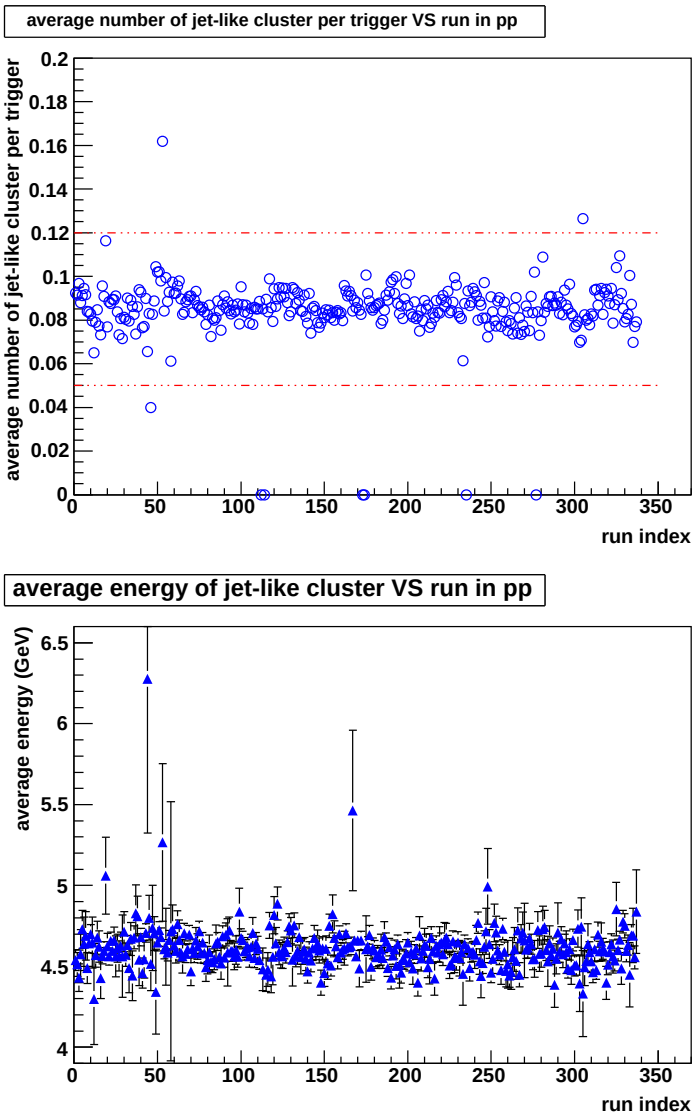

Figure 4.15: Quality check for EEMC jet-like clusters ($M > 0.2GeV/c^2$) with $1.0GeV/c < p_t^{EEMC} < p_t^{FMS}$ in events triggered by FMS π^0s ($p_t^{FMS} > 2.0GeV/c$) in p+p collisions. The FMS π^0 mass spectrum is shown in Figure 4.2, and the mass spectrum of the associated EEMC jet-like clusters is shown in the top panel of Figure 4.12. The run dependence of the average number of EEMC jet-like clusters per FMS π^0 trigger $\frac{<N_{EEMC}(jet)>}{<N_{FMS}(\pi^0)>}$ is shown in the top panel. X axis is the run index which is a sorting number for real run number. The dashed lines stand for the good run criteria $0.12 < \frac{<N_{EEMC}(jet)>}{<N_{FMS}(\pi^0)>} < 0.14$. The average EEMC jet-like cluster energy $< E_{EEMC}(jet) >$ (GeV) in FMS π^0 triggered events per run is shown in the bottom panel. The energy spectrum of the associated EEMC jet-like clusters is shown in the bottom panel of Figure 4.12.

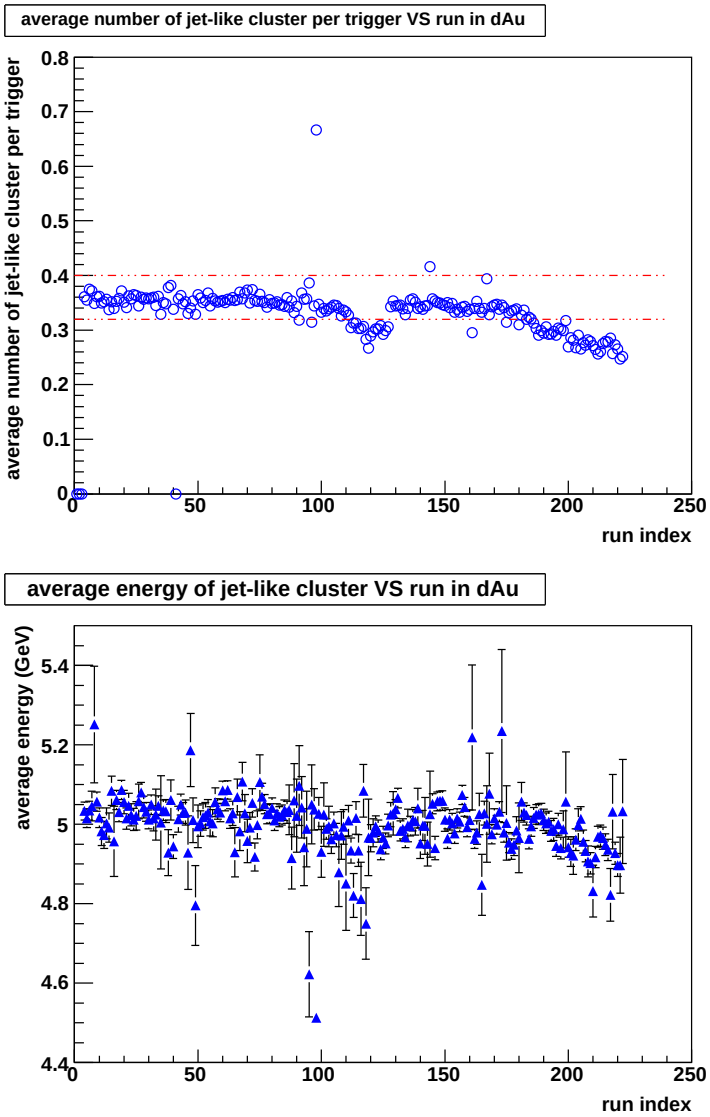

Figure 4.16: Quality check for EEMC jet-like clusters ($M > 0.2GeV/c^2$) with $1.0GeV/c < p_t^{EEMC} < p_t^{FMS}$ in events triggered by FMS π^0s ($p_t^{FMS} > 2.0GeV/c$) in d+Au collisions. The FMS π^0 mass spectrum is shown in Figure 4.2, and the mass spectrum of the associated EEMC jet-like clusters is shown in Figure 4.12. The run dependence of the average number of EEMC jet-like clusters per FMS π^0 trigger $\frac{<N_{EEMC}(jet)>}{<N_{FMS}(\pi^0)>}$ is shown in the top panel. X axis is the run index which is a sorting number for real run number. The criteria of good run is $0.33 < \frac{<N_{EEMC}(jet)>}{<N_{FMS}(\pi^0)>} < 0.4$ which is represented by the dashed lines. The average EEMC jet-like cluster energy $< E_{EEMC}(jet) >$ (GeV) in FMS π^0 triggered events per run is shown in the bottom panel. The around 30% dropping of the $\frac{<N_{EEMC}(jet)>}{<N_{FMS}(\pi^0)>}$ distribution at the end of d+Au collisions shown in the top panel is correlated with the 5 % variances of the $< E_{EEMC}(jet) >$ distribution shown in the bottom panel. The energy spectrum of the associated EEMC jet-like clusters is shown in the bottom panel of Figure 4.12.

Chapter 5

Azimuthal correlations results and discussion

In this chapter, we first present the uncorrected coincidence probability of the FMS π^0 and the EEMC jet-like cluster azimuthal correlations. A series of systematic checks are performed. The impacts of non-uniform detector acceptance and underlying contributions to the jet-like clusters will be firstly discussed in this chapter. The azimuthal correlations after corrections will be given later. Another question is how deep inside the gold nuclei the probe can reach. The centrality dependence studies related with this question in d+Au collisions will be discussed. The azimuthal correlation with a deuteron beam neutron tag in d+Au collisions related with the pedestal underneath the correlations will be presented as well.

5.1 Mixed events studies to remove detector acceptance effects

As we discussed in chapter 3, the towers of the EEMC may not work all the time during experiment operation period. As there are some electronic hardware issues including cable disconnection, DAQ readout failure and so on, usually there exist some dead or non-active areas in detectors when the data were taken. From the studies in the previous section, good runs contain more uniform detector acceptance than the bad runs. The detector non-uniformity can be caused by the calibration relevant gain shifts, single beam remnant background, the status of cells, electronic readout failure and etc. The acceptance holes or non-uniform detector acceptance may lead to non-physical structures in the azimuthal correlation results. Therefore, the azimuthal correlation results shown in chapter 3 should remove such detector acceptance effects to get physical results. Mixed events method is one way to reduce the impacts of non-uniform acceptance. The algorithm of the mixed events and the correction of correlation results will be discussed in this section.

5.1.1 Mixed event algorithm

The uncorrected FMS-EEMC azimuthal correlations shown before are obtained from events that contain at least two good photon candidates in the FMS. For the mixed events studies, the FMS π^0s and the EEMC jet-like clusters are required to be in different events with minimum bias selections on the triggers to see the impacts from the detector acceptance. During the online data acquisition, multiple triggers

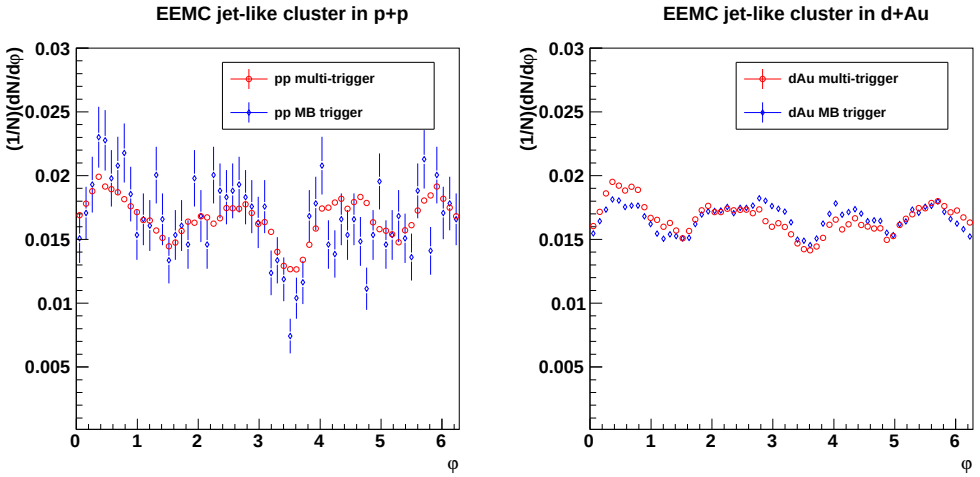

Figure 5.1: The φ distribution of EEMC jet-like clusters ($mass > 0.2GeV/c^2$) with $p_t^{EEMC} > 1.0GeV/c$ with no FMS π^0 requirements in p+p collisions (left panel) and d+Au collisions (right panel). Open circles corresponds to events with MB + FMS LED + east FPD multi-triggers and the open diamonds are only in events with the MB trigger.

are applied simultaneously in every collision event. In the mixed events studies, the π^0's reconstruction in the FMS is still studied in events with the FMS HT trigger events. However, the jet-like clusters are independently reconstructed in the EEMC with events containing different triggers except the FMS HT trigger.

Initially, the Minimum Bias trigger (MB) events are selected for the EEMC jet-like cluster reconstructions to reduce biases from the trigger detectors. As the MB events in p+p interactions only occupy a small fraction of the whole data collection and the mixed event results of low statistics are not reliable, we use another path to accumulate enough events for the EEMC jet-like cluster reconstructions. During the data acquisition, there are events with the LED trigger which generates the LED light pulses to monitor the status of the FMS cells. On the other hand, the east Forward Particle Detector (east FPD, locating at the east side of the beam interaction position of STAR) triggered events were included in the FMS data stream. These two triggers are independent of the FMS high tower trigger, therefore we use events with MB + FMS LED + east FPD trigger as a separate sample from the FMS π^0 events to reconstruct EEMC jet-like cluster. These two additional triggers contain further trigger requirements than the MB trigger, and the differences for the EEMC response between the multi-trigger and the MB trigger are studied. Figure 5.1 shows the normalized raw φ distributions of the EEMC jet-like clusters with $p_t^{EEMC} > 1.0GeV/c$ and $mass > 0.2GeV/c^2$ in MB trigger (blue open diamonds) and the MB + FMS LED + east FPD multi-trigger (red open circles) samples in p+p collisions (left panel) and d+Au collisions (right panel). The φ distribution in the multi-trigger sample looks similar as the MB trigger sample in both p+p collisions and d+Au collisions. The biases from the east FPD trigger and the FMS

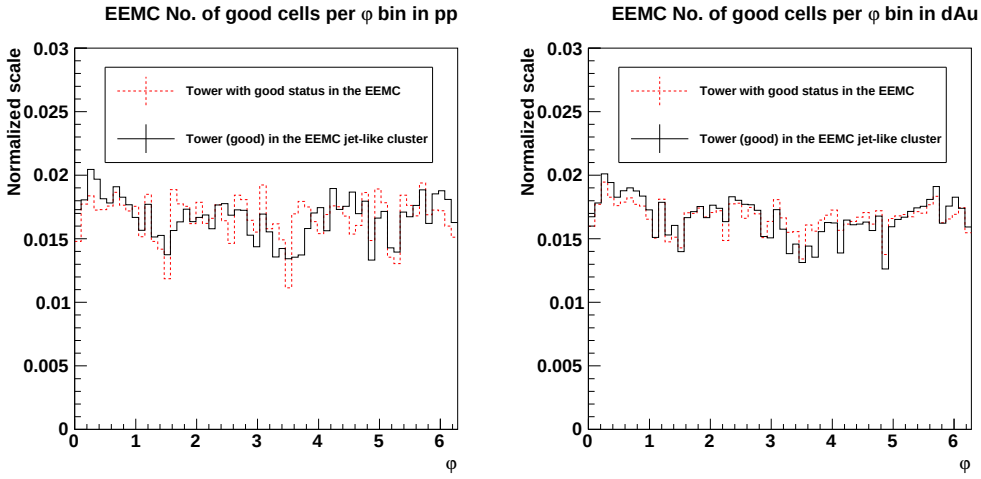

Figure 5.2: Comparisons between the normalized distribution of the towers with good status (with energy above 250MeV threshold) in the EEMC and the normalized distribution of towers with good status (with energy above 250MeV threshold) in the EEMC jet-like clusters with $mass > 0.2GeV/c^2$ and $p_t^{EEMC} > 1.0GeV/c$ in the multi-trigger events. The red dashed line stands for the normalized distribution of the EEMC towers with good status in each EEMC φ bin and the black solid line stands for the normalized distribution of the EEMC towers with good status from the EEMC jet-like clusters. The results in p+p collisions are shown in the left panel and the d+Au results are shown in the right panel.

LED trigger are small so they can be neglected.

The detector acceptance effects from the FMS can be cancelled out, as the probability of the correlations are divided by the FMS trigger. To dig out the possible source for the non-uniformity of the EEMC detector as shown in Figure 5.1, the status of the EEMC tower that masks this tower is usable is studied. The 720 EEMC cells distribute uniformly in the 60 φ bins, and the number of towers with valid status (excluding hot towers) is calculated in each φ bin in each event for both p+p and d+Au collisions. The normalized distribution of the average number of cells with good status for each EEMC φ bin in p+p and d+Au interactions with multi-triggers (the dashed line) are shown in Figure 5.2. In addition to this, the normalized φ distributions of the EEMC towers used to reconstruct the EEMC jet-like clusters ($mass > 0.2GeV/c^2$ and $p_t^{EEMC} > 1.0GeV/c$) in p+p and d+Au events with multi-triggers are presented in Figure 5.2 as well (the solid line). The φ distribution of the towers inside the jet-like clusters reconstructed in the EEMC, has similar structure as the jet-like cluster φ distribution (see Figure 5.1). It is a bit different from the EEMC towers only with the good status requirement especially in p+p collisions. This may be related with the yield of EEMC towesr changed by the gain shift between different towers of the EEMC. From the QA checks (see Figure 4.15 and 4.16) introduced in chapter 4, the energy variance of the jet-like clusters can result in the relevant yield variances.

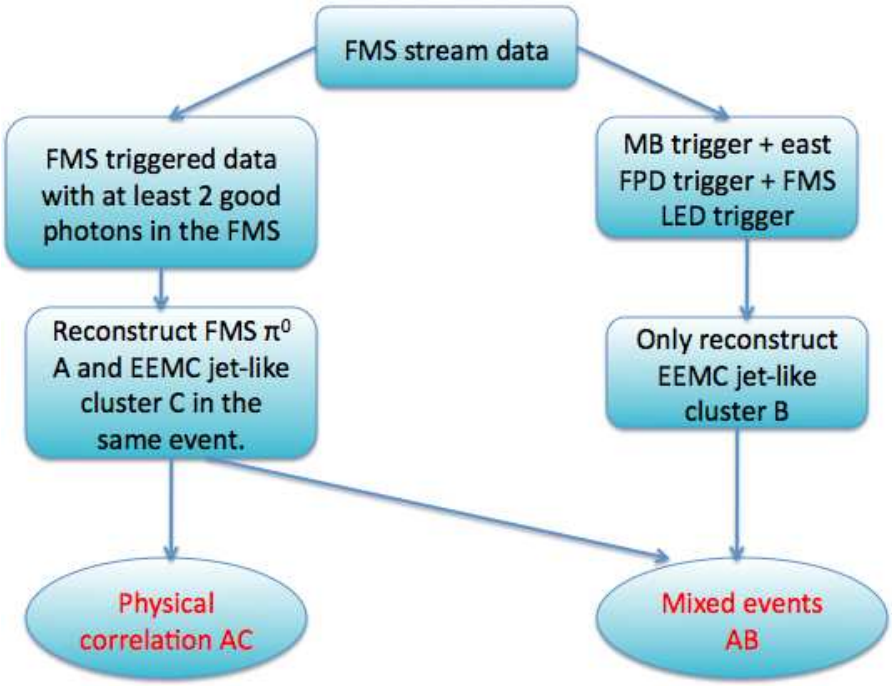

Figure 5.3: The mixed event algorithm

The algorithm of mixed events is shown in Figure 5.3. The reconstruction of the leading π^0 in the FMS are selected in the events with at least two good photon clusters recorded in the FMS (Sample A). The EEMC jet-like clusters are searched in events without good photons in the FMS, and actually are Minimum Bias + FMS LED + the east FPD trigger events (Sample B). Figure 5.4 shows the φ distributions of the FMS π^0 with $p_t^{FMS} > 2.0 GeV/c$ cut in sample A (left panel) and the EEMC jet-like clusters ($M > 0.2 GeV/c^2$) with $p_t^{EEMC} > 1.0 GeV/c$ cuts within sample B (right panel) in both p+p and d+Au collisions. In the coincident correlation analysis, the p_t^{EEMC} requirement for the EEMC jet-like cluster has a upper limit that is defined as the p_t^{FMS} of the leading FMS π^0. While in sample B, there is no reference like the triggered π^0 in the FMS, the upper limit is removed and only lower limit is used to be consistent with the coincident correlation studies. The structure in the φ distribution of the FMS π^0 is due to the FMS HT trigger effects (eg. non uniform gain resulting in non uniform acceptance of the triggered particles).

The reason for the blank region in the bottom left plot of Figure 5.4 is that only the south part of the FMS is within the DAQ triggering during run8 d+Au operation. As mentioned in chapter 3, the data taken from the EEMC, BEMC or TPC have requirements to be within the time period of trigger recorded by the DAQ system. As the data from the north FMS come later than the other detectors for DAQ trigger writing, only the south FMS is used for the correlation analysis between a leading π^0 in the FMS and an associated particle in the EEMC, BEMC or TPC during d+Au interactions of RHIC run8. As for the forward+forward correlations,

the L2 trigger contains trigger crossing, pre-crossing and post-crossing data, which provides full azimuthal coverage for the FMS-FMS correlations. However, the full azimuthal coverage is not a requirement for correlations of particles measured in independent detectors. The φ distribution of the FMS π^0 is still symmetric, and the raw correlations of the FMS π^0 and the EEMC jet-like clusters are still symmetric as shown in Figure 5.4.

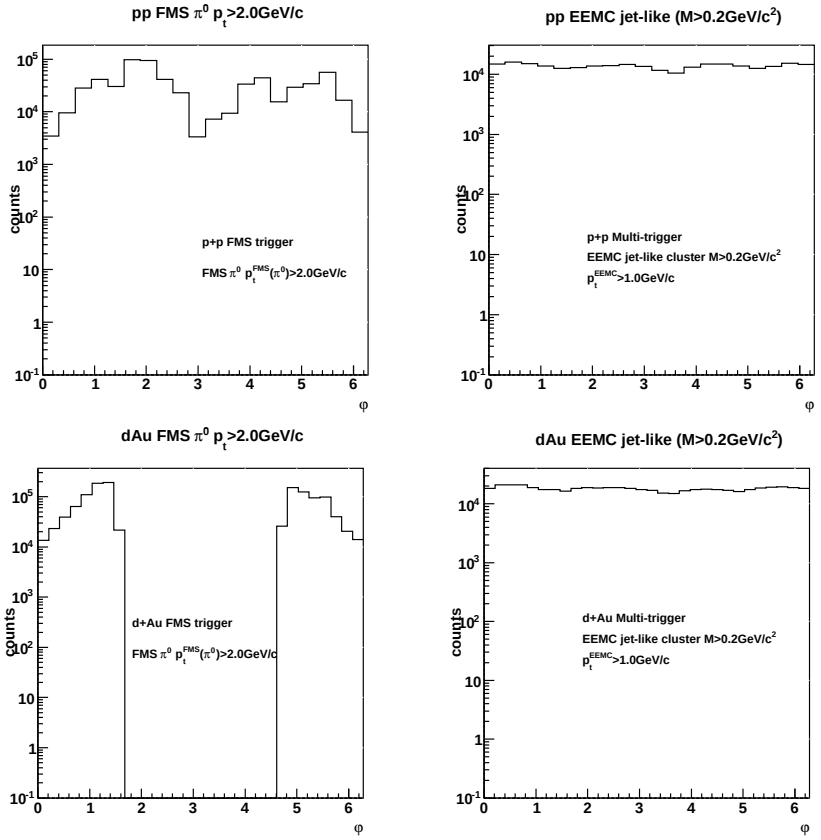

Figure 5.4: The top row: the φ distribution of the reconstructed FMS π^0 (left) and the φ distribution of the reconstructed EEMC jet-like cluster (right) in p+p collisions. The bottom row: the φ distribution of FMS π^0 (left) and the φ distribution of EEMC jet-like cluster (right) in d+Au collisions. The gap of the FMS φ distribution in d+Au collision is due to the North FMS different time crossing period from the DAQ system. The north FMS is not used for the FMS-EEMC correlations.

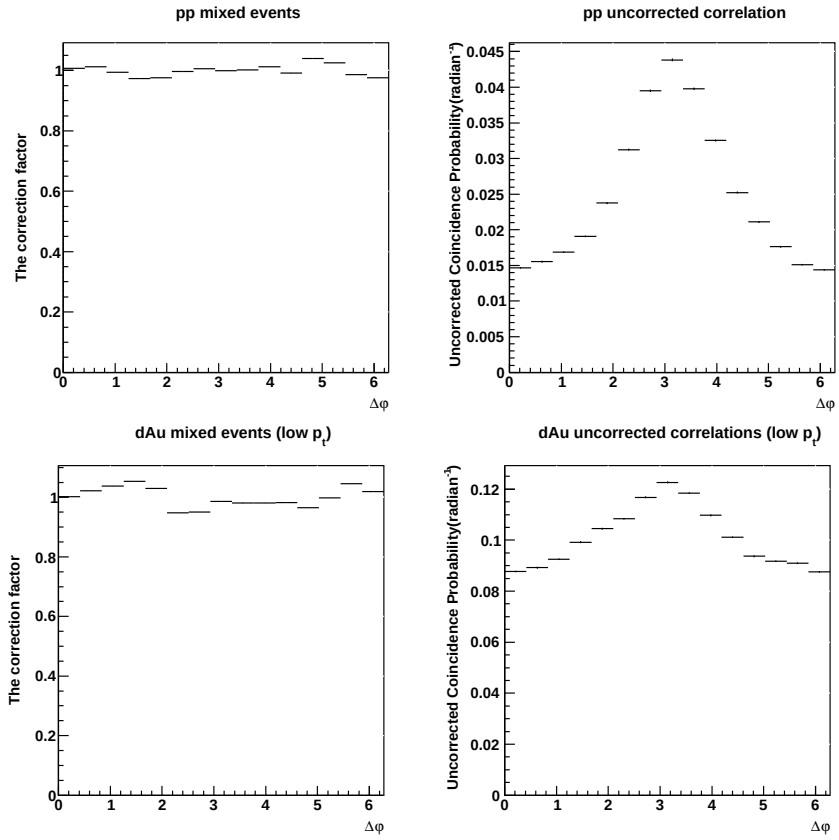

Figure 5.5: The top row: The correction factor $F_{mix}(\Delta\varphi)$ (see definition of Eq. 5.1) got from the mixed events between events contain FMS π^0 and events contain the EEMC jet-like cluster in p+p collisions is shown in the left panel. The uncorrected probability of azimuthal correlations $N_{corr}(\Delta\varphi)$ (see definition in Eq 5.2) of FMS $\pi^0 s$ ($p_t^{FMS} > 2.0 GeV/c$) and EEMC jet-like clusters ($M > 0.2 GeV/c^2$ and $1.0 GeV/c < p_t^{EEMC} < p_t^{FMS}$) is shown in the right panel. The bottom row shows the dAu results, the correction factors are shown in the left panel and the uncorrected azimuthal correlations are present in the right panel. The FMS π^0 mass spectrum is shown in Figure 4.2, and the mass spectrum of the associated EEMC jet-like clusters is shown in Figure 4.12.

The FMS π^0 in sample A and the EEMC jet-like cluster in sample B are mixed with each other to get the azimuthal angle differences $\Delta\varphi_{mix}(\equiv \varphi_{FMS} - \varphi_{EEMC})$. Then the mixed events distribution are first normalized by the total number of FMS π^0 obtained in the uncorrected FMS-EEMC azimuthal correlations. Then the mixed event azimuthal correlations are renormalized to get the the correction factor $F_{mix}(\Delta\varphi)$ for further operations, in order to achieve the integral of the distribution equals to the number of bins of the histogram.

The definition of the correction factor $F_{mix}(\Delta\varphi)$ is as follows,

$$F_{mix}(\Delta\varphi) = \frac{N_{AB}(\Delta\varphi)}{N_{A_2}(\pi^0)}, \tag{5.1}$$

where $N_{AB}(\Delta\varphi)$ is the number of events within a small correlation azimuthal angle differences $\Delta\varphi$ between the FMS π^0's and the EEMC jet-like clusters selected in different events, N_{A_2} is the average number of FMS π^0 in the average azimuthal angle value per bin $\Delta\varphi$. The uncorrected probability of azimuthal correlation $N_{corr}(\Delta\varphi)$ is,

$$N_{corr}(\Delta\varphi) = \frac{N_{AC}(\Delta\varphi)}{N_{A_1}(\pi^0)}, \tag{5.2}$$

where $N_{AC}(\Delta\varphi)$ is the number of events that have coincidence correlations of the FMS π^0s and the EEMC jet-like clusters within the same event in a certain $\Delta\varphi$ range, N_{A_1} is the total number of events containing inclusive FMS π^0s for the physical correlations multiplied by the average azimuthal angle value per bin.

The coincidence probability of the FMS π^0 - EEMC jet-like cluster per trigger ($radian^{-1}$) is defined as the uncorrected correlation $N_{corr}(\Delta\varphi)$ divided by the correction factor $F_{mix}(\Delta\varphi)$ within the same $\Delta\varphi$ region,

$$C(\Delta\varphi) \equiv \frac{N_{corr}(\Delta\varphi)}{F_{mix}(\Delta\varphi)}. \tag{5.3}$$

The correction factor $F_{mix}(\Delta\varphi)$ and the uncorrected azimuthal corrections $N_{corr}(\Delta\varphi)$ in p+p collisions and d+Au collisions are shown in Figure 5.5. $F_{mix}(\Delta\varphi)$ in d+Au collisions has larger fluctuations than in p+p collisions. This can be explained by the shape of raw φ distribution shown in Figure 5.4. The north part of the FMS is missing as a trigger detector in d+Au collisions. This is not a big effect as shown in Figure 5.5. The errors are propagated from the raw correlations to the corrected correlations accordingly.

5.1.2 The azimuthal correlations after mixed event corrections in p+p and d+Au collisions

In addition to the low p_t cut results, we applied the same mixed event algorithm but independent correction factors $F_{mix}(\Delta\varphi)$ to the high p_t cut results in p+p interactions and d+Au interactions as well. Figure 5.6 shows the FMS π^0 - EEMC jet-like cluster azimuthal correlations after mixed events corrections (low p_t cuts in the upper panel and high p_t cuts in the lower panel). The azimuthal correlations after mixed events corrections are then fitted with the same function used for the $\pi^0 - \pi^0$ correlations mentioned in Chapter 3. The form of the function is defined as following,

$$G(x) = A_0 + \frac{A_1}{\sqrt{2\pi}A_3} \times exp(-\frac{1}{2}(\frac{x - A_2}{A_3})^2). \tag{5.4}$$

$G(x)$ includes a constant plus a Gaussian function, where A_0 defined as the constant is to fit the uncorrelated pedestal underneath the correlation peak, A_1 is the integral

of the Gaussian function, A_3 is the width of the Gaussian function and A_2 is the centroid of the Gaussian function.

The fitted parameters of $G(x)$ in p+p collisions and d+Au collisions for the azimuthal correlations between the FMS π^0s with $p_t^{FMS} > 2.0 GeV/c$ and the EEMC jet-like clusters ($M > 0.2 GeV/c^2$) with $1.0 GeV/c < p_t^{EEMC} < p_t^{FMS}$ are shown in Table 5.1. The fitted results for the azimuthal correlations of the FMS π^0 with $p_t^{FMS} > 2.5 GeV/c$ and the EEMC jet-like cluster with $1.5 GeV/c < p_t^{EEMC} < p_t^{FMS}$ after the mixed event corrections are shown in Table 5.2. The errors shown in Table 5.1 and Table 5.2 are statistical errors only, the systematic studies will be discussed at the end of this chapter. The pedestal in the FMS π^0 and EEMC jet-like cluster correlations is higher in d+Au collisions than that in p+p collisions. Unlike the π^0-π^0 azimuthal correlations, the probability of finding none jet components in the EEMC for the FMS π^0 - EEMC jet-like cluster correlation is higher which leads to the high pedestal underneath the correlations. The large χ^2 is caused by the deviations from the fit function in several data points.

Although the χ^2/NDF values with function $G(x)$ are larger than 1, to be consistent with previous forward+forward correlations and forward+mid-rapidity correlation studies, the constant plus a Gaussian function form is kept to fit the coincident probability of the FMS-EEMC correlations. Systematic studies including trying a different fit function will be discussed at the end of this chapter. All the correlations after mixed event corrections have better fit quantity (see χ^2/NDF in Table 5.1 and Table 5.2) than the uncorrelated one. This indicates the mixed event corrections have successfully removed the fluctuations caused by the non-uniform detector acceptance. Lower p_t cut measurements probe larger transverse size $1/Q^2$ inside the Au nuclei than the higher p_t cuts, therefore the integral of the gluon distribution function of Au nuclei in a certain x region is larger. This results in larger width and integral of the correlations with the low p_t cuts. The width differences $\Delta\sigma = \sigma_{dAu} - \sigma_{pp}$ between p+p interactions and d+Au interactions with low p_t cuts is 0.080 ± 0.012 and the value is 0.116 ± 0.016 for high p_t cuts results. The mixed event corrections do not impact on the width differences between p+p collisions and d+Au collisions. Subsequently, the detector non-uniform effect is not the source of the width differences between p+p interactions and d+Au interactions. We will discuss this results further in the following section.

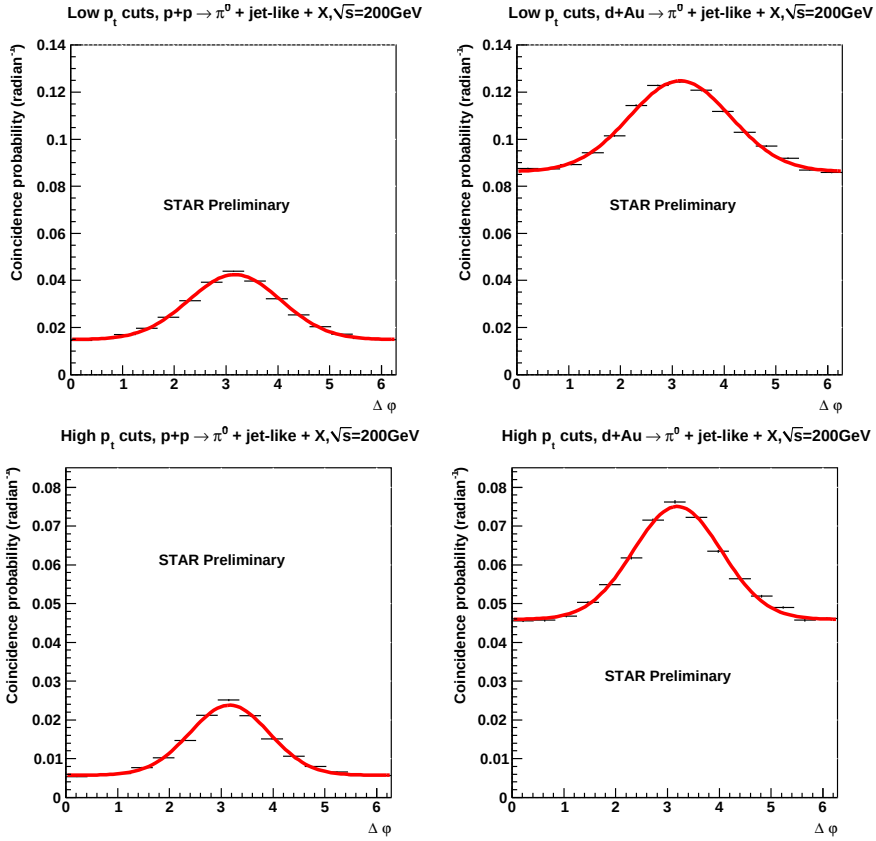

Figure 5.6: Azimuthal correlations after mixed events corrections $C(\Delta\varphi)$ (see Eq. 5.4) with different p_t cuts. The top row: The coincidence probability of azimuthal correlations of FMS $\pi^0 s$ ($p_t^{FMS} > 2.0 GeV/c$) and EEMC jet-like clusters ($M > 0.2 GeV/c^2$ and $1.0 GeV/c < p_t^{EEMC} < p_t^{FMS}$) in p+p collisions (left) and d+Au collisions (right). The bottom row: The coincidence probability of azimuthal correlations of FMS $\pi^0 s$ ($p_t^{FMS} > 2.5 GeV/c$) and EEMC jet-like clusters ($M > 0.2 GeV/c^2$ and $1.5 GeV/c < p_t^{EEMC} < p_t^{FMS}$) in p+p collisions (left) and d+Au collisions (right). Red line stands for the fitting function $G(x)$ (see definition in Eq 5.4). The fitted parameters of $G(x)$ for low p_t cuts results before and after mixed event correction are listed in Table 5.1 and the high p_t results before and after mixed event correction are listed in Table 5.2. The pedestal in d+Au collisions is much higher than p+p collisions.

	p+p uncorrected (low p_t)	p+p corrected (low p_t)
χ^2/NDF	220/11	151.4/11
Constant	0.0151 ± 0.0001	0.01516 ± 0.00007
Integral	0.06312 ± 0.00041	0.06273 ± 0.00041
Centroid	3.177 ± 0.004	3.162 ± 0.004
Width	0.9019 ± 0.0053	0.8988 ± 0.0052
	d+Au uncorrected (low p_t)	d+Au corrected (low p_t)
χ^2/NDF	250.6/11	121.8/11
Constant	0.09095 ± 0.00023	0.08881 ± 0.00022
Integral	0.08121 ± 0.00137	0.09656 ± 0.00129
Centroid	3.091 ± 0.008	3.154 ± 0.007
Width	0.9856 ± 0.0134	0.9793 ± 0.0105

Table 5.1: Comparison between uncorrected correlations fit parameters and results after removing detector acceptance effects when FMS π^0 $p_t^{FMS} > 2.0 GeV/c$ and EEMC jet-like cluster ($M > 0.2 GeV/c^2$) $1.0 GeV/c < p_t^{EEMC} < p_t^{FMS}$. See the parameter definitions in Eq.5.4. There are width differences between p+p collisions and d+Au collisions. The mixed event corrections do not impact on the width differences between p+p and d+Au interactions.

	p+p uncorrected (high p_t)	p+p corrected (high p_t)
χ^2/NDF	134.1/11	121.36/11
Constant	0.005684 ± 0.000054	0.005684 ± 0.000054
Integral	0.03472 ± 0.00034	0.03473 ± 0.00034
Centroid	3.165 ± 0.006	3.157 ± 0.006
Width	0.7694 ± 0.0074	0.7752 ± 0.0074
	d+Au uncorrected (high p_t)	d+Au corrected (high p_t)
χ^2/NDF	142.2/11	78.13/11
Constant	0.05048 ± 0.00023	0.0491 ± 0.0002
Integral	0.0605 ± 0.0013	0.07083 ± 0.00128
Centroid	3.116 ± 0.011	3.179 ± 0.010
Width	0.8733 ± 0.0167	0.8912 ± 0.0138

Table 5.2: Comparison between uncorrected correlations fit parameters and results after removing detector aceptance effects when FMS π^0 $p_t^{FMS} > 2.5 GeV/c$ and EEMC jet-like cluster ($M > 0.2 GeV/c^2$) $1.5 GeV/c < p_t^{EEMC} < p_t^{FMS}$. See the parameter definition in Eq.5.4. There are width differences between p+p collisions and d+Au collisions. The mixed event corrections do not impact on the width differences between p+p and d+Au interactions.

5.2 Underlying events analysis - background to the jet-like clusters

5.2.1 Motivation

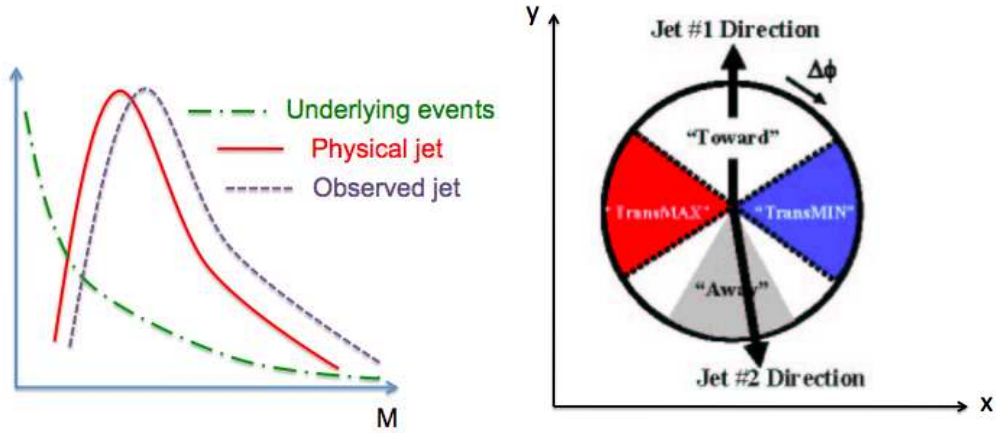

Figure 5.7: Left: schematics of underlying events smearing the physical jets to the observed jets. The green dashed dot line stands for the underlying events, the red solid line stands for physical jets and the purple dashed line stands for the observed jets. Right: schematics of the back-to-back di-jet correlations in the transverse view of collision. The back-to-back region covers $(\frac{2\pi}{3},\frac{4\pi}{3})$. The transverse region is defined as blue area plus red area. Transverse minimum region (blue area) spans $(\frac{5\pi}{6},\frac{7\pi}{6})$ and transverse maximum region (red area) spans $(\frac{4\pi}{3},\frac{5\pi}{3})$. Figure from [93].

At low x_{BJ} region, more gluons are involved in the partonic scattering due to higher gluon density. The dominant partonic scattering channels are quark+gluon (q+g) and gluon+gluon (g+g) scattering. The deposited hadron energy fragmented from the soft fragmenting partons may interfere signals from the real jets. Such contributions are called "underlying events". The underlying events are defined as everything except hard scattering partons and their radiated partons. During hadron(nuclei) - hadron(nuclei) collisions, the underlying events generally have the following components: (1)the interactions between the remnants of nuclei excluding the hard scattered parts (eg. spectator interactions), (2) initial and final non-hard scattering radiations, (3) multiple nuclei-nuclei collisions (pile-up events). These effects can not be avoided completely during collisions, and it is hard to subtract them without identified tracking of particles to isolate particles from each other. The left panel of Figure 5.7 shows the schematics of how the underlying events impact on the physical jets. The underlying events smear the physical jets to the physical jets. Not only the mass and energy of the physical jet get changed, their azimuthal angle directions may deviate from their original position. To minimize the underlying event contribution to the jet-like cluster is the goal of this study.

We use the method which was first proposed by Rick Field [93] to study the

contribution of the underlying events to the jet-like clusters (see the right panel of Figure 5.7). This method was performed in high p_t jets (eg. $p_t > 10GeV/c$). We extend the applicable scope of this method to lower p_t region (eg. the correlation analysis) assuming the underlying events are universal and can be described by the perturbative QCD (pQCD).

To see the relevant object in the initial state with the jet-like cluster reconstructed in the EEMC, a fragmenting parton is treated as a surrogate of the jet in the PYTHIA simulation. In addition to this, the same threshold bounded cluster finder is applied in the PYTHIA+GEANT and HIJING+GEANT simulation with forward π^0 filter to reconstruct jet-like clusters. Now we have three different objects within the $1.1 < \eta < 1.9$ (the same cuts used for the jet-like clusters in p+p and d+Au data) range in events triggered by the forward π^0 ($2.5 < \eta < 4.0$),

- the fragmenting partons in PYTHIA only simulation in p+p collision,
- the reconstructed jet-like clusters in PYTHIA+GEANT simulation for p+p collision and HIJING+GEANT simulation for d+Au collision,
- the reconstructed jet-like clusters in data of both p+p and d+Au interactions.

The fragmenting partons are not studied in the HIJING only simulation as there are more statistics of the π^0 triggered events in the PYTHIA only simulation. As shown in Figure 5.8, the azimuthal angle of the π^0 reconstructed in the FMS with a certain p_t cut (e.g. $p_t^{FMS} > 2.0GeV/c$) is named as φ_{FMS}. The azimuthal (polar) angle of the jet-like cluster or a fragmenting parton with the relevant p_t cut (eg. $1.0GeV/c < p_t^{EEMC} < p_t^{FMS}$) and within the EEMC acceptance ($1.1 < \eta < 1.9$) is defined as φ_{back} (θ_{back}). The pseudo-rapidity value of the jet-like cluster or parton is defined as $\eta_{back} = -lntan(\theta_{back}/2)$. The azimuthal (polar) angle of the remaining jet-like clusters or partons with transverse momentum less than the transverse momentum of the FMS π^0 ($p_t^{remain} < p_t^{FMS}$) and within the same pseudo-rapidity range is defined as φ_{remain} (θ_{remain}) and the η is defined as $\eta_{remain} = -lntan(\theta_{remain}/2)$. We take the low p_t cuts sample as an example. The azimuthal angle differences between the FMS π^0 with $p_t^{FMS} > 2.0GeV/c$ and the EEMC jet-like clusters ($mass > 0.2GeV/c^2$) or partons with $1.0GeV/c < p_t^{EEMC} < p_t^{FMS}$ is defined as,

$$\Delta\varphi_{12} = \varphi_{back} - \varphi_{FMS}. \tag{5.5}$$

The azimuthal angle difference between the FMS π^0 with $p_t^{FMS} > 2.0GeV/c$ and the remaining jet-like clusters (no mass cut) or partons with $p_t^{remain} < p_t^{FMS}$ within the EEMC acceptance is defined as,

$$\Delta\varphi_{13} = \varphi_{remain} - \varphi_{FMS}. \tag{5.6}$$

In events containing at least a pair of a FMS π^0 and a EEMC jet-like cluster satisfying the relevant p_t cuts, the relative azimuthal angle between the EEMC jet-like clusters ($mass > 0.2GeV/c^2$) or partons with $1.0GeV/c < p_t^{EEMC} < p_t^{FMS}$ and the

remaining EEMC jet-like clusters (no mass cut) or partons with $p_t^{remain} < p_t^{FMS}$ is defined as,

$$\Delta\varphi_{23} = \varphi_{remain} - \varphi_{back}. \tag{5.7}$$

All the azimuthal angle differences $\Delta\varphi_{12}$, $\Delta\varphi_{13}$ and $\Delta\varphi_{23}$ are forced to be cyclic on the interval from 0 to 2π. The relative η value between the back-to-back EEMC jet-like clusters or partons ($1.0GeV/c < p_t^{EEMC} < p_t^{FMS}$ and the cut $mass > 0.2GeV/c^2$ is only applied on the jet-like clusters) and remaining EEMC jet-like clusters or partons ($p_t^{remain} < p_t^{FMS}$, no mass cut) is,

$$\Delta\eta_{23} = \eta_{remain} - \eta_{back}. \tag{5.8}$$

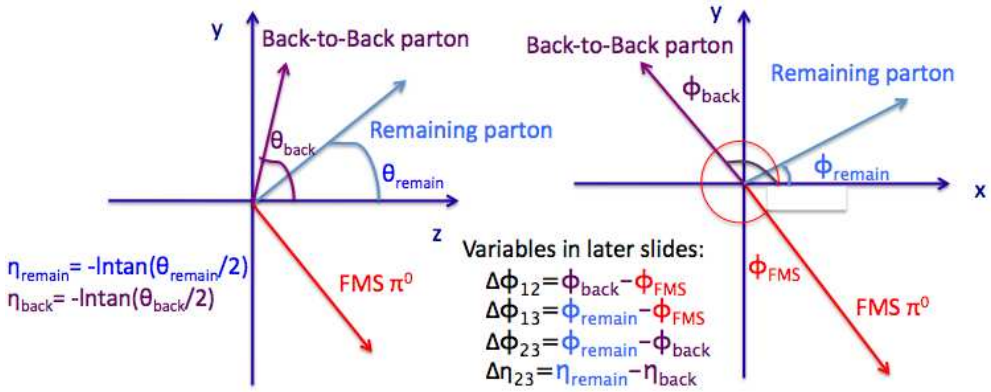

Figure 5.8: Schematics of FMS π^0 ($2.5 < \eta < 4.0$), back-to-back jet-like cluster or parton and remaining jet-like clusters or partons within the EEMC η range ($1.1 < \eta < 1.9$) in yz plane view is shown in the left and the xy plane view is shown in the right. The FMS π^0 azimuthal angle is defined as φ_{FMS}, the back-to-back jet-like cluster or parton azimuthal (polar) angle is defined as φ_{back} (θ_{back}) and the azimuthal (polar) angle of the remaining jet-like cluster or parton is defined as φ_{remain} (θ_{remain}). The pseudo-rapidity of the back-to-back (remaining) parton is defined as $\eta_{back} = -lntan(\theta_{back}/2)$ ($\eta_{remain} = -lntan(\theta_{remain}/2)$). Relevant variables $\Delta\varphi_{12}$ (see Eq.5.5), $\Delta\varphi_{13}$ (see Eq.5.6), $\Delta\varphi_{23}$ (see Eq.5.7), $\Delta\eta_{23}$ (see Eq.5.8) are defined. The azimuthal angle differences are forced to be cyclic on the interval from 0 to 2π.

A FMS π^0 satisfing the certain p_t cut is treated as a leading jet. If there is one jet-like cluster or parton within the EEMC acceptance ($1.1 < \eta < 1.9$) and the relevant p_t cuts sitting in the back-to-back region with $\Delta\varphi_{12}$ in $(\frac{5\pi}{6}, \frac{7\pi}{6})$, we take the π^0 (reconstructed in the FMS) and jet-like cluster (reconstructed in the EEMC) as a back-to-back pair. Moreover, in the events containing at least one back-to-back pair, the remaining jet-like clusters or partons ($1.1 < \eta < 1.9$, the same η range of the back-to-back jet-like clusters or partons) in the transverse region $\Delta\varphi_{13}$ in $(\frac{\pi}{3}, \frac{2\pi}{3})$ and $\Delta\varphi_{13}$ in $(\frac{4\pi}{3}, \frac{5\pi}{3})$ are used for underlying events candidates.

5.2.2 Data and simulation comparison

The underlying event study starts with partons recorded in PYTHIA simulation for p+p collision. Fragmenting partons like u, d, s quarks, relative anti-quarks and gluons in PYTHIA only simulation are taken as jet surrogates. A π^0 is chosen as a FMS π^0 only when both its photon daughters are projected in the FMS acceptance. In PYTHIA simulated p+p collision events, only those that contain higher transverse momentum FMS π^0 than the fragmenting partons with the EEMC η coverage are studied. This cut is to emphasize the underlying event contribution. The fragmenting parton in the FMS π^0 back-to-back region is marked as "back-to-back parton". As there are p_t cuts to the di-jets in Figure 5.7, to be consistent with Rick Field's method and to get highest statistics in simulation, low p_t cut defined as the FMS π^0 $p_t^{FMS} > 2.0GeV/c$ and back-to-back parton with $1.0GeV/c < p_t^{EEMC} < p_t^{FMS}$ are applied. When we found a back-to-back pair, the remaining partons within the EEMC coverage in the transverse region ("transverse parton") with $p_t^{remain} < p_t^{FMS}$ are taken as underlying event objects, assuming the underlying events distribute uniformly in the full azimuthal angle φ range.

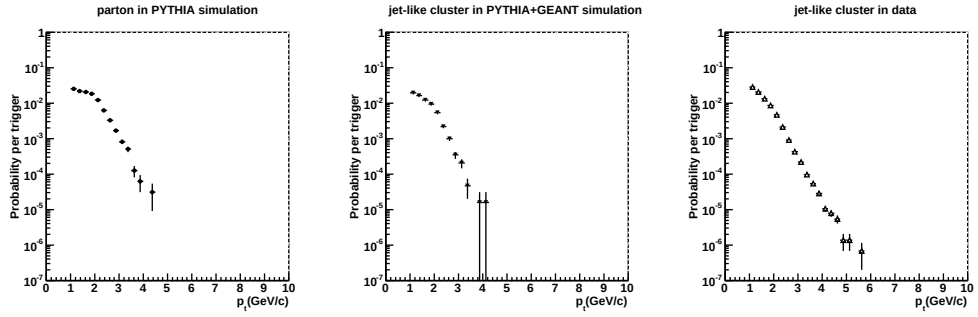

Figure 5.9: The p_t spectrum of the EEMC partons or jet-like clusters within the triggered FMS π^0 back-to-back region $\frac{5\pi}{6} < \Delta\varphi_{12} < \frac{7\pi}{6}$ (see $\Delta\varphi_{12}$ in Eq 5.5) in p+p collisions. In events containing a FMS π^0 with $p_t^{FMS} > 2.0GeV/c$, the back-to-back partons or jet-like clusters ($mass > 0.2GeV/c^2$) with $1.0GeV/c < p_t^{EEMC} < p_t^{FMS}$ are presented. Results based on parton level in PYTHIA only simulation are shown in the left panel, results based on reconstructed jet-like clusters in PTHIA+GEANT simulation are shown in the middle panel and the results based on reconstructed jet-like clusters in p+p collision data are shown in the right panel. The parton-level distribution, the jet-like cluster from full simulation and the jet-like cluster in data look similar especially the slopes in these distribution are in resonable agreement for $p_t > 2.0GeV/c$ region.

Before we look further to compare the property like the invariant mass between the "back-to-back parton" and the "transverse parton", the relative spatial distances in $\eta - \varphi$ plane between the back-to-back partons with p_t cuts and the remaining partons are studied to understand the relationship between them. For the remaining parton, there is $p_t^{remain} < p_t^{FMS}$ cut applied. The azimuthal angle differences $\Delta\varphi_{23}$

versus the pseudo-rapidity differences $\Delta\eta_{23}$ between the back-to-back parton specified in the EEMC range $1.1 < \eta < 1.9$ with $1.0GeV/c < p_t^{EEMC} < p_t^{FMS}$ and the remaining parton with the same EEMC coverage η cuts has a clear ring structure. This is related with radiated gluons from the back-to-back partons. The ring shape is more obvious when removing the η coverage cuts for the remaining partons. This inflects that the η cut has detector acceptance limitation, but it does not affect the measured gluon radiation effect. In the PYTHIA+GEANT simulation for p+p collisions, the simulated collision events contain particles passing through the EEMC and their deposited energies can be simulated with GEANT. The jet-like clusters reconstructed in the EEMC with cone radius $R = 0.6$ cluster finder in PYTHIA+GEANT are studied to compare with data. The energy threshold on the EEMC towers is selected to be the same as data (250MeV). The FMS π^0 in the PYTHIA+GEANT full simulation is based on the same strategy as used in PYTHIA only simulation. In the FMS π^0 ($p_t^{FMS} > 2.0GeV/c$) triggered events, the reconstructed jet-like cluster in the EEMC with $mass > 0.2GeV/c^2$ and $1.0GeV/c < p_t^{EEMC} < p_t^{FMS}$ within $\frac{5\pi}{6} < \Delta\varphi_{12} < \frac{7\pi}{6}$ is taken as the back-to-back jet-like cluster. In addition to the back-to-back jet-like cluster, the remaining jet-like clusters in the EEMC with $p_t < p_t^{FMS}$ cuts and no mass cuts within $\frac{\pi}{3} < \Delta\varphi_{12} < \frac{2\pi}{3}$ plus $\frac{4\pi}{3} < \Delta\varphi_{12} < \frac{5\pi}{3}$ region are named as transverse jet-like clusters and taken as the underlying event proxies. Similar studies are performed in p+p data as well. The mass, energy and p_t of the back-to-back partons or jet-like clusters and transverse partons or jet-like clusters are compared separately in PYTHIA only simulation, PYTHIA+GEANT simulation and data.

Figure 5.9 shows the p_t spectrum of the back-to-back partons in PYTHIA only simulation (left panel), the jet-like clusters in PYTHIA+GEANT full simulation (middle panel) and the jet-like clusters in data (right panel) for p+p collisions. All of the distributions are normalized by the number of the triggered π^0's reconstructed in the FMS to get the probability per trigger particle. The back-to-back parton spectrum generally agrees with the jet-like cluster results in full simulation and finally with the jet-like cluster reconstructed in data. The agreement between fragmenting parton and jet-like cluster indicates the jet-like cluster is a reasonable object to probe initial state function.

5.2.3 Underlying event contribution to the jet-like clusters

As there is no tracking system covering the η range of the EEMC during RHIC run8, any cuts tried to remove underlying events may introduce biases or over-subtraction. An indirect path to study the contributions from underlying events to the jet-like clusters in data is performed. From the data and simulation comparison in previous subsection, the remaining super clusters are proved to be good surrogates as underlying events and the underlying events are assumed to have uniform distribution.

Figure 5.10 shows the invariant masses of the EEMC jet-like clusters ($mass > 0.2GeV/c^2$, $1.0GeV/c < p_t^{EEMC} < p_t^{FMS}$) in the FMS π^0 ($p_t^{FMS} > 2.0GeV/c$) back-to-back region and the remaining jet-like clusters ($p_t^{EEMC} < p_t^{FMS}$) in the transverse

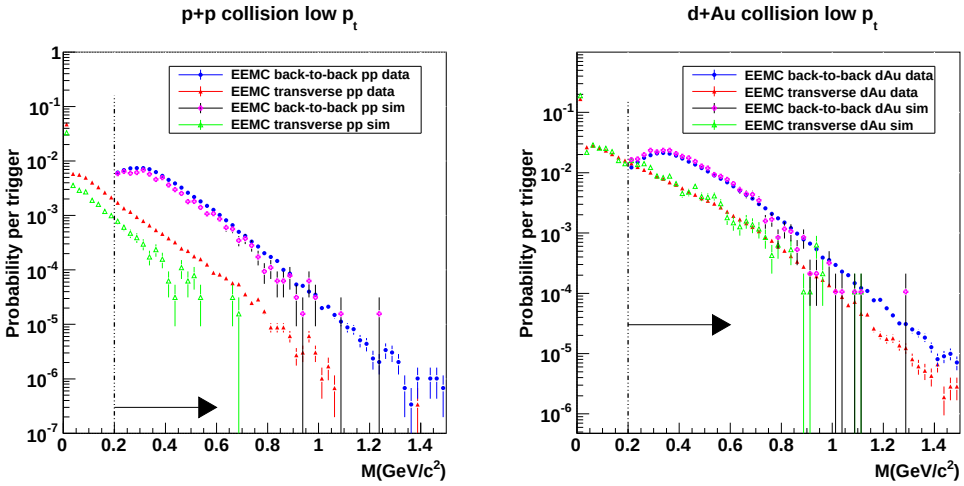

Figure 5.10: Data and simulation comparisons for the invariant mass of the "back-to-back" jet-like clusters ($mass > 0.2GeV/c^2$, $1.0GeV/c < p_t^{EEMC} < p_t^{FMS}$) within $\frac{5\pi}{6} < \Delta\varphi_{12} < \frac{7\pi}{6}$ (see $\Delta\varphi_{12}$ in Eq 5.5) and the remaining "transverse" jet-like clusters ($p_t^{remain} < p_t^{FMS}$) within $\frac{\pi}{3} < \Delta\varphi_{12} < \frac{2\pi}{3}$ plus $\frac{4\pi}{3} < \Delta\varphi_{12} < \frac{5\pi}{3}$ region in the FMS π^0 ($p_t^{FMS} > 2.0GeV/c$) triggered events. The tower energy threshold of the EEMC is chosen as 250MeV. The probabilities per trigger particle in p+p collisions are shown in the left panel and the results in d+Au collisions are shown in the right panel. Blue solid circles stand for the back-to-back jet-like clusters in data, red solid triangles stand for the remaining transverse jet-like clusters in data, purple open cross points stand for the back-to-back jet-like clusters in simulation and green open triangles stand for the remaining transverse jet-like clusters in simulation. There are more underlying event contribution to the jet-like clusters in d+Au collisions than p+p collisions.

region relative to the FMS π^0 in both data and simulation. The distributions are normalized by the number of the triggered FMS π^0's. The mass spectrum within p+p data is higher than simulation, which is due to the higher tower multiplicity in data than simulation for p+p interactions. There are better agreement between data and simulation in d+Au collisions. The jet-like clusters in the transverse region are taken as surrogates of underlying events. A ratio $R_{threshold}$ is defined as integral of number of remaining jet-like clusters with $p_t < p_t^{FMS}$) per FMS π^0 trigger above $0.2GeV/c^2$ mass cut over the number of jet-like $1.0GeV/c < p_t^{EEMC} < p_t^{FMS}$ per FMS π^0 trigger above $0.2GeV/c^2$ mass cut,

$$R_{threshold} = \frac{\int_{0.2GeV/c^2}^{\infty} dN/dM_{underly}}{\int_{0.2GeV/c^2}^{\infty} dN/dM_{jet}}, \tag{5.9}$$

where $\int_{0.2GeV/c^2}^{\infty} dN/dM_{underly}$ is the integral of the probability per trigger particle for $mass > 0.2GeV/c^2$ underlying events and $\int_{0.2GeV/c^2}^{\infty} dN/dM_{jet}$ is the integral of the probability per trigger particle for $mass > 0.2GeV/c^2$ jet-like clusters. We use $R_{threshold}$ as the fraction of underlying event in the jet-like clusters. The underlying event does not occupy a large fraction of the EEMC jet-like clusters in p+p collisions. There are more underlying event contribution to the EEMC jet-like clusters in d+Au collisions than p+p collisions as shown in Figure 5.10. A series of studies are performed to suppress the contributions from the underlying events to the jet-like clusters. These studies will be discussed in the following sections.

5.2.4 Tower energy threshold dependence

The hadronic shower can not be fully measured via the electromagnetic shower in the electromagnetic calorimeter. With the increased tower threshold in the EEMC, the fraction of hadronic energy in the EEMC can be reduced. Therefore, the contribution of underlying events can be tuned by changing the tower energy threshold as the underlying events are soft physics such as beam remnants. This can be reflected in the distribution of $R_{threshold}$ versus tower energy threshold. In addition to $R_{threshold}$ which is related with the fraction of underlying event inside the jet-like clusters, the other parameters of the fitting function $G(x)$ (see definition in Eq 5.4) for the azimuthal correlations are relevant to understand the impacts of tower energy threshold.

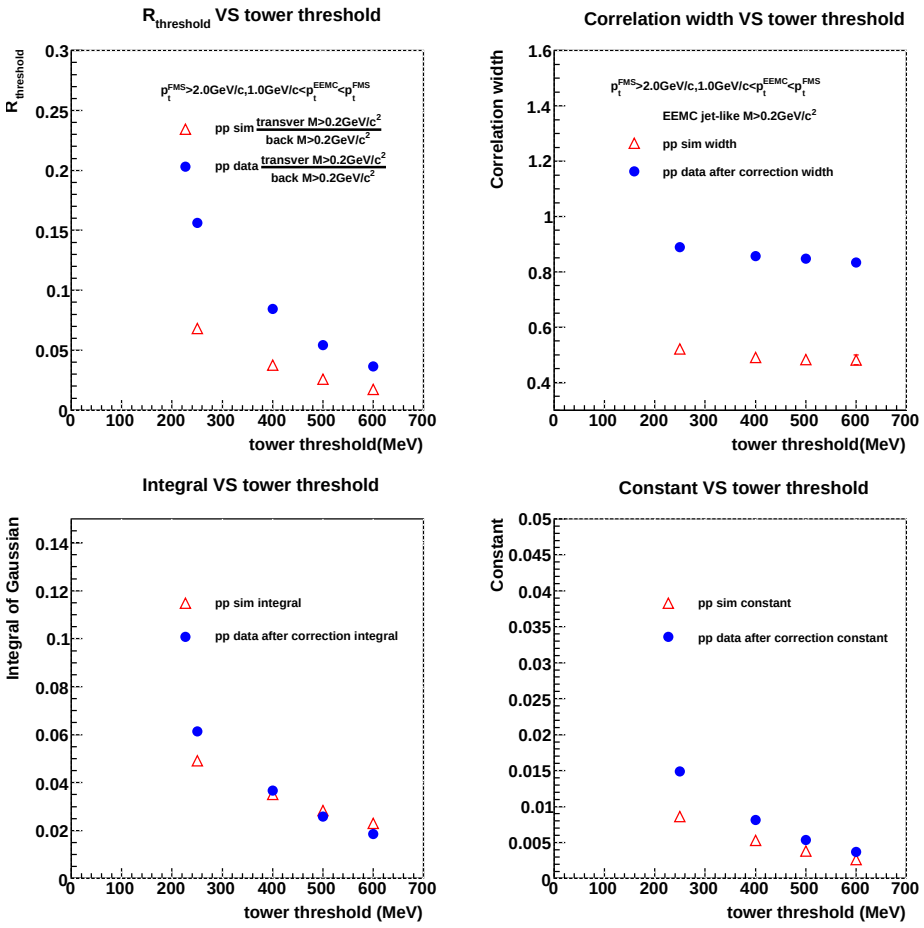

Figure 5.11: Data and simulation comparison for $R_{threshold}$ (see definition in Eq 5.9) and parameters of fitting function G(x) (see definition in Eq 5.4) for azimuthal correlations of the FMS π^0s ($p_t^{FMS} > 2.0GeV/c$) and the EEMC jet-like clusters ($mass > 0.2GeV/c^2$ and $1.0GeV/c < p_t^{EEMC} < p_t^{FMS}$) with different EEMC tower energy threshold in p+p interactions. Left top panel shows the study for $R_{threshold}$, the right top panel shows the study for width of correlation, left bottom panel shows the study for the integral of Gaussian function and the right bottom panel shows the study for the constant values. Blue solid circles stand for data and red open triangles stand for simulation.

5.2. Underlying events analysis - background to the jet-like clusters

Figure 5.11 shows the comparison between data and simulation in p+p collisions for tower energy threshold dependence on the $R_{threshold}$, the width of correlation, the integral of the Gaussian function and constant for azimuthal correlation with "low p_t" cut. The tower energy thresholds are selected from 250MeV, 400MeV, 500MeV to 600MeV. As the detector acceptance in simulation is ideally uniform, the results after mixed event corrections in data are used to compare with simulation. Differences between data and simulation is due to the differences in EEMC tower multiplicity between data and simulation (see Figure 4.4). Although d+Au data have better agreement with simulation in EEMC tower multiplicity, the low statistics in d+Au simulation can not undertake such comparison. Therefore only p+p comparison is shown in Figure 5.11. The differences between data and simulation in $R_{threshold}$, the integral of fitting Gaussian function and the constant of the correlations decreases as the tower threshold increases. Higher tower threshold not only reduce the fraction of underlying events in the jet-like clusters but also the hadronic component of the deposited energy in the EEMC.

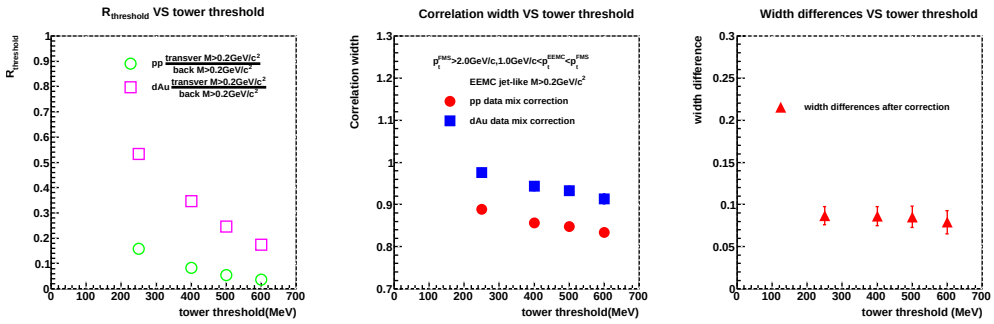

Figure 5.12: The FMS π^0 and EEMC jet-like cluster correlations with low p_t cuts as a function of tower energy threshold in both p+p and d+Au collisions. The tower energy thresholds are selected from 250MeV, 400MeV, 500MeV to 600MeV. Left panel shows the study for $R_{threshold}$ (see definition in Eq 5.9), the green open circles stand for p+p collisions and the purple open rectangles stand for d+Au collisions. The widths of azimuthal correlations after mixed events corrections are shown in the middle panel, red solid circles stand for p+p collisions and blue solid rectangles stand for d+Au collisions. The width differences between p+p interactions and d+Au interactions are shown in the right panel, and they do not change much as the EEMC tower threshold increases.

The differences for $R_{threshold}$ as a function of tower energy threshold between p+p collisions and d+Au collisions in data are shown in the left panel of Figure 5.12. The underlying event contribution to the jet-like clusters $R_{threshold}$ are higher in d+Au interactions than in p+p interactions. $R_{threshold}$ decreases as tower energy threshold increases, and the values in d+Au interactions are approaching the values in p+p interactions. From the middle panel and the right panel of Figure 5.12, the widths of azimuthal correlations in both p+p interactions and d+Au interactions decrease as the tower energy threshold increases, while the width differences

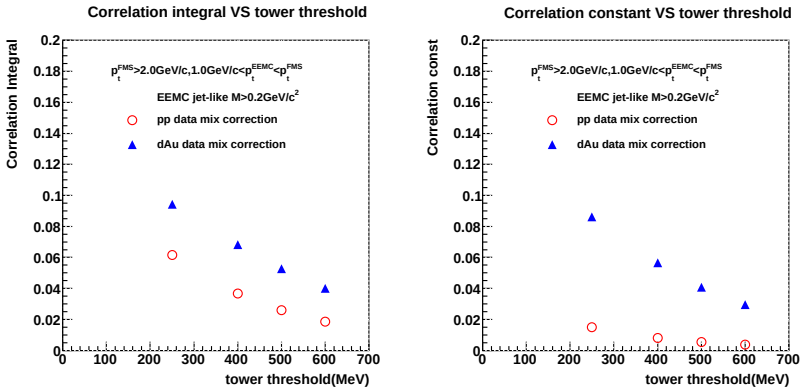

Figure 5.13: The fitted integral and constant parameters of G(x) function (see definition in Eq 5.4) for the FMS π^0 - EEMC jet-like cluster correlations with low p_t cuts as a function of tower energy threshold in both p+p and d+Au collisions. The integral values are shown in the left panel and the constant values are shown in the right panel. Red open circles stand for p+p collisions and blue solid triangles stand for d+Au collisions.

between p+p collisions and d+Au collisions remain nearly the same independent of tower threshold. This indicates that there is negligible impact from underlying events to the broadening effects from p+p to d+Au collisions in the FMS π^0 - EEMC jet-like cluster correlations. The underlying events contribution which can be tuned by changing the tower energy threshold is mostly related with the pedestal of the azimuthal correlations. This study indicates that the underlying event can be suppressed with a high tower threshold.

Integral of the Gaussian function and the constant scales also have tower threshold dependence. The left panel of Figure 5.13 shows the integral of the fitting Gaussian function in G(x) for the azimuthal correlations between FMS π^0 $p_t^{FMS} > 2.0 GeV/c$ and EEMC jet-like cluster ($M > 0.2 GeV/c^2$) $1.0 GeV/c < p_t^{EEMC} < p_t^{FMS}$ as a function of tower energy threshold. The results are after mixed event corrections. The integral decrease almost equally in p+p collisions and d+Au collisions as tower threshold increases.The differences between p+p interactions and d+Au interactions remain the same. The right panel of Figure 5.13 shows the constant of the fitting function G(x) for the correlations versus the tower energy threshold. The integral of the correlation peak and the constant values decrease as tower threshold increases in both p+p and d+Au collisions, but the constant values in d+Au collisions decreases more rapidly than that in p+p collisions. In other words, the constant values in d+Au collisions are approaching to the p+p collision results as the tower threshold increases.

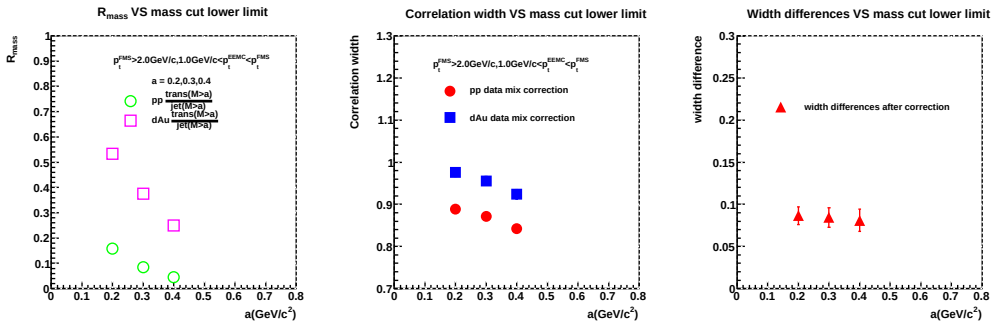

Figure 5.14: The FMS π^0 and EEMC jet-like cluster correlations with low p_t cuts as a function of jet-like cluster mass cut lower limit in both p+p and d+Au collisions. The mass cut lower limits are selected from $0.2GeV/c^2$, $0.3GeV/c^2$ to $0.4GeV/c^2$. Left panel shows the study for R_{mass} (see definition in Eq 5.10), the green open circles stand for p+p collisions and the purple open rectangles stand for d+Au collisions. The widths of azimuthal correlations after mixed events corrections are shown in the middle panel, red solid circles stand for p+p collisions and blue solid rectangles stand for d+Au collisions. The width differences between p+p interactions and d+Au interactions are shown in the right panel.

5.2.5 Jet-like cluster mass cut dependence

In addition to the tower threshold, Figure 5.10 indicates different mass cuts can also change the fractions of underlying events. As in Eq 5.9, the fraction of underlying events with different mass cuts are defined as,

$$R_{mass} = \frac{\int_a^\infty dN/dM_{underly}}{\int_a^\infty dN/dM_{jet}}, \tag{5.10}$$

where $a = 0.2GeV/c^2$, $0.3GeV/c^2$ and $0.4GeV/c^2$ is the lower limit of the mass cut, $\int_a^\infty dN/dM_{underly}$ is the integral of the probability per trigger particle for $mass > a$ underlying events and $\int_a^\infty dN/dM_{jet}$ is the integral of the probability per trigger particle for $mass > a$ jet-like clusters. The left panel of Figure 5.14 shows R_{mass} as a function of lower limits of mass cuts a. R_{mass} decreases as mass cut a increases and the number in d+Au collisions is approaching the same scale as in p+p collisions. The widthes of azimuthal correlations in p+p interactions and d+Au interactions are shown in the middle panel and the width differences between p+p and d+Au interactions are shown in the right panel. Although the correlation width decreases as the mass cut lower limits increases, the width differences between p+p interactions and d+Au interactions are independent of mass cuts.

5.3 Forward+near-forward correlation results

As the underlying events contribution can be suppressed by increasing the tower threshold in the EEMC and the mass cut lower limit for the jet-like cluster, the tower threshold is selected to be 600MeV and the mass lower limit is taken as $0.4GeV/c^2$. One can fit the $R_{threshold}$ distribution in Figure 5.12 or the R_{mass} distribution in Figure 5.14 with a decay exponential function then derive the expected tower threshold to suppress the underlying event to a low fraction (eg. 0.001). However, the tower threshold (1.4GeV for p+p collisions and 2.7GeV for d+Au collisions) is very high compared to the p_t cuts for the jet-like clusters, this will limit the statistics of the reconstructed jet-like clusters. As a trade off, we use the 600MeV tower threshold and $mass > 0.4GeV/c^2$ cuts for the EEMC jet-like clusters to achieve the final results. Figure 5.15 shows the FMS π^0 - EEMC jet-like cluster azimuthal correlations with low p_t cuts (the FMS π^0 $p_t^{FMS} > 2.0GeV/c$ and the EEMC jet-like cluster $1.0GeV/c < p_t^{EEMC} < p_t^{FMS}$) in the top panel and high p_t cuts (the FMS π^0 $p_t^{FMS} > 2.5GeV/c$ and the EEMC jet-like cluster $1.5GeV/c < p_t^{EEMC} < p_t^{FMS}$) in the bottom panel. The correlation results are fitted with a constant plus a Gaussian function G(x) (see definition in Eq 5.4), and the fitted parameters are listed in Table 5.3.

The ratio of the correlation peak integral over the pedestal is about 6 (16) for the correlation with low p_t cuts in p+p (d+Au) collisions, and the ratio for high p_t cut results is around 8 (18) in p+p (d+Au) collisions. The high correlation peak to pedestal ratio indicates the current cuts have successfully suppressed the underlying event contribution to the jet-like clusters. The width differences from p+p interaction to d+Au interaction $\Delta\sigma(dAu - pp)$ are 0.0957 ± 0.0200 with low p_t cuts and 0.1295 ± 0.0229 with high p_t cuts. There are around 5σ (6σ) significance broadening from p+p collision to d+Au collisions for the FMS π^0 - EEMC jet-like cluster azimuthal correlation with low (high) p_t cuts. This means the probed gluon distribution function in the x_{BJ} region between 0.003 and 0.02 is higher than the region $0.008 < x_{BJ} < 0.07$ probed by the forward+mid-rapidity correlations (eg. FMS-BEMC azimuthal correlations).

	p+p corrected (low p_t)	d+Au corrected (low p_t)
χ^2/NDF	75.08/11	49.96/11
Constant	0.0008021 ± 0.0000125	0.009757 ± 0.000056
Integral	0.005025 ± 0.000079	0.01589 ± 0.00032
Centroid	3.141 ± 0.010	3.157 ± 0.011
Width	0.7978 ± 0.0124	0.8935 ± 0.0157
	p+p corrected (high p_t)	d+Au corrected (high p_t)
χ^2/NDF	70.32/11	49.42/11
Constant	0.0007415 ± 0.000017	0.009404 ± 0.000073
Integral	0.005949 ± 0.000112	0.01764 ± 0.00042
Centroid	3.136 ± 0.012	3.156 ± 0.014
Width	0.7154 ± 0.0143	0.8449 ± 0.0179

Table 5.3: Comparisons for the fit parameters of the coincident probability of the FMS π^0 and EEMC jet-like cluster ($M > 0.4GeV/c^2$) in Figure 5.15 between p+p interactions and d+Au interactions. See the parameter definitions in Eq.5.4. Low p_t means the FMS π^0 $p_t^{FMS} > 2.0GeV/c$ and the EEMC jet-like cluster $1.0GeV/c < p_t^{EEMC} < p_t^{FMS}$. High p_t means the FMS π^0 $p_t^{FMS} > 2.5GeV/c$ and the EEMC jet-like cluster $1.5GeV/c < p_t^{EEMC} < p_t^{FMS}$. After the underlying event suppression, significant width differences between p+p collisions and d+Au collisions are kept with statistical error only.

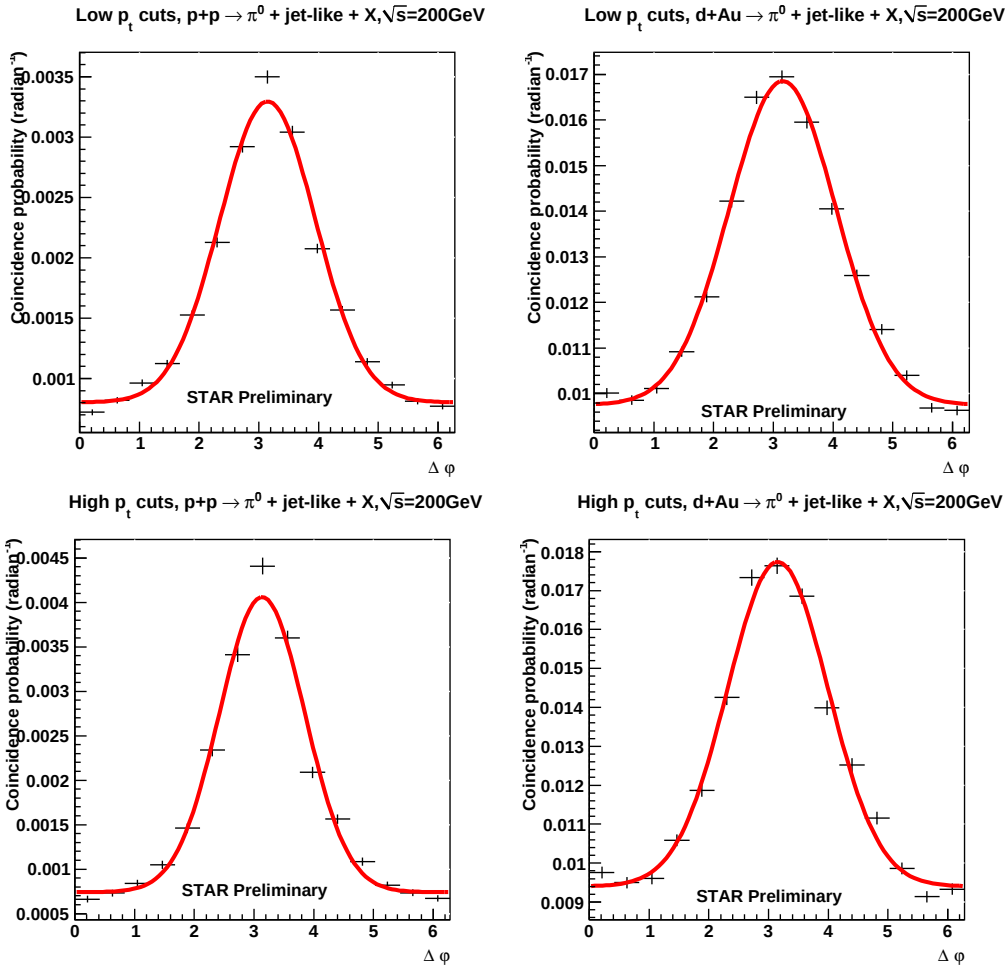

Figure 5.15: The coincidence probability of the FMS π^0 and EEMC jet-like cluster ($mass > 0.4GeV/c^2$) azimuthal correlations in p+p collisions and d+Au collisions. FMS π^0 $p_t^{FMS} > 2.0GeV/c$ and EEMC jet-like cluster $1.0GeV/c < p_t^{EEMC} < p_t^{FMS}$ (low p_t) cuts are applied in the top panel, and FMS π^0 $p_t^{FMS} > 2.5GeV/c$ and EEMC jet-like cluster $1.5GeV/c < p_t^{EEMC} < p_t^{FMS}$ (high p_t) cuts are applied in the bottom panel. The data points are fit with function G(x) (see definition in Eq 5.4) which is represented by the red solid line, and the fitted parameters are listed in Table 5.3.

5.3.1 Systematic uncertainties

There are several sources of systematic uncertainties on the FMS-EEMC correlations. These include jet-like reconstruction algorithm, reconstruction cuts and different background contributions. The integral of the Gaussian function extracts the correlation yields per trigger and we take this parameter to do a series of systematic checks. The high energy experiment studies provide a mean for underlying event suppression [93]. With the 600MeV threshold for the EEMC towers, the yield (the integral of the correlation peak) after mixed event correction in p+p (and d+Au) interaction with low p_t cuts (FMS π^0 $p_t^{FMS} > 2.0GeV/c$ and EEMC jet-like cluster with $mass > 0.4GeV/c^2$ and $1.0GeV/c < p_t^{EEMC} < p_t^{FMS}$) is $I_{pp} = 0.005025 \pm 0.000079$ ($I_{dAu} = 0.01589 \pm 0.00032$), and the value with high p_t cuts (FMS π^0 $p_t^{FMS} > 2.5GeV/c$ and EEMC jet-like cluster with $mass > 0.4GeV/c^2$ and $1.5GeV/c < p_t^{EEMC} < p_t^{FMS}$) is $I_{pp} = 0.005949 \pm 0.000112$ ($I_{dAu} = 0.01764 \pm 0.00042$). The impacts on the Gaussian peak from different selections are systematically studied in the following.

a. Correlation bin selections Different bin sets of the azimuthal correlations may induce different fit quality, the standard number of bins we used is 15. The number of bins is scanned from 10, 12, 14, 15, 16 to 20. The fitted integral of the Gaussian peak for 14 bins (a1) and 16 bins (a2) which are with better fit agreement are put in Table 5.4.

b. Run selections The criteria on run selection may induce systematic uncertainties. And we vary the cuts by 10% and check the results after mixed event corrections (Item b in Table 5.4).

c. Integral of Gaussian peak in simulation We have studied reconstructed EEMC jet-like clusters in PYTHIA (HIJING) + GEANT simulation for p+p (d+Au) collisions. The azimuthal correlations between FMS π^0 and the EEMC jet-like cluster are analogously fit with $G(x)$ (see definition in Eq 5.4) and the fitted Gaussian integral values are put in Table 5.4. As the simulation samples in p+p interactions used in this analysis have discrepancy in describe EEMC tower multiplicities from real data, the differences between data and simulation for p+p collisions are included in the systematic studies. The integral of the correlation peak is more sensitive to the detector acceptance effect.

d. Fit function selection The fit function $G(x)$ includes a constant plus a Gaussian function. The back-to-back correlation results from data do not like a pure Gaussian sits on the uncorrelated pedestal, the top of the correlation is away from the fit function $G(x)$ (the main source of large χ^2). To check the impacts from different fit functions, a new fit function $P(x)$ which contains a constant plus two Gaussian function is applied on the correlation after mixed event corrections. $P(x)$ is defined as follows,

$$P(x) = A_0 + \frac{A_1}{\sqrt{2\pi}A_2} \times exp(-\frac{1}{2}(\frac{x-\pi}{A_2})^2) + \frac{A_3}{\sqrt{2\pi}A_4} \times exp(-\frac{1}{2}(\frac{x-\pi}{A_4})^2), \quad (5.11)$$

Item	Integral in pp I_{pp} (low p_t)	Integral in dAu I_{dAu} (low p_t)
standard	0.005025±0.000079	0.01589±0.00032
a1	0.005022±0.000080	0.01357±0.00038
a2	0.005014±0.000079	0.01373±0.00038
b	0.005017±0.000084	0.01684±0.00040
c	0.006860±0.00037	no
d	0.005556±0.00055	0.01650±0.00175
e	0.006238±0.000114	0.01870±0.00075
systemactic error	+ 0.00183 - 0.00001	+0. 00281 -0. 00216
Item	Integral in pp I_{pp} (high p_t)	Integral in dAu I_{dAu} (high p_t)
standard	0.005949±0.000112	0.01764±0.00042
a1	0.005951±0.000112	0.01539±0.00046
a2	0.005937±0.000112	0.01562±0.00047
b	0.005969±0.000120	0.01864±0.00052
c	0.00905±0.000738	no
d	0.006511±0.000572	0.01825±0.000221
e	0.006227±0.000114	0.01878±0.00042
systematic error	+ 0.00310 - 0.00001	+0. 00114 -0. 00225

Table 5.4: Summary of the systematic uncertainty analysis for the extraction of the correlated yield in p+p and d+Au interactions for lower (top table) and higher (bottom table) p_T selections. "Standard" is the coincidence probability of FMS π^0 and EEMC jet-like cluster with the tower energy threshold 600MeV and $0.4GeV/c^2$ mass lower limit for the reconstructed jet-like cluster in the EEMC. The definition of other item are described in text.

where the integral of correlation peak is $A_1 + A_3$ (item d).

e. Mass cut for the EEMC jet-like cluster From previous sections, the width differences from p+p collisions to d+Au collisions do not rely on the mass cuts on the EEMC jet-like clusters. The mass is correlated with the transverse momentum of the jet-like cluster, and the mass cut changes the correlated yields. The mass cut lower limit is changed from $0.4GeV/c^2$ to $0.39GeV/c^2$, and the results are marked as item e in Table 5.4.

From a series of systematic checks, the correlation yield for EEMC jet-like cluster ($mass > 0.4GeV/c^2$) per FMS triggered π^0 with low p_t cuts is $I_{pp} = 0.00501 \pm 0.00008^{+0.00183}_{-0.00001}$ ($I_{dAu} = 0.01589 \pm 0.00032^{+0.00281}_{-0.00216}$) in p+p (d+Au) collisions and the average value is $I_{pp} = 0.00595 \pm 0.00011^{+0.00310}_{-0.00001}$ ($I_{dAu} = 0.01764 \pm 0.00042^{+0.00114}_{-0.00225}$) with high p_t cuts.

	p+p collision (low p_t)	d+Au collision (low p_t)
χ^2/NDF	60.9/11	31.1/11
Constant	0.000526 ± 0.000011	0.006624 ± 0.00006
Integral	0.00327 ± 0.00007	0.01184 ± 0.00036
Centroid	3.14 ± 0.013	3.16 ± 0.017
Width	0.8079 ± 0.0175	0.9387 ± 0.0239
	p+p collision (high p_t)	d+Au collision (high p_t)
χ^2/NDF	43.7/11	27.8/11
Constant	0.00049 ± 0.000015	0.00662 ± 0.000078
Integral	0.00383 ± 0.000097	0.01285 ± 0.00045
Centroid	3.135 ± 0.016	3.154 ± 0.020
Width	0.7126 ± 0.0193	0.8554 ± 0.0271

Table 5.5: The fitted parameters for the azimuthal correlations of FMS π^0 and EEMC jet-like cluster with $1.3 < \eta < 1.7$ in p+p and d+Au collisions in Figure 5.16. The results have been corrected by mixed events.

We also study the systematic uncertainties about the width differences from p+p collisions to d+Au collisions. For reference, the EEMC jet-like cluster is reconstructed with 600MeV tower threshold, $1.1 < \eta < 1.9$ and cone radius R = 0.6. The azimuthal correlations of FMS π^0 and EEMC jet-like cluster width differences from p+p interactions to d+Au interaction are 0.0957 ± 0.0200 for low p_t cuts and 0.1295 ± 0.0229 for high p_t cuts (see Figure 5.15).

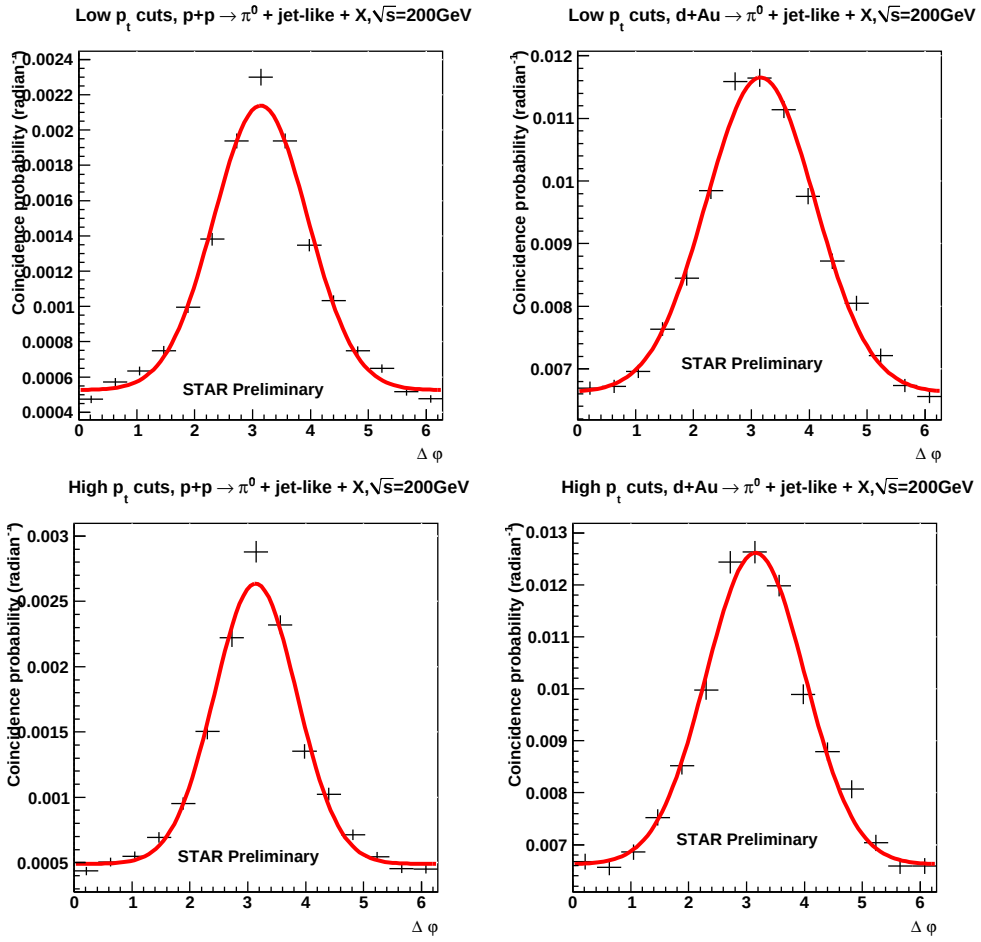

Figure 5.16: Coincidence probability with new η cut ($1.3 < \eta < 1.7$) for the EEMC jet-like cluster. Top: The azimuthal correlations of FMS π^0 with $p_t^{FMS} > 2.0 GeV/c$ and EEMC jet-like cluster ($M > 0.4 GeV/c^2$) with $1.0 GeV/c < p_t^{EEMC} < p_t^{FMS}$ in p+p (left) and d+Au (right) collisions. Bottom: The azimuthal correlations of FMS π^0 with $p_t^{FMS} > 2.5 GeV/c$ and EEMC jet-like cluster ($M > 0.4 GeV/c^2$) with $1.5 GeV/c < p_t^{EEMC} < p_t^{FMS}$ in p+p (left) and d+Au (right) collisions. Red line is the fit function $G(x)$ (see definition in Eq 5.4). The fitted parameters can be found in Table 5.5.

I. Cone radius A different cone radius R=0.5 is used. The width differences with low p_t cuts are $\Delta(\sigma_{dAu} - \sigma_{pp}) = 0.1163 \pm 0.0279$ and the results with high p_t cuts are $\Delta(\sigma_{dAu} - \sigma_{pp}) = 0.1107 \pm 0.0264$.

II. EEMC tower energy threshold The underlying event contribution decreases as tower energy threshold increases, but the width differences between p+p and d+Au collisions do not change too much (see Figure 5.12). We tune the EEMC tower energy threshold to 260MeV, The width differences with low p_t selections are $\Delta(\sigma_{dAu} - \sigma_{pp}) = 0.0822 \pm 0.0136$ and the results with high p_t

Item	Width differences $\Delta\sigma$ (low p_t)	Width differences $\Delta\sigma$ (high p_t)
standard	0.0957±0.0200	0.1295±0.0229
I	0.1163±0.0279	0.1107±0.0264
II(1)	0.0822±0.0136	0.1196±0.0173
II(2)	0.0770±0.0140	0.1242±0.0173
III	0.1308±0.0296	0.1428±0.0333
IV	0.1098±0.0147	0.1246±0.0220
systemactic	+ 0.0206 - 0.0187	+0. 0030 -0. 0188

Table 5.6: Summary of the systematic analysis for the width differences between p+p and d+Au interactions $\Delta\sigma$ with lower (column 2) and higher (column 3) p_T selections. "Standard" is the coincidence probability of FMS π^0 and EEMC jet-like cluster with the tower energy threshold 600MeV and $0.4GeV/c^2$ mass lower limit for the reconstructed jet-like cluster in the EEMC. The definition of other item are described in text.

cuts are $\Delta(\sigma_{dAu} - \sigma_{pp}) = 0.1196 \pm 0.0173$. With 240MeV threshold, the low p_t selections are $\Delta(\sigma_{dAu} - \sigma_{pp}) = 0.0770 \pm 0.0140$ and the width differences between p+p and d+Au collisions are $\Delta(\sigma_{dAu} - \sigma_{pp}) = 0.1242 \pm 0.0173$.

III. Pseudo-rapidity cuts for the EEMC jet-like cluster The η cuts change the correlated yield, the pseudo-rapidity cuts change from $1.1 < \eta < 1.9$ to $1.3 < \eta < 1.7$ to see the impacts on the width differences. Figure 5.16 shows the FMS π^0 -EEMC jet-like cluster correlation and the jet-like clusters are reconstructed within $1.3 < \eta < 1.7$. The width differences with low p_t selections are $\Delta(\sigma_{dAu} - \sigma_{pp}) = 0.1308 \pm 0.0296$ and the results with high p_t selections are $\Delta(\sigma_{dAu} - \sigma_{pp}) = 0.1428 \pm 0.0333$.

IV. Mass cut lower limit for the EEMC jet-like cluster The underlying event contribution decreases as the mass cut lower limit for the jet-like cluster increases, but the width differences between p+p and d+Au collisions do not change too much (see Figure 5.14). The mass cut lower limit is changed from $0.4GeV/c^2$ to $0.39GeV/c^2$ within the pseudo-rapidity $1.1 < \eta < 1.9$ cut. The width differences with low p_t selections are $\Delta(\sigma_{dAu} - \sigma_{pp}) = 0.1098 \pm 0.0147$ and the results with high p_t selections are $\Delta(\sigma_{dAu} - \sigma_{pp}) = 0.1246 \pm 0.0220$.

Based on the systematic studies shown above, the correlation width differences between p+p collisions and d+Au collisions for the coincidence probability of FMS π^0 and EEMC jet-like cluster are $0.0957 \pm 0.0200^{+0.0351}_{-0.0187}$ with high p_t cuts and $0.1295 \pm 0.0229^{+0.0133}_{-0.0188}$ with low p_t cuts.

5.4 Azimuthal correlation centrality dependence in d+Au

In high energy experiment, not all heavy ion collisions are head on interactions. One important parameter is the impact parameter b defined as the perpendicular distance between the path of a projectile and the center of the potential field created by an object that the projectile is approaching. At small impact parameter b, the projectile is close to the center of the approaching object, and such collision is defined as central collision. The interaction with large impact parameter b is defined as peripheral collision. Figure5.17 shows the schematics of peripheral and central d+Au collisions. Central d+Au collisions are expected to have more medium effects than the peripheral d+Au collisions for the di-hadron correlations. We have found suppression of back-to-back forward π^0 - forward π^0 azimuthal correlation in central d+Au collisions, which is consistent with the CGC prediction [11]. To see whether the forward+near-forward correlation have similar phenomena like the forward-forward correlations, we studied the centrality dependence for the FMS π^0 - EEMC jet-like cluster azimuthal correlations.

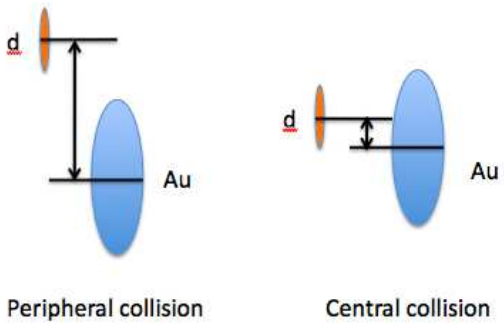

Figure 5.17: Schematics of peripheral d+Au collisions and central d+Au collisions.

The multiplicity of final state particles in central d+Au collisions is higher than that in peripheral d+Au collisions as at small impact parameter (central collision) more partons inside gold nuclei is probed by the deuteron. During RHIC run8 operation, east BBC records the multiplicity of charged particles from the gold beam. In d+Au collision, the multiplicity recorded in the east BBC facing gold beam is a indirect measurement of centrality of interaction.

5.4.1 Centrality selection with east BBC multiplicity cuts

To better understand the BBC response, a slow simulator is developed to get similar ADC output for the BBC during online data taken. To separate peripheral collisions from central collisions, a specific study had been done in HIJING+GSTAR+slow-simulator Minimum Bias d+Au simulation [11]. The response of individual BBC tile had been tuned to look like data in the slow simulator. From Figure 5.18, the impact parameter in HIJING event generator is strongly correlated with the multiplicity measured in the gold beam which is quantified by the ADC charge sum

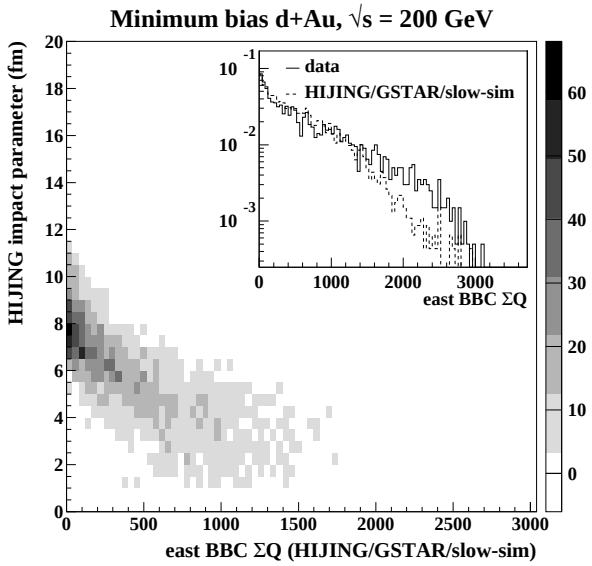

Figure 5.18: Impact parameter in HIJING versus charge sum in the east BBC (facing gold beam) in HIJING+GSTAR+slow-simulator simulation events. The comparison between data and simulation is shown in the inset. Solid line stands for data and dashed line is simulation. Figure from [11].

$\sum Q(BBC_{east})$	Average impact parameter (fm)
0-500	6.8 ± 1.7
2000-4000	2.7 ± 1.3

Table 5.7: Average impact parameter b in different $\sum Q(BBC_{east})$ region.

measured in the east BBC ($\sum Q(BBC_{east})$). The projected impact parameter b in different $\sum Q(BBC_{east})$ regions are shown in Table 5.7. The Au nuclei radius is about 7.63fm. From Table 5.7 the deuteron only approaches the edge of the Au neclei in events where $0 < \sum Q(BBC_{east}) < 500$. The impact parameter with $0 < \sum Q(BBC_{east}) < 500$ cuts is over two times larger than that with $2000 < \sum Q(BBC_{east}) < 4000$ cuts. The ADC charge sum $\sum Q(BBC_{east})$ looks similar in data and simulation (see Figure 5.18 inset plot). This study suggests the multiplicity detected in the east BBC is an indirect measurement of centrality in d+Au collision.

Figure 5.19 shows charge sum measured in east BBC ($\sum Q(BBC_{east})$) with events that have coincident FMS π^0 with $p_t^{FMS} > 2.0GeV/c$ and EEMC jet-like cluster (M $> 0.2GeV/c^2$) $1.0GeV/c < p_t < p_t^{FMS}$. Therefore additional studies about d+Au collision with only forward π^0 triggered in the FMS. The differences between distribution under coincidence condition and Minimum Bias events especially at low $\sum Q(BBC_{east})$ region are due to forward trigger bias in correlation analysis. Consequently, the peripheral d+Au interaction is selected with $0 < \sum Q(BBC_{east}) < 500$ and central d+Au interaction is selected with $2000 < \sum Q(BBC_{east}) < 4000$.

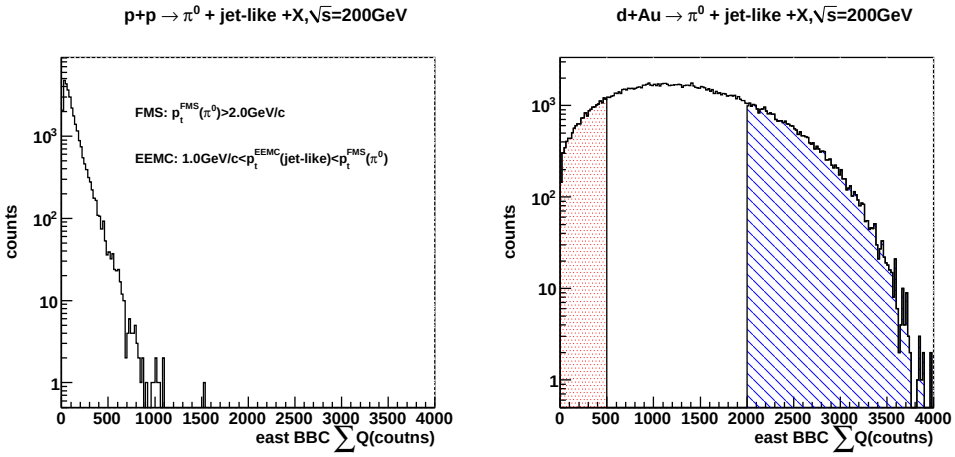

Figure 5.19: The ADC charge sum in the east BBC ($\sum Q(BBC)$) with coincidence requirements: FMS π^0 with $p_t^{FMS} > 2.0GeV/c$ and EEMC jet-like cluster ($M > 0.4GeV/c^2$) with $1.0GeV/c < p_t^{EEMC} < p_t^{FMS}$. Left panel shows $\sum Q(BBC)$ in p+p collision and the results in d+Au collision are shown in the right plot. Peripheral d+Au collision is defined within $0 < \sum Q(BBC_{east}) < 500$ region and central d+Au collision is defined within $2000 < \sum Q(BBC_{east}) < 4000$ region.

5.4.2 Correlations in peripheral and central d+Au interactions

The azimuthal correlations in d+Au collisions are divided with different centrality according to the criteria shown in Figure 5.19. The azimuthal correlations of FMS π^0 $p_t^{FMS} > 2.0GeV/c$ and EEMC jet-like clusters ($M > 0.4GeV/c^2$) with $1.0GeV/c < p_t^{EEMC} < p_t^{FMS}$ with different centralities in d+Au collisions are shown in Figure 5.20. The results are fitted with a constant plus a Gaussian function. The fitted constant, the integral and width of the Gaussian function are listed in Table 5.8.

The correlations in peripheral d+Au collisions look like p+p collision although the pedestal in peripheral d+Au collisions is higher than p+p collision. The correlations in central d+Au collisions have much larger width. The relative broadening from peripheral to central collisions in d+Au interactions is caused by the higher parton density in central d+Au collisions where the Au nuclei is a dense medium. The integral of the correlation signals (Only the fitted Gaussian function above the constant) in the central d+Au collisions looks similar as that in peripheral d+Au collisions while the pedestal underneath the correlations is much higher in central d+Au collisions. This means the higher multiplicity in central d+Au collisions mainly contribute to the pedestal which is not associated with the FMS triggered π^0. The width differences between central and peripheral d+Au collisions are not due to the different particle multiplicities, and they indicate the probabilities of the probe seeing multiple scattering inside the Au nuclei get increased in central d+Au collisions. There is no suppression on the back-to-back FMS π^0 - EEMC jet-like cluster azimuthal correlations in central d+Au collisions, which suggests the

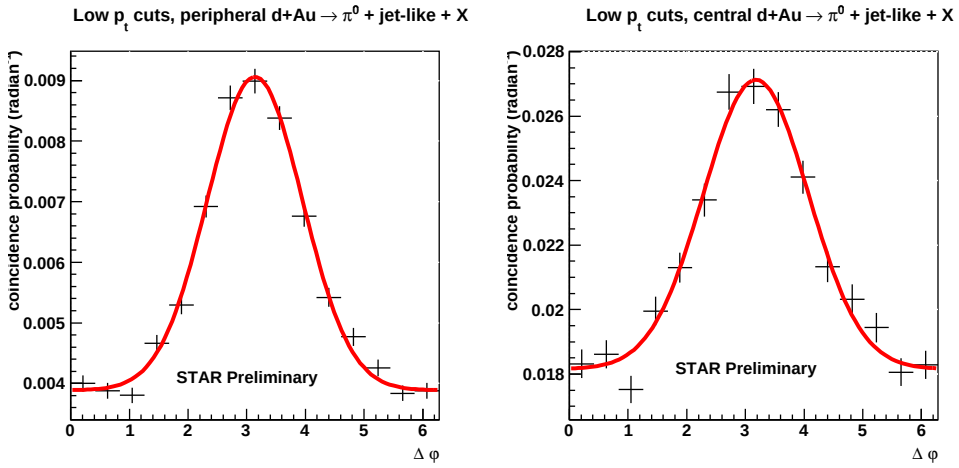

Figure 5.20: The azimuthal correlations of FMS π^0 with $p_t^{FMS} > 2.0GeV/c$ and EEMC jet-like cluster ($M > 0.4GeV/c^2$) with $1.0GeV/c < p_t^{EEMC} < p_t^{FMS}$ in peripheral (left) and central (right) d+Au collisions. To get enough statistics, the EEMC tower energy threshold is selected to be 600MeV. Red line is the fit function $G(x)$ (see definition in Eq 5.4). The fitted parameters can be found in Table 5.8.

sensitive x region that the FMS-EEMC correlations probe does not approach the saturation state.

5.5 Azimuthal correlation with west ZDC neutron tag in d+Au

5.5.1 West ZDC neutron tag - p+Au collision approach

Recent developments from theory expand from leading twist in perturbative QCD to double parton scattering in the scattering process. The double parton scattering is the case that one parton from proton of the deuteron scatters with one parton

	d+Au peripheral collision (low p_t)	d+Au central collision (low p_t)
χ^2/NDF	16.68/11	15.36/11
Constant	0.003888 ± 0.000062	0.01815 ± 0.00023
Integral	0.01053 ± 0.00036	0.0201 ± 0.0013
Centroid	3.14 ± 0.02	3.178 ± 0.036
Width	0.8118 ± 0.0253	0.8936 ± 0.0490

Table 5.8: The fitted parameters of azimuthal correlations of FMS π^0 $p_t^{FMS} > 2.0GeV/c$ and EEMC jet-like cluster ($M > 0.4GeV/c^2$) $1.0GeV/c < p_t < p_t^{FMS}$ in central and peripheral d+Au collisions in Figure 5.20. The results have been corrected by mixed events.

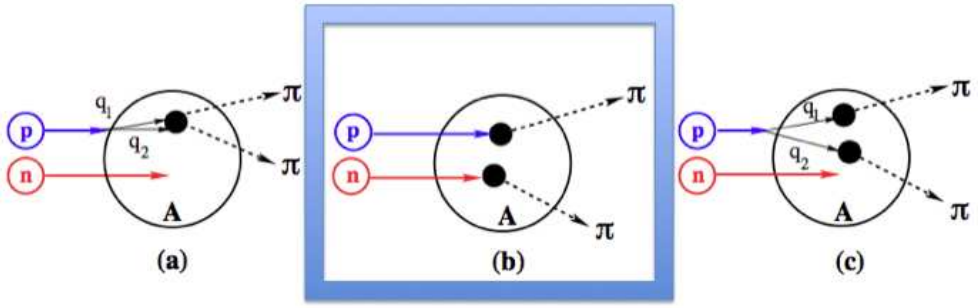

Figure 5.21: Schematics of double parton scattering in d+Au interaction. The middle panel shows independent double parton scattering. The final state pion pairs are generated by the process that one parton from proton inside the deuteron nuclei and another parton from neutron inside the deuteron nuclei independently scatters with the partons inside the gold nuclei. Figure from [94].

inside gold nuclei, one parton from neutron of the deuteron interacts with another parton inside the gold nuclei. See the middle panel of Figure 5.21. The double parton scattering only contributes to the pedestal of the azimuthal correlations in d+Au collisions [94]. As there is no p+Au collision arranged in previous RHIC runs, an qualitative approach with a neutron tag from the deuteron beam is studied.

The west ZDC facing deuteron beam at STAR is sensitive to the "spectator" forward neutrons. From simulation studies, background to the neutron signal from forward photons is small. The energy spectrum of forward particles detected in the west ZDC in d+Au HIJING+GSTAR simulation is dominated by the high energy neutron (E > 95GeV/c). The ADC sum in west ZDC (facing deuteron beam) during d+Au collisions is shown in the left panel of Figure 5.22. There is clear neutron signal in left panel of Figure 5.22, and neutron from deuteron is tagged with ADC sum in west ZDC ($\sum Q(ZDC_{west})$) between 10 and 90. The fraction of high energy neutron (E > 95GeV) in simulation is comparable to the number in the west ZDC neutron tag window ($10 < \sum Q(ZDC_{west}) < 90$). The multiplicity measured in the east BBC detector is proportional to the parton density in the gold nuclei. The impact on the centrality measurement in d+Au interactions with west ZDC neutron tag is shown in the right panel of Figure 5.22. Comparison between charge sum in east BBC detector with and without west ZDC neutron tag shows that the centrality measurements with ZDC neutron tag cut prefers to peripheral interaction. Further simulation studies with high energy neutron (E > 95GeV) detected in the west ZDC demonstrated the average impact parameter in such event is larger than that in the d+Au collisions. As the centrality is in general different with and without west ZDC neutron tag in dAu interactions using the same cut on the $\sum Q(BBC_{east})$, the FMS π^0 - EEMC jet-like cluster azimuthal correlations are studied only in centrality averaged dAu interaction with west ZDC neutron tag.

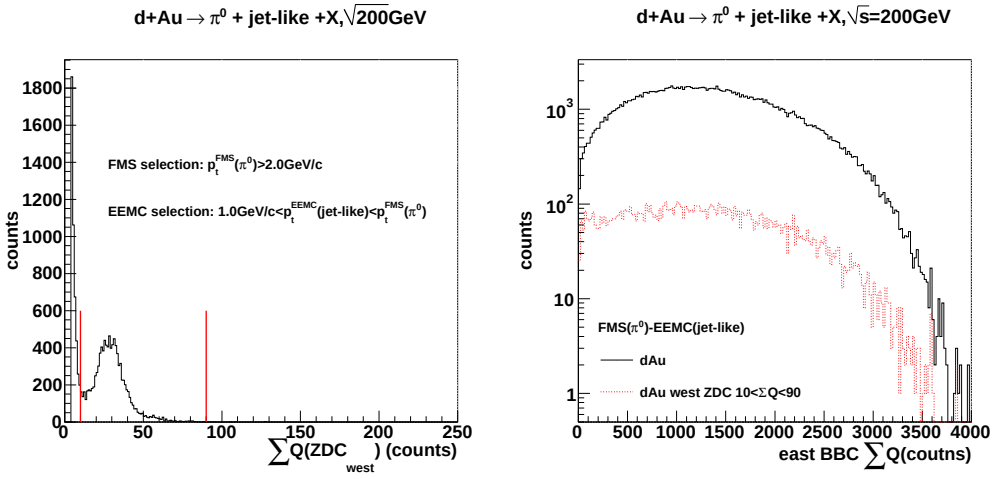

Figure 5.22: Left panel: The ADC charge sum in west ZDC ($\sum Q(ZDC_{west})$) in events containing FMS π^0 with $p_t^{FMS} > 2.0GeV/c$ and EEMC jet-like cluster (M $> 0.2GeV/c^2$) with $1.0GeV/c < p_t^{EEMC} < p_t^{FMS}$ in d+Au collisions. The two vertical lines stand for the neutron tag cuts $10 < \sum Q(ZDC_{west}) < 90$. Right panel: the ADC charge sum in east BBC ($\sum Q(BBC_{east})$ under the same conditions. The red dashed line shows the $\sum Q(BBC_{east})$ with the neutron tag cuts ($10 < \sum Q(ZDC_{west}) < 90$) and the black solid line stands for the results without the west ZDC ADC sum cuts.

5.5.2 Comparisons of the EEMC jet-like cluster with and without west ZDC neutron spectator in d+Au collisions

The relative characteristic scales of the jet-like cluster including energy, mass and jet-shape in d+Au collision with west ZDC neutron spectator are compared with such parameters in d+Au collisions.

5.5.3 Azimuthal correlations in p+Au collision approach

The FMS π^0 - EEMC jet-like cluster azimuthal correlations in d+Au collision with neutron spectator in the deuteron beam facing ZDC are studied to probe the independent double parton scattering in d+Au collisions. The FMS π^0 - EEMC jet-like cluster azimuthal correlation with $10 < \sum Q(ZDC_{west}) < 90$) in d+Au collisions with different p_t cuts are shown in Figure 5.23. The correlations results are fitted with a constant plus a Gaussian function with centroid at π. The constant, the width of the Gaussian function and the integral of the Gaussian function after fitting are put in Table 5.9.

The pedestal (constant parameter in Table 5.9) of the correlations in d+Au collisions related with uncorrelated final hadron states contains the information on the independent double parton scattering. The neutron spectator in the west ZDC is a good discriminator to approach p+Au collisions from simulation studies. From Table 5.9, the integral of the correlation peak in the approximate p+Au collisions

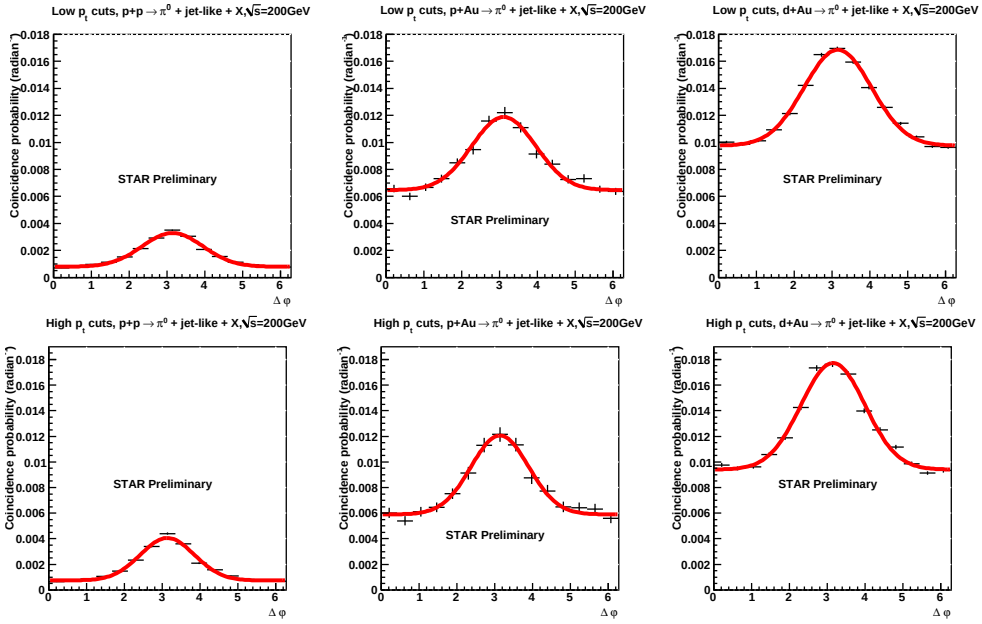

Figure 5.23: The azimuthal correlation in p+p collisions, d+Au collisions with west ZDC neutron tag and d+Au collisions. To get enough statistics, the tower threshold is selected as 600MeV. Top row event requirements are FMS π^0 $p_t^{FMS} > 2.0GeV/c$ and EEMC jet-like cluster ($M > 0.4GeV/c^2$) $1.0GeV/c < p_t^{EEMC} < p_t^{FMS}$, bottom row event requirements are FMS π^0 $p_t^{FMS} > 2.5GeV/c$ and EEMC jet-like cluster ($M > 0.4GeV/c^2$) $1.5GeV/c < p_t^{EEMC} < p_t^{FMS}$. Left panel shows results in p+p collisions, middle panel shows the correlations in d+Au collisions with west ZDC neutron tag $10 < \sum Q(ZDC_{west}) < 90$ and the right panel shows the correlations in centrality averaged d+Au collision. The red line are the fit function G(x) (see definition in Eq 5.4) and the fitted parameters are put in Table 5.23.

is comparable with the value in d+Au collisions. This indicates the correlations are from nucleon inside deuteron which scatters with multiple partons in Au nuclei. The pedestal in p+Au collisions is about two thirds of the value in d+Au collisions with low p_t cuts. The differences come from independent double parton scattering contribution in d+Au collisions. With high p_t cut, the azimuthal correlation pedestal in p+Au approach is about half in d+Au collisions. This study sheds a light on the independent parton scattering clarified in [94]. It would be interesting to perform correlation analysis in further p+Au collisions.

The integral and the width of the Gaussian signal in p+Au approach are consistent with d+Au collision results. This indicates the correlation signal above pedestal does not see much contributions from scattering of multiple partons from deuteron nuclei. With this said, the integral of the Gaussian peak above pedestal in the azimuthal correlation is a indirect measurement of the gluon density in Au nuclei in the sensitive x_{BJ} region [0.003, 0.02].

	p+p (low p_t)	p+Au (low p_t)	d+Au (low p_t)
χ^2/NDF	75.08/11	14.81/11	49.96/11
Constant	0.0008021 ± 0.0000125	0.006464 ± 0.000141	0.009757 ± 0.000056
Integral	0.005025 ± 0.000079	0.01145 ± 0.00081	0.01589 ± 0.00032
Centroid	3.141 ± 0.0010	3.112 ± 0.039	3.157 ± 0.011
Width	0.7978 ± 0.0124	0.8426 ± 0.0549	0.8935 ± 0.0157
	p+p (high p_t)	p+Au (high p_t)	d+Au (high p_t)
χ^2/NDF	70.32/11	6.597/11	49.42/11
Constant	0.0007415 ± 0.000017	0.005902 ± 0.000173	0.009404 ± 0.000073
Integral	0.005949 ± 0.000112	0.01174 ± 0.00097	0.01764 ± 0.00042
Centroid	3.136 ± 0.012	3.137 ± 0.047	3.156 ± 0.014
Width	0.7154 ± 0.0143	0.7604 ± 0.0597	0.8449 ± 0.0179

Table 5.9: Comparison of fitted parameters on the azimuthal correlations in p+p collisions, d+Au collisions with west ZDC neutron tag (p+Au collisions) and d+Au collisions. The correlations are after mixed events correction. The fitting parameters of correlations between FMS π^0 $p_t^{FMS} > 2.0 GeV/c$ and EEMC jet-like cluster ($M > 0.4 GeV/c^2$) $1.0 GeV/c < p_t^{EEMC} < p_t^{FMS}$ are shown in the upper half and fitting parameters of correlations between FMS π^0 $p_t^{FMS} > 2.5 GeV/c$ and EEMC jet-like cluster ($M > 0.4 GeV/c^2$) $1.5 GeV/c < p_t^{EEMC} < p_t^{FMS}$ are shown in the lower half.

Chapter 6

Conclusions and Outlook

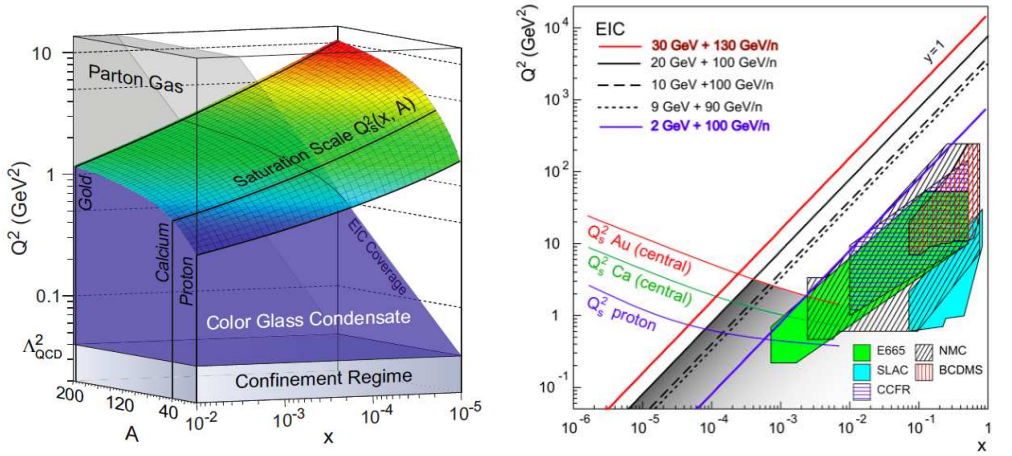

Figure 6.1: The phase diagram in x_{BJ}, Q^2 and A three dimensional frame from parton gas to the Color Glass Condensate is shown in the left panel, figure from [95]. The projection in x_{BJ} and Q^2 at rapidity $y = 1$ of EIC (Electron-Ion-Collider) covered region with different electron+nucleus energy setups is shown in the right panel, and the solid or dashed lines stand for different combinations of electron energy + heavy ion energy. The colored boxes represent the data of existing fixed target experiments.

The low x_{BJ} physics (related with high center of mass energy $\sqrt{s}$, forward pseudo-rapidity η and low Q^2 [$Q^2 > \Lambda_{QCD}$]) proves the dipole model can be applied in the proton(or deuteron)-nucleus interaction processes. In addition to the forward+forward correlations and the forward+mid-rapidity correlations, the transition process from dilute parton system which can be described by perturbative QCD to the dense CGC state is implemented by adding the FMS π^0 and EEMC jet-like cluster azimuthal correlations analysis at fixed Q^2. Although the jet-like clusters minimizes the effects from fragmentation function of hadron production in p+p and d+Au interactions, the behavior of the initial state gluons should be universal and independent of the fragmentation functions. In the systematic studies for the FMS-EEMC correlations, the underlying events contributions do not impact the width differences between p+p collisions and d+Au collisions. Significant broadening from p+p interactions to d+Au interactions is found in the FMS π^0 and EEMC jet-like cluster azimuthal correlations. This is consistent with the expecta-

tion that the forward+near-forward correlations probe lower x_{BJ} region than the forward+mid-rapidity correlations. The study of the FMS π^0 - EEMC jet-like cluster azimuthal correlations suggests the transition process to the low x_{BJ} saturation state is smooth at low Q^2.

Some theorists extend from leading twist to double parton scattering [94]. The independent double parton scattering which stands for one parton from proton of the deuteron and one parton from neutron of the deuteron interact with the partons inside gold nuclei individually is expected to only contributes to the pedestal of the azimuthal correlations. We use the west ZDC neutron tag in d+Au collisions to approach p+Au collisions to study the impacts from the individual double parton scattering. The FMS-EEMC correlations in p+Au approach shows comparable results on the ratio between the pedestal and the correlation peak which is consistent with the predictions of [94]. The azimuthal correlation analysis can be further studied in p+A collisions without considering the nuclear effect of deuteron.

The latest theory model including both q+g and g+g channels shows good agreements for the forward-forward correlations in peripheral and central d+Au collisions [96]. Current models can only well describe the azimuthal correlations of particles in the same pseudo-rapidity region. It is still a challenge for theorists to explain the correlations with a pseudo-rapidity gap as gluons can exchange between the outgoing two jets. The di-hadron correlations in the hadron (nucleus) - hadron (nucleus) interaction is a complex process as both the initial and final states carry color charges and there are strong interactions between them. Drell-Yan processes only contain lepton pairs in the final state, it is the cleanest channel in hadron (nucleus) - hadron (nucleus) interactions to probe the initial state, some theorist proposed to test the universality of unintegrated gluon distribution at low x with Drell-Yan process [97].

The saturation scale Q_s^2 at LHC is larger than at RHIC, it is about $2.6 - 4GeV^2$ at mid-rapidity and about $10GeV^2$ for rapidity $y = 3$ [44]. This means the inclusive production and correlation results at RHIC are achievable at central rapidity and the results get enhanced at forward rapidity. Another clear path is to use DIS process with a leptonic probe instead of a color baggage. A future Electron-Ion collider can do a series of precision studies to probe a wide Q_s^2 ($Q^2 \sim Q_s^2 >> \Lambda_{QCD}$) range. As shown in the right panel of Figure 6, the new EIC can measure lower x_{BJ} related with gluon saturation in nucleus than the fixed target nucleus experiments. As indicated in Figure 6, the low x measurements can be realized in the near forward region (eg. rapidity y = 1) in the EIC collider.

Appendix A

Hardware related studies

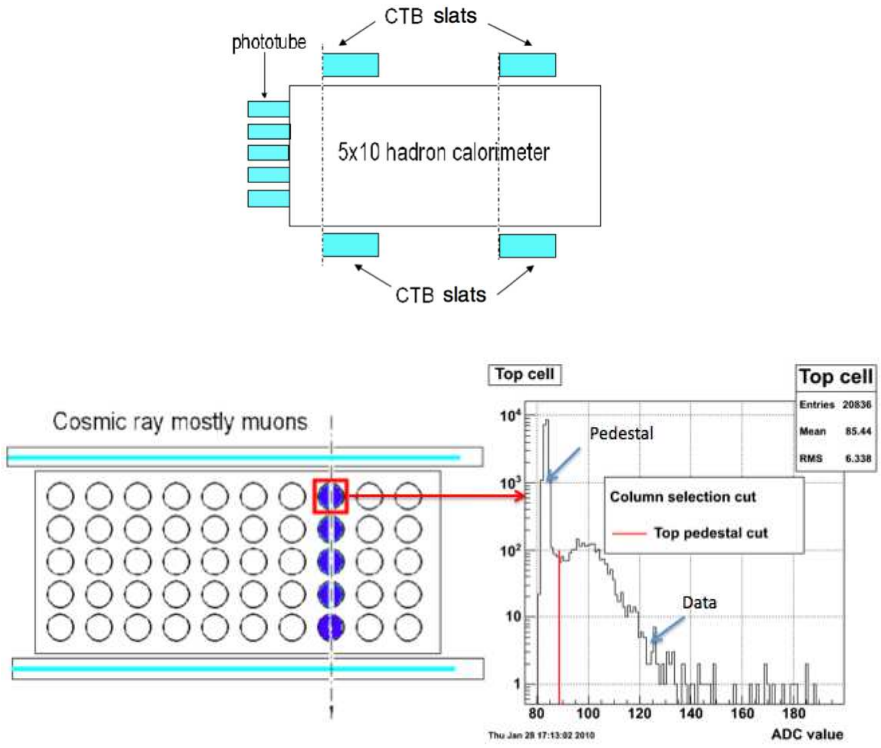

Figure A.1: The cosmic ray test setup of the 5×10 hadronic calorimeter module. Two groups of We took cosmic ray data for a 5×10 module of the lead-scintillating hadronic calorimeter. Central Trigger Barrel (CTB) scintillating slats are used as coincidence triggers. Top panel shows the side view of the setup. The front view of the setup is shown in Bottom left panel. When one bunch of cosmic ray muons pass through the 5×10 module, the signals are recorded in the DAQ system. The the ADC values accumulated many events of one cell is shown in the right panel.

From September, 2009 to May, 2010, I joined in the proposed Forward Hadronic Calorimeter (FHC) cosmic ray test at STAR. The FHC detector will implement the hadronic capability in the forward rapidity ($\eta \sim 3.2$) of STAR. The FHC was proposed to be installed behind the FMS at STAR to provide full jet measurements for spin physics. One goal is to distinguish Sivers effects which is an initial quark state mechanism [98, 99] and Collins effects which is final state mechanism entangled

with quark transversity [100]. The Lambda transverse spin transfer measurement is also included in the FHC proposal.

Figure A.1 shows the cosmic ray test setup for a module of 5 × 10 hadronic calorimeter. Two groups of Central Trigger Barrel (CTB) scintillating slats mounted separately above or below the hadronic module comprosies the coincidence triggers. The deposited energy from cosmic ray muons within the coincidence trigger time window is digitized into ADC values and recorded by the DAQ system. The ADC value of one cell accumulated many events is shown in the bottom right panel of Figure A.1. There are clear Landau like distribution above pedestal. Three different positions (one near the PMT side, one near the rear of the calorimeter, and another is in the middle) along the spaghetti calorimeters are chosen to locate the CTB slats. The ADC after pedestal subtraction is fitted with Landau function and the most probable value (MPV) of the Landau function with different positions are fit with a decay exponential function $y = y_0 exp(-x/L0)$. The decay length L_0 after fitting is consistent with value mentioned in the NIM paper of the hadronic calorimeter [101]. This work had been presented in the 2010 APS April meeting.

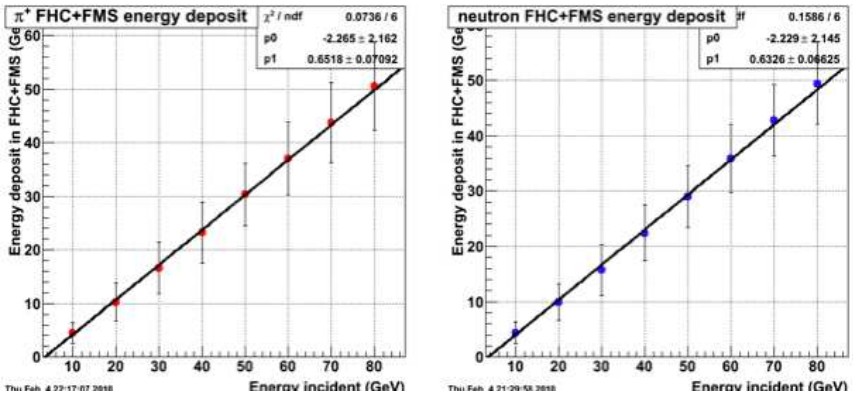

Figure A.2: The deposited energy in FMS+FHC versus incident energy of single particle in GEANT. The results for π^+ are shown in the left panel and neutron studies are presented in the right panel. The energy range is from 10GeV to 80GeV with step 10GeV.

The hadron response with GEANT simulation is studied. Particle passing through the STAR detectors have energy deposited in the detectors. The energy resolutions are studied with single particle penetrating both the FMS and the FHC. Figure A.2 shows good linearity in the deposited energy of the FMS+FHC versus the incident energy and the energy resolution is independent on particle species. Lambda (Λ) decays into neutron and π^0 with branch ratio about 35.8%. As the π^0 decayed photons can be well defined in the FMS, the hadron energy resolution in the FMS+FHC has good linearity, the reconstruction of Λ can be realized through n$\gamma\gamma$ channel. In experiment, the charged ρ yields are larger than the Λ yields. In addition, the branching ratio of $\rho^+ \to \pi^+ + \pi^0$ is near 100%. Therefore, the ρ^+ reconstruction in PYTHIA+GEANT with the FMS(existing)+FHC(proposed) is also

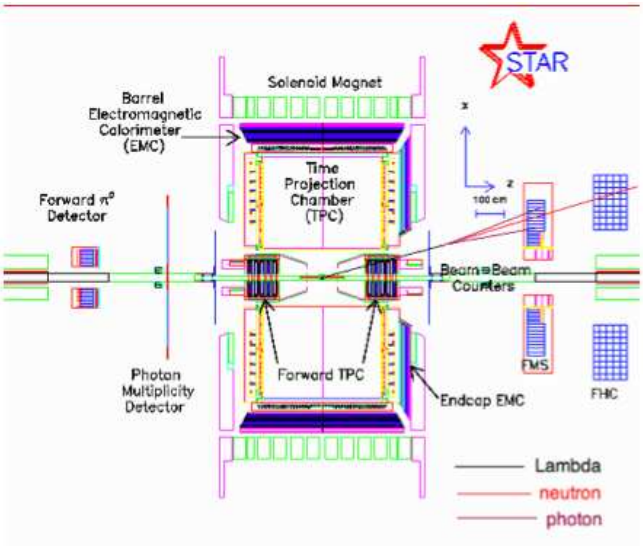

Figure A.3: Skematics of Lambda (Λ) cay in the forward region at STAR. $\Lambda \rightarrow n + \pi^0$, π^0 decayed photon daughters can be well defined in the FMS, the neutron decayed from the Λ deposit energy in the FMS and the FHC. The Λ can e reconstructed through n$\gamma\gamma$ channel.

studied to provide calibration for further Λ reconstructions. The reconstructed ρ^+s have a large fraction associated with PYTHIA level ρ^+s, the method can be developed further during collision data taking and symmetric configuration more close to beam pipe.

From August 2010 to May, 2011, I joined in the AnDY feasibility experiment which is aiming to measure Drell-Yan processes within transverse polarized p+p collisions at $\sqrt{s} = 500GeV$. AnDY was taken as an interaction point at RHIC 2 o'clock position during RHIC run11 operation. FigureA.5 shows the schematics of AnDY configuration in RHIC run11. The main setup of AnDY run11 consist of two 9×12 lead scintillating hadronic calorimeter, two 7×7 lead glass electromagnetic calorimeter (EM cal), two layers of preshower detectors and two modules of Beam Beam Counter(BBC). Based on the 5×10 module cosmic ray test strategies, we calibrated the two 9×12 hadronic modules. We designed 4 separate LED fiber boxes providing LED triggers to monitor the hadronic response during online data taken. I joined in the cell by cell PMT calibrations of the EM cal and assembling of the two layers of preshower detectors. We finished the hadronic calorimeter energy calibrations based on data and simulation comparisons for π^0; the calibration on hadronic shower is ongoing. A first look at the di-lepton pairs is tried with pairs contain a cluster in the EM cal and a cluster in the hadronic calorimeter. To reduce combinatory background, the related BBC tile should have a MIP like singal. Figure A.4 shows the invariant mass spectrum of the cluster pairs under these conditions, a clear J/Ψ peak appears above the background including photon pair, charged hadron pair, hadron-photon pair and so on. The J/Ψ analysis opens a window for

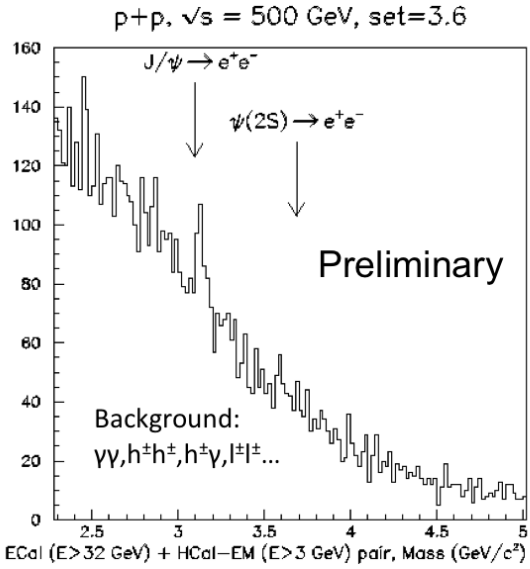

Figure A.4: The invariant mass of pair contains one cluster with $E > 32GeV$ in the EM calorimeter and one cluster with $E > 3GeV$ in the hadronic calorimeter, a MIP like response is required in the relevant BBC tile. A clear J/Ψ peak and a possible $\Psi(2S)$ signal exist above background. The background consists of photon pair, charged hadron pair, charged hadron + photon pair and lepton pairs.

future Drell-Yan process studies related with Sivers function.

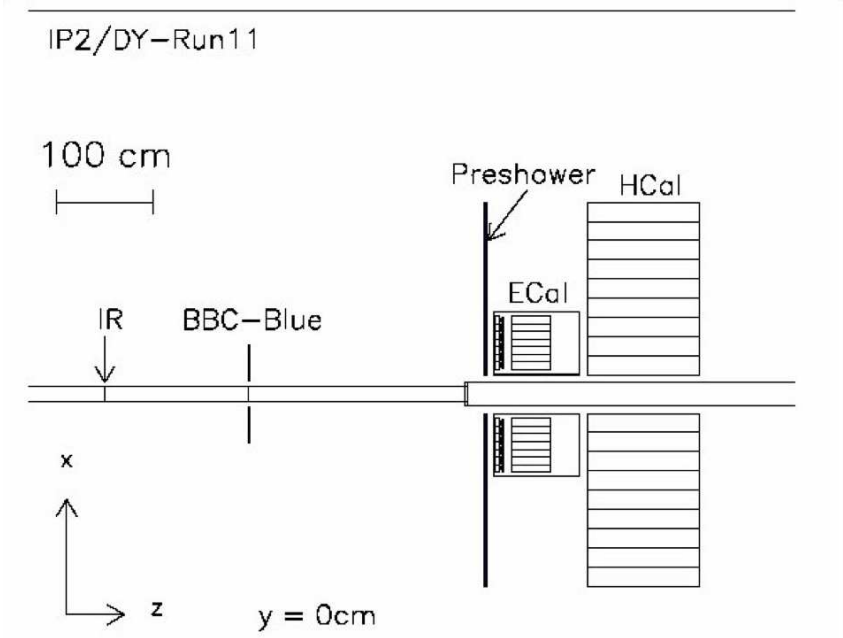

Figure A.5: The schematics of RHIC run11AnDY setup.

Appendix B

Acknowledge

I would like to take this opportunity here to thank my supervisor Prof. Zuotang Liang for his guidance and support during my PhD training processes. I would like also to thank Prof. Qinghua Xu for his help and suggestions for my studies at the STAR experiment of RHIC. I would like to thank Nu Xu who is the STAR experiment spokesperson for his support and invitation to stay at Brookhaven National Lab.

The study life at Brookhaven National Lab is an unforgettable memory to me. I would like to thank Leslie C. Bland and Hank Crawford for a series of discussions, suggestions and help on the data analysis and hardware work related with this thesis. I would like to thank Akio Ogawa for his help on my understanding the software configuration and his efforts getting the simulation sample. I would like to thank Ermes Braidot, Chris Perkins, Jack Engelage, Larisa Nogach, Nikolai Minaev and George Igo for the very nice discussions and suggestions about the research topic I am involved in. I would like to thank Alexander Bazilevsky and Elke-caroline Aschenauer for the discussions related with the RHIC CNI polarimeter analysis. Thanks very much to the people mentioned before, three years of studying and working in Brookhaven National Lab help me build up the view what the high energy experiment is.

I would like to thank the friends and classmates at Shandong University, Graduate University of the Chinese Academy of Sciences and Brookhaven National Lab who I have spent a very good time with. Last but not least, I would like to thank my parents for reminding me keep on doing the things that I am interested in. Thanks for your love and understanding.

Reference

[1] X. Li, for the STAR Collaboration, J.Phys.Conf.Ser. **316**, 012002 (2011), hep-ex/1106.0621 1, 5, 64

[2] V. N. Gribov, L. N. Lipatov, Sov. J. Nucl. Phys. **15**, 438 (1972) 4, 14

[3] L. N. Lipatov, Sov. J. Nucl. Phys. **20**, 95 (1975) 4, 14

[4] G. Altarelli, G. Parisi, Nucl. Phys. B **126**, 298 (1977) 4, 14

[5] Y. L. Dokshitzer, Sov. Phys. JETP **46**, 641 (1977) 4, 14

[6] Y. Balitsky, L. Lipatov, Sov. Phys. JETP **28**, 822 (1978) 4, 15

[7] E. Kuraev, L. Lipatov, V. Fadin, Sov. Phys. JETP **45**, 199 (1977) 4, 15

[8] L. Lipatov, Sov. Phys. JETP **63**, 904 (1986) 4, 15

[9] E. Rizvi, *Talk presented at the International Euro Physics Conference on High Energy Physics* (2003) 4, 11, 13

[10] E. Braidot, Nucl. Phys. A **854**, 168 (2011) 4, 27

[11] E. Braidot, *Suppression of Forward Pion Correlations in d+Au Interactions at STAR* (2010), hep-ph/1005.2378 5, 27, 29, 108, 109

[12] E. Braidot, Ph.D. thesis, The University of Netherlands (2011), nucl-ex/1102.0931 5, 27, 47, 54, 55, 59, 61

[13] C.Adloff, et al., Eur. Phys. J. C **21**, 33 (2001) 7, 25

[14] S. Chekanov, et al., Eur. Phys. J. C **21**, 443 (2001) 7, 25

[15] M. Peskin, D.Schroeder, *An introduction to Quantum Field Theory* (Addison-Wesley, 1995) 7, 8

[16] R. D. Field, D. Pines, *Applications Of Perturbative Qcd* (Addison-Wesley, 1995) 7, 8

[17] J. Pumplin, A. Belyaev, J. Huston, et al., JHEP **0602**, 032 (2006) 7, 14

[18] G. Dissertori, I. Knowles, M. Schmelling, *Quantum Chromodynamics, High Energy Experiments and Theory* (Oxford Science Publications, 2003) 8

[19] J. D. Bjorken, Phys. Rev. **179**, 1547 (1969) 8

[20] J. C. Collins, D. E. Soper, G. Sterman, Adv.Ser.Direct.High Energy Phys **5**, 1 (1988), hep-ph/0409313 9

[21] M. Froissart, Phys. Rep. **123**, 1053 (1983) 9, 15

[22] K. Nakamura, et al., Journal of Physics G **37**, 075021 (2010) 10, 50

[23] M. Gluck, E. Hoffmann, E. Reya, Z. Phys. C **13**, 119 (1982) 12

[24] L. C. Bland, et al., Eur. Phys. J. C **43**, 427 (2005), `hep-ex/0502040` 13, 14, 28, 40

[25] F. Gelis, E. Iancu, J. J. Marian, et al. (2010), `hep-ph/1002.0333` 14

[26] L. Gribov, E. Levin, M. Ryskin, Phys. Rep. **100**, 1 (1983) 15

[27] A. H. Mueller, J. Qiu, Nuclear Physics B **268**, 427 (1986) 15

[28] Y. V. Kovchegov, Phys. Rev. D **60**, 034008 (2011), `hep-ph/990128` 15

[29] L. Gribov, E. Levin, M. Ryskin, Nucl. Phys. B **188**, 555 (1981) 15

[30] K. Golec-Biernat, M. Wusthoff, Phys. Rev. D **59**, 014017 (1999) 16, 17

[31] N. Nikolaev, B. Zakharov, Z. Phys. C **49**, 607 (1991) 16

[32] N. Nikolaev, B. Zakharov, Z. Phys. C **53**, 331 (1992) 16

[33] A. H. Mueller, Nucl. Phys. B **415**, 373 (1994) 16

[34] A. H. Mueller, Nucl. Phys. B **437**, 107 (1995) 16

[35] A. Mueller, Nucl. Phys. B **335**, 115 (1990) 17, 18

[36] L. McLerran, R. Venugopalan, Phys. Rev. D **49**, 2233 (1994) 17

[37] L. McLerran, R. Venugopalan, Phys. Rev. D **49**, 3352 (1994) 17

[38] J. Pumplin, D. Stump, J. Huston, et al., JHEP **0207**, 012 (2002) 17

[39] A. Martin, R. Roberts, W. Stirling, et al., Eur. Phys. J C **28**, 455 (2003) 17

[40] A. Bohr, B. R. Mottelson, *Nuclear Structure* (Benjamin, New York, 1969) 18

[41] H. Kowalski, D. Teaney, Phys. Rev. D **68**, 114005 (2003), `hep-ph/0304189` 18

[42] M. Gyulassy, I. Vitev, X.-N. Wang, et al., Quark Gluon Plasma 3 123–191 (2003), `nucl-th/0302077` 18

[43] L. McLerran, Lect.Notes Phys. **583**, 291 (2002), `hep-ph/0104285` 19, 20

[44] F. Gelis, E. Iancu, J. Jalilian-Marian, et al., Ann.Rev.Nucl.Part.Sci. **60**, 463 (2010), `hep-ph/1002.0333` 19, 118

[45] L. McLerran, R. Venugopalan, Phys. Rev. D **49**, 2233 (1994) 19, 20

[46] L. McLerran, R. Venugopalan, Phys. Rev. D **49**, 3352 19

[47] L. McLerran, R. Venugopalan, Phys. Rev. D **50**, 2225 (1994) 19

[48] Y. V. Kovchegov, A. H. Mueller, Nucl. Phys. B **529**, 451 (1998) 21

[49] A. Dumitru, L. D. McLerran, Nucl. Phys. A **700**, 492 (2002) 21

[50] J. Jalilian-Marian, A. Kovner, A. Leonidov, et al., Nucl. Phys. B **504**, 415 (1997) 21

[51] J. Jalilian-Marian, A. Kovner, H. Weigert, Phys. Rev. D **59**, 014015 (1999) 21

[52] A. Kovner, G. Milhano, H. Weigert, Phys. Rev. D **62**, 114005 (2000) 21

[53] E. Ferreiro, E. Iancu, A. Leonidov, et al., Nucl. Phys. A **703**, 489 (2002) 21

[54] E. Iancu, R. Venugopalan, *The Color Glass Condensate and High Energy Scattering in QCD* (2003), `hep-ph/0303204v3` 21

[55] I. Balitsky, Nucl. Phys. B **463**, 99 (1996) 21

[56] H. Weigert, Prog.Part.Nucl.Phys. **55**, 461 (2005) 22

[57] K. Itakura, *Color Glass Condensate and UHECR physics* 23

[58] K. Golec-Biernat, J. Phys. G **28**, 1057 (2002), `hep-ph/0109010` 24

[59] A. M. Stasto, K. G. Biernat, J. Kwiecinski, Phys. Rev. Lett. **86**, 596 (2001) 24

[60] A. Freund, K. Rummukainen, H. Weigert, et al., Phys. Rev. Lett. **90**, 222002 (2003) 24, 25

[61] M. Hirai, S. Kumano, T. H. Nagai, Phys. Rev. C **70**, 044905 (2004) 25

[62] E. Iancu, K. Itakura, L. McLerran, Nucl.Phys. A **708**, 327 (2002), `hep-ph/0203137` 25

[63] I. Arsene, et al., Phys. Rev. Lett. **93**, 242303 (2004) 25, 26

[64] J.Adams, et al., Phys. Rev. Lett. **97**, 152302 (2006) 26, 27

[65] A. Dumitru, A. Hayashigaki, J. Jalilian-Marian, Nucl. Phys. A **765**, 464 (2006) 26

[66] V. Guzey, M. Strikman, W. Vogelsang, Phys. Lett. B **603**, 173 (2004) 26, 27

[67] J. Qiu, I. Vitev, Phys. Rev. Lett **93**, 262301 (2004) 26

[68] J. Qiu, I. Vitev, Physics Letters B **632**, 507 (2006) 26

[69] D. Kharzeev, E. Levin, L. McLerran, Nucl. Phys. A **748**, 627 (2005) 26

[70] C. Marquet, Nucl. Phys. A **796**, 41 (2007) 29

[71] C. M. Javier L. Albacete, Phys. Rev. Lett. **105**, 162301 (2010), hep-ph/1005.4065v2 27

[72] A. Stasto, B.-W. Xiao, F. Yuan (2011), hep-ph/1109.1817v2 27

[73] K. Tuchin, Nucl. Phys. A **846**, 83 (2010) 27

[74] K. H. Ackermann, et al., Nucl. Instr. Meth. Res. A **499**, 2 (2003) 32

[75] K. Adcox, et al., Nucl. Instr. Meth. Res. A **499**, 2 (2003) 32

[76] T. Sakuma, M. Walker (2010), hep-ex/1012.1173 33

[77] M. Anderson, et al., Nucl. Instrum. Meth. A **499**, 659 (2003) 35

[78] M. Beddo, et al., Nucl. Instrum. Meth. A **499**, 725 (2003) 36

[79] C. E. Allgower, et al., Nucl. Instrum. Meth. A **499**, 740 (2003) 38

[80] J. K. for the STAR Collaboration (2005), hep-ex/0501072 42

[81] C. Adler, et al., Nucl. Instrum. Meth. A **470**, 488 (2001), nucl-ex/0008005v1 43

[82] J. Morris, S. Binello, T. Clifford, et al., *10th ICALEPCS Int. Conf. on Accelerator and Large Expt. Physics Control Systems proceedings* (2005) 45

[83] J. M. Landgraf, M. J. LeVine, A. Ljubicic, et al., Nucl. Instr. Meth. Phys. Res. A **499**, 762 (2003) 45

[84] F. S. Bieser, H. J. Crawford, J. Engelage, et al., Nucl. Instr. Meth. Phys. Res. A **499**, 766 (2003) 45

[85] S. van der Meer, CERN-ISR-PO **68**, 31 (1968) 47

[86] A. Drees, Z. Xu p.3120 (2001) 48

[87] T. Sjostrand, L. Lonnblad, S. Mrenna (2001), hep-ph/0108264 49, 55

[88] X. Wang, M. Gyulassy, Phys. Rev. D **44**, 3501 (1991) 49, 55

[89] S. Agostinelli, J. Allison, K. Amako, et al., Nucl. Instr. Meth. Phys. Res. A **506**, 250 (2003) 50

[90] A. Lednev, Nucl. Instr. Meth. Phys. Res. A **366**, 292 (1995) 51

[91] Y. Wang, *Measurement of Inclusive Forward Neutral Pion Production in 200 GeV Polarized Proton-Proton Collisions at RHIC*, Ph.D. thesis, The University of Texas at Austin (2004) 51, 52, 54

[92] C. P. L. L. Writeup, *Detector Description and Simulation Tool* (1993) 55

[93] R. Field, AIP Conf. Proc. **828**, 163 (2006) 89, 103

[94] M. Strikman, W. Vogelsang, Phys. Rev. D **83**, 034029 (2011), `hep-ph/1009.6123` 112, 114, 118

[95] D. Boer, et al., INT-PUB **11**, 034 (2011), `nucl-th/1108.1713v2` 117

[96] A. Stasto, B. wen Xiao, F. Yuan (2011), `hep-ph/1109.1817` 118

[97] F. Dominguez, C. Marquet, B.-W. Xiao, et al., Phys.Rev.D **83**, 105005 (2011), `1101.0715` 118

[98] D. W. Sivers, Phys. Rev. D **41**, 83 (1990) 119

[99] D. W. Sivers, Phys. Rev. D **43**, 261 (1991) 119

[100] J. C. Collins, Nucl. Phys. B **396**, 161 (1993), `hep-ph/9208213` 120

[101] T. A. Armstrong, et al., Nucl. Instr.and Meth. A **406**, 227 (1998) 120